

APPROVAL SHEET

Title of Thesis: Nonlinear Optics at Ultralow Power using Metastable Xenon in a High Finesse Cavity

Name of Candidate: Garrett Hickman
Doctor of Philosophy, 2017

Thesis and Abstract Approved: James D. Franson
Dr. James Franson
Professor
Department of Physics

Date Approved: 4 / 7 / 17

Abstract

Single-photon cross phase shifts and other single-photon nonlinearities have numerous applications in all-optical quantum information processing. Generating these nonlinearities though can be difficult. This has been done previously using sophisticated experiment setups, for instance using cold atoms optically trapped within the field mode of a high-finesse cavity. Several groups have experimentally achieved single-photon phase shifts on the order of π using these systems. However, nonlinearities weaker than this have important applications as well. In this work we introduce and demonstrate the idea of using metastable xenon gas in a high-finesse cavity to produce weak single-photon nonlinearities. Our system is relatively simple and robust, avoids problems associated with the accumulation of alkali atoms on mirror surfaces, and is capable of approaching the strong coupling regime of cavity quantum electrodynamics. It can compete with the performance of state-of-the-art cavity systems up to a single-atom cooperativity of roughly $\eta \approx 1$. Beyond this, the effects of atomic motion begin to play a larger role and improving the system performance becomes more difficult.

After a brief introduction to the use of optical cavities and the spectroscopic properties of metastable xenon, we demonstrate the feasibility of our approach by reviewing two proof-of-principle demonstrations performed in our lab. In these experiments, we measured absorption saturation and cross-phase modulation using a cavity of moderately high finesse $F = 3,000$. We found that nonlinear effects occurred at ultralow input power levels, proving that the presence of the cavity strongly enhanced the inherent optical nonlinearity of metastable xenon. We close by reviewing our recent progress in building an improved cavity system, which is expected to produce enhanced single photon cross phase shifts.

Nonlinear Optics at Ultralow Power using Metastable Xenon in a High Finesse Cavity

Garrett Hickman
Department of Physics
UMBC
Baltimore, MD 21250

Dissertation submitted to the Faculty of the Graduate School of the
University of Maryland, Baltimore County in partial fulfillment
of the requirements for the degree of
Doctor of Philosophy
2017

© 2017, Garrett Hickman

All rights reserved

Contents

List of Tables	vii
List of Figures	viii
1 Introduction	1
2 Optical Cavities and Cavity Quantum Electrodynamics	6
2.1 Introduction to Optical Cavities	6
2.2 Transverse Mode Structure of a Fabry-Perot Cavity	11
2.3 Cavity QED and Quantum Nonlinear Optics	13
2.4 Theoretical Description of Dissipation and Dephasing	20
3 Xe Spectroscopy and Level Structure	27
3.1 Overview and Rationale for using Xe	27
3.2 Xe's Electron Configuration	28
3.3 Spectroscopy of Multi-Electron Atoms	30
3.3.1 The Hamiltonian	30
3.3.2 Eigenstates	32

3.3.3	LS-Coupling	33
3.3.4	jj-Coupling	36
3.3.5	jl-Coupling	37
3.4	Energy Level Structure of Xenon	40
3.5	Spectral Line Shapes and Broadening Mechanisms	43
3.5.1	Fundamental Theory	43
3.5.2	Homogeneous Broadening	46
3.5.3	Inhomogeneous Broadening	47
3.5.4	The Voigt Lineshape	49
3.5.5	Hyperfine Splitting and Comparison with Measurements	50
4	Experimental Methods	55
4.1	Overview	55
4.2	Vacuum System	55
4.3	Production of Metastable Xenon	56
4.3.1	DC Discharge Production	57
4.3.2	RF Discharge Production	59
4.3.3	All-Optical Production	62
4.3.4	Optically-Enhanced Production	65
4.4	Fiber-Coupled Optical Components	69
4.5	The Proof-of-Principle Optical Cavity	73
4.5.1	Cavity Design	73
4.5.2	Early Work with the Cavity	76

5	Ultra-Low Power Absorption Saturation	81
5.1	Overview	81
5.2	Absorption in a Cavity	81
5.3	Experiment Setup	84
5.4	Lock-and-Measure Method	87
5.5	Frequency Sweep Method	89
5.6	Initial Measurements	90
5.7	Results and Discussion	92
5.8	Conclusions	94
6	Ultra-Low Power Cross-Phase Modulation	95
6.1	Overview	95
6.2	Cross-Phase Modulation with Xenon	96
6.3	Design of the Experiment	98
6.4	Optical Amplifiers to Improve SNR	100
6.5	Noise from Back-Reflections	104
6.6	Laboratory Setup	107
6.7	Frequency Tuning	109
6.8	Searching for the Signal	112
6.9	Cross-Phase Shift Measurement	115
6.10	Theoretical Description	117
6.11	Results and Conclusions	125

7	New Cavity System	127
7.1	Overview	127
7.2	Design Considerations	127
7.3	The New Cavity	129
7.4	Redesign of the New Cavity	132
8	Conclusion and Summary	136
9	Bibliography	139

List of Tables

3.1	Spectroscopic notation for the orbital angular momentum quantum number	35
3.2	Summary of the spectroscopic notation used with the jl -coupling scheme . .	39
3.3	Transition rates, wavelengths, and frequencies for xenon transitions	43
3.4	Stable isotopes of xenon and percent natural abundances	51

List of Figures

2.1	Diagram of a general spherical-mirror optical cavity	7
2.2	Illustration of resonant light transmission in an optical cavity.	8
2.3	Illustration of Gaussian beam profile and phase wavefronts	13
2.4	Concept diagram of the Jaynes-Cummings model	15
2.5	Probabilities of finding the coupled atom-cavity system in either of states $ 1_a, n_c\rangle$ or $ 2_a, (n - 1)_c\rangle$	18
2.6	Energy level diagrams for the Jaynes-Cummings model	19
2.7	Conceptual diagram for an atom-cavity open quantum system	21
3.1	Illustration of excitations in Rb and Xe atoms	29
3.2	Excited state energy levels of xenon	41
3.3	Calculated absorption spectrum for a gas of identical metastable xenon atoms	46
3.4	Calculated absorption spectrum for a gas of room-temperature metastable xenon atoms, neglecting hyperfine splitting	50
3.5	Diagram of allowed transitions between hyperfine sublevels of the states $6s[3/2]_2^o$ and $6p[3/2]_2$	52
3.6	Measured transmission spectrum of metastable xenon at 823 nm	52

3.7	Measured transmission spectrum superposed with calculated Voigt profiles .	54
4.1	Diagram of the vacuum system	56
4.2	Photo of our vacuum system in the laboratory	57
4.3	DC discharge inside a xenon-filled vacuum chamber	58
4.4	Two RF circuit designs used in our work with RF discharge excitation . . .	60
4.5	Laboratory photo of a circuit of type (a)	61
4.6	Laboratory photo of a circuit of type (b)	62
4.7	Energy level diagram for all-optical production of Xe*	63
4.8	Photos of the VUV xenon discharge lamp in our vacuum chamber	65
4.9	Energy level diagram for the experimental demonstration of optically-enhanced Xe* production	66
4.10	Diagram of the experimental system for performing optically-enhanced production of Xe*	67
4.11	Measured absorption spectrum showing enhancement of metastable xenon density with optical pumping	68
4.12	Photograph of the experimental system as of July 10, 2015	69
4.13	Oscilloscope traces showing Fabry-Perot oscillations in laser transmission .	72
4.14	Diagram of the nickel block used to house the cavity mirrors.	74
4.15	Photograph illustrating the mounting system for the cavity	75
4.16	Photograph of the copper disk used to control the temperature of the vacuum feedthrough rod	76
4.17	Photo of the completed cavity within an RF discharge in the vacuum chamber	76

4.18	Oscilloscope traces of cavity transmission	77
4.19	Oscilloscope traces showing variations in cavity transmission over time . . .	78
4.20	Oscilloscope traces showing variations in cavity transmission and laser in- tensity	79
4.21	Frequency of 853 nm laser as a function of time	80
5.1	Diagram illustrating our Fabry-Perot cavity and the parameters relevant to critical coupling	82
5.2	Cavity transmission plotted vs. the loss α in a single pass through the in- tracavity medium.	83
5.3	Overview of experiment layout to measure absorption saturation in the $6s[3/2]_2^o$ to $6p[3/2]_2$ xenon transition	85
5.4	Overview of the Labview program used to control the experiment	86
5.5	Oscilloscope trace of the cavity transmission during an experiment run . . .	88
5.6	Raw data from absorption measurements using intracavity xenon atoms . . .	91
5.7	Absorption data for intra-cavity metastable xenon with input power levels of 0.5, 2, and 19 nW	93
6.1	Energy level diagram used for producing cross-phase shifts with metastable xenon gas in a cavity	97
6.2	Conceptual diagram of the system for measuring the cross-phase shift	99
6.3	Oscilloscope traces of balanced detector output during a calibration test of the experiment	101
6.4	Diagram of the optics used to couple light from an amplifier into single- mode polarization-maintaining fiber	102

6.5	Laboratory photo of the optics used to couple light from an amplifier into single-mode polarization-maintaining fiber	103
6.6	CCD images of the mode profile of an amplifier's emission	103
6.7	Illustration of the optics used in the laboratory to produce the probe field pulses	105
6.8	Illustration of the updated optics for producing the probe field pulses	105
6.9	Optics used to produce the probe field pulses with minimized leakage of narrowband probe light	106
6.10	Diagram of experiment layout for the cross-phase shift measurement	108
6.11	Plot of the frequency drift of a cavity resonance after receiving a delta function heating pulse	111
6.12	Data from our initial phase shift measurements	112
6.13	Experiment setup for two-photon absorption measurements	114
6.14	Sample of our two-photon absorption measurement results	114
6.15	Two-photon absorption and phase shift measurement data	116
6.16	Spurious feature in phase shift measurement data	117
6.17	Phase shift measurement data after the inclusion of a pair of narrowband optical filters	117
6.18	Illustration of the time evolution of a wavefront of the intracavity field . . .	123
6.19	Results from a sample run of the numerical simulation used to predict phase shift measurements	125
6.20	Combined phase shift measurement and theory results	126

7.1	Energy level diagram to be used for producing cross-phase shifts in the new cavity	129
7.2	Series of 4 photographs illustrating the design of the new cavity mount . . .	130
7.3	Closeup view of the cavity mirrors	131
7.4	Mirrors damaged after mounting in the steel mirror holders	132
7.5	Photo of the redesigned cavity mount, during the process of aligning the mirrors	133
7.6	Closeup photo illustrating the relative orientations of the mirrors after initial alignment	134
7.7	Photo of the cavity mirrors and their supporting structure	134

Chapter 1

Introduction

Compared with many other branches of physics, the theory of the behavior of light is quite elegant. In most day-to-day circumstances this behavior follows the relatively simple rules of classical optics, which are very well understood. Within the last century though, since the introduction of quantum mechanics, it has become apparent that these rules do not always apply. Appropriately engineered optical fields are capable of manifesting the phenomena of entanglement and quantum superposition in ways unexplainable by classical optics. One particularly notable example is the use of photons to violate the famous Bell inequality [1–3]. This and similar phenomena can be explained only by a new optical theory that follows the rules of quantum mechanics. The work of the scientific community to develop this theory and to examine its consequences led to the emergence of the field of quantum optics.

Quantum optics is the field of physics whose goal is the development of a more complete understanding of the behavior of light and its interaction with matter when quantum mechanical effects are taken into account. Initial research in this field was often driven by purely scientific interests, but in recent decades several new technologies have also been developed taking advantage of the quantum nature of light. Among these are systems for performing provably secure long-distance communications [4–7], ideas for building all-

optical quantum computers [8, 9], and ways of networking multiple quantum computers together to share resources [10–12].

Quantum states of light are particularly useful for playing the role of what are called “flying qubits,” i.e. physical systems in which bits of quantum information can be reliably transmitted from one place to another. One intuitive way to do this is to encode a quantum bit, or “qubit,” of information into the polarization of a single photon [11]. This can work quite well when experiments are carefully designed and losses are tightly controlled. In practical situations though there is a clear limit past which the use of single photons is no longer useful. Say for instance that an attempt is made to transmit quantum information by sending a single photon from point A (from a young lady named Alice) to point B (we can call him Bob). If along the way the photon happens to be absorbed or scattered outside of the transmission line, the attempted communication fails. This leads necessarily to an exponential decrease in the rate of quantum communication as the distance between Alice and Bob is increased [13, 14].

It is not too difficult to circumvent this problem if Alice can content herself sending only classical information. In that case she could encode the information into macroscopic, classical light pulses. These can be amplified with relatively little damage to the encoded information. A series of amplifiers, placed along the optical transmission line all the way from Alice to Bob, can make up for the scattering and absorption losses that the light pulses experience during transmission. In this way the information has a much easier time making it to all the way to Bob.

Single photons, however, cannot be amplified without destroying their unique quantum-mechanical properties, and maintaining these properties is essential if they are to be good carriers of quantum information. This preclusion of the use of amplifiers is one of the core problems for quantum communications: without something in the communications channel that can function like an amplifier, the rate of transmitting quantum informa-

tion drops off exponentially with increasing distance [15]. It is then natural to ask whether there may be other quantum states of light that can be used to communicate quantum information, but for which the use of amplifiers doesn't automatically destroy coherence. Recent work by our group suggested that using phase-entangled coherent states might possibly work [16]. A coherent state is a quantum mechanical representation of a classical laser pulse. Since classical light can pass through an amplifier relatively unharmed, it seemed not unreasonable to suppose that a pair of phase entangled classical light pulses might be able to pass through with relatively little degradation as well.

The potentially far-reaching applications of this idea made it quite appealing to our group as new research direction. Things became more difficult though when we started to think about how to generate a pair of phase-entangled coherent states. The simplest method required an extremely strong Kerr nonlinearity, so strong that a single photon in a control pulse could impart a noticeable phase shift on a coherent state [16]. The subfield of physics concerned with the production and application of single-photon nonlinearities is called quantum nonlinear optics. As a result of the potential applications for quantum communication our group began working in this field.

A great deal of work in quantum nonlinear optics has focussed on producing large single-photon cross-phase shifts, on the order of π radians [17–19]. A system capable of performing this task on-demand and with high fidelity would have numerous important applications in quantum communications and optical quantum computation [8, 11, 20–22]. Large single-photon cross-phase modulation has been produced in a number of different systems using quantum dots [23], single trapped atoms [12, 17, 24–26], clouds of cold atoms [18, 19, 27], and artificial atoms [28]. Warm atoms have been used as well, and while warm atom systems have some appeal for their relative experimental simplicity, results so far have been comparatively modest [29].

Many of these experimental works represent the best results achieved to-date, using sophisticated, state-of-the-art systems designed and built by research groups with decades of accumulated technical expertise in this field [17–19, 24, 26]. From the perspective of a relatively small research group with relatively little previous experience in this area of work, the prospect of building a new quantum nonlinear optical system was a daunting one. Typically, years of development and testing are required before such a system reaches a point at which it can compete with the state-of-the-art.

Fortunately for our group though, several recent theoretical results have shown that interesting and useful experiments in quantum information processing can be performed with nonlinearities significantly weaker than what is typically sought. In addition to their usefulness for generating phase entangled coherent states as discussed above, single-photon cross-phase shifts on the order of ~ 1 mrad could be useful for applications in photonic quantum computing and quantum non-demolition measurement [9, 16, 30]. Single-photon nonlinearities of roughly this size are commonly referred to in the literature as “weak nonlinearities.” Our group decided to pursue the development of a new system for performing quantum nonlinear optics experiments using weak nonlinearities. Our goal was to build a system that would be relatively simple and robust, compared with the sophisticated setups cited above, but still capable of producing single-photon cross-phase shifts on the order of ~ 1 mrad.

Many groups have used high-finesse optical cavities to increase the nonlinearity of atomic media. This has been done with single trapped atoms and cold atomic clouds [12, 17, 23–25]. Perhaps surprisingly, to the best of our knowledge high-finesse cavities have never been used in conjunction with a simple warm atomic vapor. This has been the case because most experiments in atom optics have used alkali atoms such as rubidium and sodium. These elements have convenient spectroscopic properties and strong transitions, but they are also highly reactive. They tend to adhere to optical surfaces and can quickly

degrade their performance. As a result, it has simply not been possible to use warm vapors with cavities of finesse greater than about 100 [31–33].

Our group has changed this. Rather than relying the alkali elements, we turned to metastable noble gas atoms as our nonlinear media. Metastable xenon in particular has optical properties similar to those of rubidium, but it is inert and does not damage sensitive cavity mirrors. Using metastable xenon in a high-finesse cavity has allowed us to produce optical nonlinearities at ultralow optical power levels with a relatively simple and robust setup [34, 35].

This work will be devoted to a more detailed description of our proposed system and of the results we have obtained with it so far. We begin in Chapter 2 with a brief introduction to the field of cavity quantum electrodynamics (cavity QED). In Chapter 3 we describe the spectroscopic properties of room-temperature xenon atoms, with an emphasis on those properties most relevant to the experimental work described in the following chapters. Chapter 4 explains the design and construction of our first, proof-of-principle high-finesse cavity system. Chapters 5 and 6 describe two of our most important experiments using this system. In Chapter 7 we provide details of a new cavity that we have recently built, which should bring our experiment into the regime of quantum nonlinear optics with weak nonlinearities. We close with a brief summary in Chapter 8.

Chapter 2

Optical Cavities and Cavity Quantum Electrodynamics

2.1 Introduction to Optical Cavities

Cavity quantum electrodynamics, or cavity QED, is a subfield of quantum optics focused on the study of the quantum mechanical interaction of light and matter inside of a high-finesse cavity. The word cavity in this context refers to a device that stores electromagnetic energy, whose operation depends on constructive interference between an input field and a stored field. There are many ways to build a cavity, from superconducting cavities that operate in the microwave regime [36] to optical whispering gallery mode resonators [37] and Fabry-Perot (FP) cavities built from high-quality bulk mirrors [38]. We will concentrate on optical Fabry-Perot cavities.

An illustration of a typical Fabry-Perot cavity is shown in Figure 2.1 (a). The device is made of a pair of mirrors, preferably highly-reflective mirrors with low absorption and scattering losses. These mirrors are positioned facing each other as shown. Intuitively, one would expect that an input light field incident on the cavity should simply be reflected.

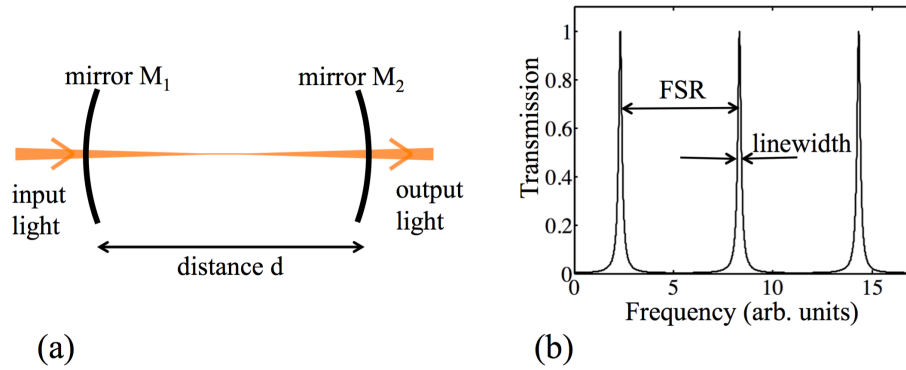


Figure 2.1: (a) Diagram of a general spherical-mirror optical cavity. (b) Transmission as a function of frequency for a typical ideal cavity.

However, assuming perfect, lossless mirrors it is possible for 100% of the input light intensity to be transmitted through the cavity.

As already mentioned, this counter-intuitive behavior depends on the constructive interference of the input light field with the field circulating inside the cavity. The system transmits only at discrete set of optical frequencies. These frequencies occur at regular intervals, separated by what is called the cavity's free spectral range (FSR). A typical cavity transmission spectrum is shown in Figure 2.1 (b).

The phenomenon of resonant transmission in an optical cavity can be understood with a relatively simple classical wave analysis. We will assume for simplicity that our cavity is built with plane mirrors, and that the input field is an infinite plane wave. When the input field first strikes the front mirror of a high-finesse FP cavity most of the incident intensity is reflected, but a small fraction is transmitted through the mirror. This transmitted beam travels across the cavity, reflects from the opposite mirror, then returns to the front mirror and reflects again. A small amount of the energy in the intracavity field leaks out of the cavity through the mirrors during this round-trip, but when the mirrors are highly reflecting and of high quality this loss is relatively small. Then during the following pass there are two fields propagating together: one directly transmitted through the first mirror and another that has already completed a full round trip inside the cavity. This process

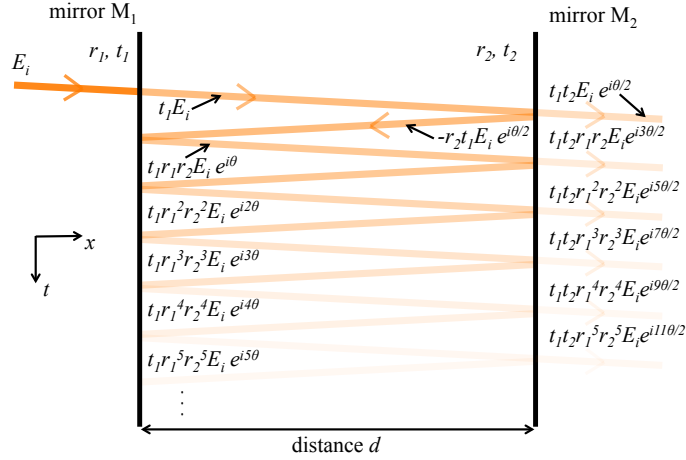


Figure 2.2: Illustration of resonant light transmission in an optical cavity.

repeats ad infinitum. In the limit of a long time after the input light is first turned on (assuming a continuous-wave input), the field amplitude within the cavity can be written as a sum of an infinite number of component fields, each one having travelled back-and-forth within the cavity a different number of times, as illustrated in Figure 2.2. This produces an infinite geometric series, leading to a nice, clean result.

Ignoring losses due to absorption or diffraction, the transmitted field amplitude from Figure 2.2 is

$$E_t = t_1 t_2 E_i e^{i\theta/2} \sum_{k=0}^{\infty} (r_1 r_2 e^{i\theta})^k = \frac{t_1 t_2 e^{i\theta/2}}{1 - r_1 r_2 e^{i\theta}} E_i, \quad (2.1)$$

for mirrors with amplitude reflection coefficients r_1 and r_2 , and transmission coefficients t_1 and t_2 . The parameter $\theta = 2nkd$ represents the phase accumulated by the beam during one round trip inside the cavity, where n is the index of refraction of the intracavity medium and k is the wavenumber of the input light. The transmitted intensity is then given by

$$I_t = \frac{T_1 T_2}{1 + R_1 R_2 - 2\sqrt{R_1 R_2} \cos\theta} I_i, \quad (2.2)$$

where R_1 , R_2 , T_1 , and T_2 are the reflectances and transmittances of the two mirrors, and I_i is the input intensity. We have assumed that r_1 , r_2 , t_1 , and t_2 are all real, since the inclusion of the phases of these coefficients leads only to a constant offset in the value of θ . In the special case of identical mirrors, the equation for the transmitted intensity reduces to

$$I_t = \frac{T^2}{1 + R^2 - 2R\cos\theta} I_i. \quad (2.3)$$

The maxima and minima of the transmission function occur at $\theta_{max} = m2\pi$ and $\theta_{min} = \pi + m2\pi$, for any integer m . This leads to $I_{t,max} = I_i$ and $I_{t,min} = \frac{(1-R)^2}{(1+R)^2} I_i$.

The free spectral range of the cavity can be found from the condition that the change of θ between two adjacent cavity transmission peaks is 2π : $FSR = \frac{c}{2nd}$. The full-width-at-half-max (FWHM) of the transmission peaks described in Eq. 2.3 is related to the free spectral range by $FWHM = \frac{FSR}{\mathcal{F}}$, where the quantity \mathcal{F} is called the cavity's finesse. In the limit of highly-reflecting mirrors the finesse is given by

$$\mathcal{F} = \frac{\pi(R_1 R_2)^{1/4}}{1 - (R_1 R_2)^{1/2}}. \quad (2.4)$$

The finesse represents the number of round trips an intracavity field makes before its intensity decays to a fraction $e^{-2\pi}$ of its original value.

Fabry-Perot cavities have a wide variety of applications. For instance, they are convenient spectral filters, due to the strong frequency selectivity of their transmission profiles. Due to their sensitivity to slight changes in cavity length they can also be well suited to the task of measuring very small displacements, of order $\ll 1 \mu m$. These applications use the cavity transmission function as a measuring tool. In contrast, we are primarily interested in these structures because of the effects they have on atoms and fields inside the resonators themselves.

As an initial example, let's consider the amplitude of an intracavity field. For simplicity we will assume for the remainder of this section that the mirrors are identical and lossless. The maximum amplitude of the transmitted electric field can be found from Eq. 2.1:

$$E_t = \frac{t^2 e^{i\theta/2}}{1 - r^2 e^{i\theta}} E_i \quad (2.5)$$

$$|E_{t,max}| = |E_i|,$$

where E_i is the input field amplitude. The intracavity field amplitude E_c is related to the transmitted amplitude by $E_t = tE_c$. Hence the maximum intracavity field is $E_{c,max} = E_i/t$. For a high quality set of cavity mirrors, t can be as small as $t = \sqrt{.00001} \approx 0.003$. In this case the field inside the cavity is 300 times stronger than it is at the input. This provides a massive advantage for nonlinear optical processes. For instance, the efficiency of the second harmonic generation process is typically proportional to the intensity of the driving light field. Placing the nonlinear medium inside of a high-finesse cavity could increase the efficiency by up to a factor of $1/t^2 \approx 100,000$!

Consider another example: say we want to cause a weak light field to interact with a single atom that we've managed to capture in an optical trap. We could try simply placing the atom in the path of the field, but in that case the passing photons would each have only a very small probability of interacting with the atom. If we were to place the atom within a high quality cavity, however, the situation would be different. Taking the above value of $t^2 \approx 10^{-5}$, a photon inside a Fabry-Perot cavity would bounce back and forth between the two mirrors on the order of $1/t^2 \approx 100,000$ times before leaving the cavity. This would give it 100,000 chances to interact with the atom, and as a result that interaction could become roughly 100,000 times more likely to occur. This is the kind of application we want to pursue.

2.2 Transverse Mode Structure of a Fabry-Perot Cavity

The behavior of optical cavities discussed in Section 2.1 depends on the coherent superposition of multiply-reflected versions of an incident field. The cavity and the input field need to be oriented correctly for this superposition to occur. The above analysis assumed that the input fields were infinite plane waves, and that the mirrors were infinitely large and flat, and aligned with perfect precision. In practice of course this is never the case. For a plane-mirror Fabry-Perot cavity finite beam diameters and mirror sizes lead inevitably to diffraction losses. Consequently, FP cavities are typically constructed with spherical concave mirrors.

A spherical mirror cavity has the advantage that, for a correct choice of the cavity size and mirror curvatures, fields circulating within the cavity tend to be confined near the optic axis. A cavity configuration which supports this confinement is called a *stable* configuration, whereas one that does not support it is called *unstable*. The conditions for the stability of a cavity configuration can be determined through a ray-tracing analysis [39]. We will skip the derivation for the sake of brevity, and simply state the stability criterion:

$$0 \leq \left(1 + \frac{d}{R_1}\right) \left(1 + \frac{d}{R_2}\right) \leq 1, \quad (2.6)$$

where d is the distance between the centers of the mirrors, and R_1 and R_2 are their radii. In this work we will consider only cavities in which the mirrors are identical. In that case this relationship simplifies to

$$0 \leq \left(\frac{d}{-R}\right) \leq 2, \quad (2.7)$$

where R is negative for concave and positive for convex mirrors. A symmetric, concave spherical mirror cavity will always be stable as long as the distance between mirrors is not more than twice the mirror radius of curvature.

In order to couple light into the cavity we need to know the transverse intensity distributions that correspond to the resonant modes. To constitute a transverse resonant mode of a Fabry-Perot cavity, the field distribution needs to allow multiple reflections to coherently interfere. This means that the shape of the distribution after propagating back-and-forth across the cavity needs to exactly match the distribution of the field at the cavity input. The Hermite-Gaussian modes satisfy this condition for a spherical mirror cavity [40]. (The Laguerre-Gaussian modes work as well, in the ideal case of perfect cylindrical symmetry. Small imperfections in the geometry of the mirror substrates can easily break this symmetry though, in which case the observed mode structure will be Hermite-Gaussian.) The derivation and the mathematical forms of these modes can be found in reference [40], or in a similar standard textbook on laser physics. When the intensity distribution of an input field matches that of a particular transverse mode, interference occurs and the analysis of Section 2.1 correctly describes the behavior of the cavity.

For applications in nonlinear optics it is generally best to use the mode with the tightest beam confinement. Tighter confinement results in larger field amplitudes and hence stronger nonlinearities. The fundamental or 0th-order mode is the most suitable for this purpose. It is called the TEM₀₀ mode. It is a simple 2-dimensional Gaussian intensity profile, given by

$$I(\vec{r}) = I_0 \left(\frac{W_0}{W(z)} \right)^2 e^{[-2(x^2+y^2)/W^2(z)]}, \quad (2.8)$$

where $W(z)$ is the radius of the beam at longitudinal position ‘ z ’ and W_0 is the radius at the beam waist (the location where the beam is narrowest). $W(z)$ for a Gaussian beam is given by

$$W(z) = W_0 \sqrt{1 + \left(\frac{z}{z_0} \right)^2}, \quad (2.9)$$

where z_0 is the Rayleigh range. The Rayleigh range is the longitudinal position at which the wavefronts are most strongly curved, and it is given by $z_0 = \frac{\pi W_0^2}{\lambda}$, with λ the wavelength of the radiation [39]. These relationships are illustrated in Figure 2.3. Further details can

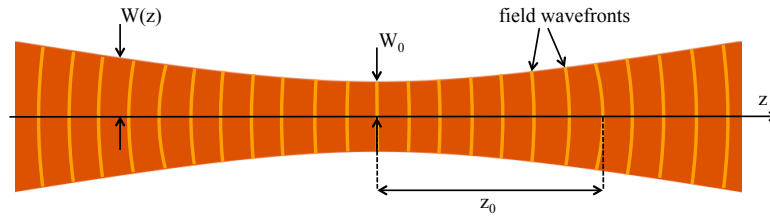


Figure 2.3: Illustration of a Gaussian beam profile and phase wavefronts as a function of longitudinal distance, z .

be found in any textbook on laser physics. The simple Gaussian shape of these modes is fortunate for experimental implementations as it matches very well the field distribution within a single-mode optical fiber.

2.3 Cavity QED and Quantum Nonlinear Optics

The regime of classical nonlinear optics is interesting in its own right, with many practical applications, but we are more interested in the use of optical cavities in the field of cavity QED. This field explores the interaction of quantum light fields with atoms, molecules, and other quantum-sized objects inside optical cavities. In this regime, a classical wave analysis is not sufficient to completely describe the dynamics. We need another, fully quantum mechanical model.

We will start our development of this model by taking a look at the quintessential cavity QED system: a single 2-level atom sitting motionless inside a single-mode optical cavity. This model, though somewhat idealized, describes many real experimental systems with a high degree of accuracy. Though most physically realizable cavities support a very large number of modes, the 2-level atom inside the cavity has only one resonance frequency. Interactions between the atom and the cavity will generally be very weak unless the cavity

and atomic frequencies are quite close. Hence it is usually assumed that only one of the cavity modes is tuned close enough to the atomic resonance to result in an appreciable interaction, and all other modes are ignored.

As with all other quantum mechanical analyses, we begin by writing the Hamiltonian that describes this system,

$$\begin{aligned}\hat{H} &= \frac{1}{2}\hbar\omega_a\hat{\sigma}_z + \hbar\omega_c\hat{a}^\dagger\hat{a} + \hat{E} \cdot \hat{\mu} \\ &= \frac{1}{2}\hbar\omega_a\hat{\sigma}_z + \hbar\omega_c\hat{a}^\dagger\hat{a} + \hbar\left(\mathcal{E}\hat{a}^\dagger + \mathcal{E}^*\hat{a}\right)\hat{\mu}.\end{aligned}\tag{2.10}$$

The \hat{a}^\dagger and \hat{a} are the raising and lowering operators for the cavity mode. The atomic resonance frequency is given by ω_a , and ω_c is the frequency of the relevant cavity mode. For the sake of simplicity we have chosen to consider only one polarization. The \hat{E} and $\hat{\mu}$ are the electric field and atomic dipole moment operators, respectively. \mathcal{E} and \mathcal{E}^* are the constants of proportionality relating \hat{E} to the creation and annihilation operators \hat{a} and \hat{a}^\dagger for the electromagnetic field, respectively [41]. For a two-level atom the dipole operator has the form $\hat{\mu} = \mu_{12}\hat{\sigma}_{12} + \mu_{12}^*\hat{\sigma}_{21}$, where $\mu_{12} = \langle 1_a | \hat{\mu} | 2_a \rangle$, with $|i_a\rangle$ indicating an atom in state i . The operators $\hat{\sigma}_{21}$ and $\hat{\sigma}_{12}$ take the atom from its ground state $|1_a\rangle$ to the excited state $|2_a\rangle$ and vice versa, respectively. From here on we will use the notation $\hat{\sigma}_{ij} \equiv |i_a\rangle\langle j_a|$ when referring to atomic operators. We use $\hat{\sigma}_z$ for the atomic Pauli z operator, given by $\hat{\sigma}_z = \hat{\sigma}_{22} - \hat{\sigma}_{11}$. Substituting this into the above,

$$\hat{H} = \frac{1}{2}\hbar\omega_a\hat{\sigma}_z + \hbar\omega_c\hat{a}^\dagger\hat{a} + \hbar\left(\mathcal{E}\hat{a}^\dagger + \mathcal{E}^*\hat{a}\right)\left(\mu_{12}\hat{\sigma}_{12} + \mu_{12}^*\hat{\sigma}_{21}\right).\tag{2.11}$$

As basis states we will use the eigenstates of the interaction-free part of the Hamiltonian, $H_0 = \frac{1}{2}\hbar\omega_a\hat{\sigma}_z + \hbar\omega_c\hat{a}^\dagger\hat{a}$, consisting of the atomic ground and excited states along with the photonic excitation number states. The state of the coupled atom-cavity system

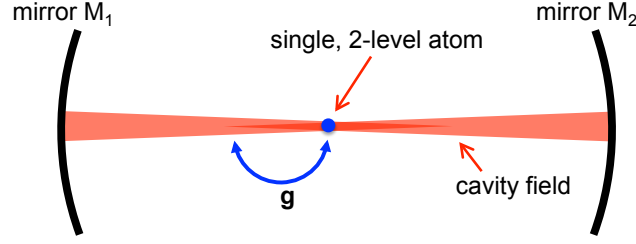


Figure 2.4: Conceptual diagram of the Jaynes-Cummings model for a 2-level atom in an optical cavity. The parameter g describes the coupling rate between atomic and cavity excitations.

can then be written as a product of the atomic and photonic parts: $|i_a, j_c\rangle \equiv |i_a\rangle |j_c\rangle$, where $|j_c\rangle$ indicates the state in which the cavity mode contains j photons.

Now we apply the rotating wave approximation. This approximation is valid as long as the optical field is not extremely strong, and the relation $|\omega_a - \omega_c| \ll \omega_a + \omega_c$ is satisfied. This allows us to neglect the so-called counterrotating terms, and we are left with:

$$\hat{H} = \frac{1}{2}\hbar\omega_a\hat{\sigma}_z + \hbar\omega_c\hat{a}^\dagger\hat{a} + \hbar\left(\mu_{12}\mathcal{E}\hat{\sigma}_{12}\hat{a}^\dagger + \mu_{12}^*\mathcal{E}^*\hat{a}\hat{\sigma}_{21}\right). \quad (2.12)$$

We will assume without loss of generality that $\mu_{12}\mathcal{E}$ is real and positive. Then $\mu_{12}\mathcal{E}$ and $\mu_{12}^*\mathcal{E}^*$ can be absorbed into a new constant g , which describes the rate of coupling between the cavity field and the atomic excitation. We now have

$$\hat{H} = \frac{1}{2}\hbar\omega_a\hat{\sigma}_z + \hbar\omega_c\hat{a}^\dagger\hat{a} + \hbar g\left(\hat{\sigma}_{12}\hat{a}^\dagger + \hat{a}\hat{\sigma}_{21}\right). \quad (2.13)$$

This Hamiltonian includes terms describing a free 2-level atom ($\frac{1}{2}\hbar\omega_a\hat{\sigma}_z$) and a free single mode of the optical field ($\hbar\omega_c\hat{a}^\dagger\hat{a}$), along with an interaction term $\hbar g\left(\hat{\sigma}_{12}\hat{a}^\dagger + \hat{a}\hat{\sigma}_{21}\right)$. The interaction term causes excitations to be exchanged between the atom and the field. This is the familiar Jaynes-Cummings model of quantum optics [42], illustrated in Figure 2.4.

There is a great mass of literature pertaining to the Jaynes-Cummings model, some works calculating solutions for specific circumstances and initial conditions, others produc-

ing generalizations and/or extensions of the model. For a couple of examples see [43–45]. Related experimental works include [46–48], and many others. We, however, are interested primarily in the use of cavity QED as a tool for nonlinear quantum optics, so we will pass over the grand majority of this literature and concentrate on the results most relevant to our work.

In particular, there is one important result that can be straightforwardly derived from the Hamiltonian of Eq. 2.12. We start by diagonalizing this Hamiltonian and calculating its normal mode energies. The Hilbert space of the Hamiltonian Eq. 2.12 is infinite dimensional, as there is in principle no limit on the number of photons allowed in the cavity mode. However, notice that the interaction term only links states with the same total number of excitations. For example, this term can transform the state $|1_a, 1_c\rangle$ into the state $|2_a, 0_c\rangle$, but it cannot transform either of these into the state $|2_a, 1_c\rangle$.

Our next step is to write the Hamiltonian in matrix form. First we define the state vectors as

$$\begin{aligned}
|\psi\rangle &= c_{1,0} |1_a, 0_c\rangle + c_{2,0} |2_a, 0_c\rangle + c_{1,1} |1_a, 1_c\rangle + c_{2,1} |2_a, 1_c\rangle + \dots \\
&\quad + c_{1,2} |1_a, 2_c\rangle + c_{2,2} |2_a, 2_c\rangle + c_{1,3} |1_a, 3_c\rangle + c_{2,3} |2_a, 3_c\rangle + \dots \quad (2.14) \\
|\psi\rangle &= \left[c_{1,0}, c_{2,0}, c_{1,1}, c_{2,1}, c_{1,2}, c_{2,2}, c_{1,3}, c_{2,3}, \dots \right]^T.
\end{aligned}$$

Writing the Hamiltonian in this basis, we see that it is block diagonal:

$$\hat{H} = \hbar \begin{bmatrix} -\frac{1}{2}\omega_a & 0 & 0 & 0 & 0 & \dots \\ 0 & \frac{1}{2}\omega_a & g & 0 & 0 & \dots \\ 0 & g & -\frac{1}{2}\omega_a + \omega_c & 0 & 0 & \dots \\ 0 & 0 & 0 & \frac{1}{2}\omega_a + \omega_c & \sqrt{2}g & \dots \\ 0 & 0 & 0 & \sqrt{2}g & -\frac{1}{2}\omega_a + 2\omega_c & \dots \\ \vdots & \vdots & \vdots & \vdots & \vdots & \ddots \end{bmatrix}. \quad (2.15)$$

It suffices then to diagonalize the Hamiltonian within the subspace of each block, taking them one at a time. For the sake of illustration, we will assume now that $\omega_a = \omega_c \equiv \omega$. This means that, in the absence of the interaction term, states $|1_a, n_c\rangle$ and $|2_a, (n-1)_c\rangle$ are eigenstates of the Hamiltonian with identical energy. In the n^{th} block (with n any integer ≥ 1), we have

$$\hat{H}_{\text{block } n} = \hbar \begin{bmatrix} (n - \frac{1}{2}) \omega & \sqrt{n}g \\ \sqrt{n}g & (n + \frac{1}{2}) \omega \end{bmatrix}. \quad (2.16)$$

For the eigenstates and eigenenergies we find

$$\begin{aligned} |\psi_{n,+}\rangle &= \frac{1}{\sqrt{2}} (|1_a, n_c\rangle + |2_a, (n-1)_c\rangle) \\ |\psi_{n,-}\rangle &= \frac{1}{\sqrt{2}} (|1_a, n_c\rangle - |2_a, (n-1)_c\rangle) \\ \lambda_{\pm} &= \hbar \left(n - \frac{1}{2} \right) \omega \pm \hbar \sqrt{n}g. \end{aligned} \quad (2.17)$$

Notice that the interaction terms split the atom-cavity degeneracy. An interesting consequence of the energy splitting can be seen by calculating the system evolution from a given set of initial conditions. Assume that at time $t = 0$ the system is in state $|\psi_0\rangle = |1_a, n_c\rangle$. Note from Eq. 2.17 that

$$\begin{aligned} |1_a, n_c\rangle &= \frac{1}{\sqrt{2}} (|\psi_{n,+}\rangle + |\psi_{n,-}\rangle) \\ |2_a, (n-1)_c\rangle &= \frac{1}{\sqrt{2}} (|\psi_{n,+}\rangle - |\psi_{n,-}\rangle). \end{aligned} \quad (2.18)$$

Integrating the Schrödinger equation gives $|\psi(t)\rangle = e^{-i\hat{H}t/\hbar} |\psi_0\rangle$. Setting $|\psi_0\rangle = |1_a, n_c\rangle$ we find

$$|\psi(t)\rangle = e^{-i(n-1/2)\omega t} \left[\cos(\sqrt{n}gt) |1_a, n_c\rangle - i \sin(\sqrt{n}gt) |2_a, (n-1)_c\rangle \right]. \quad (2.19)$$

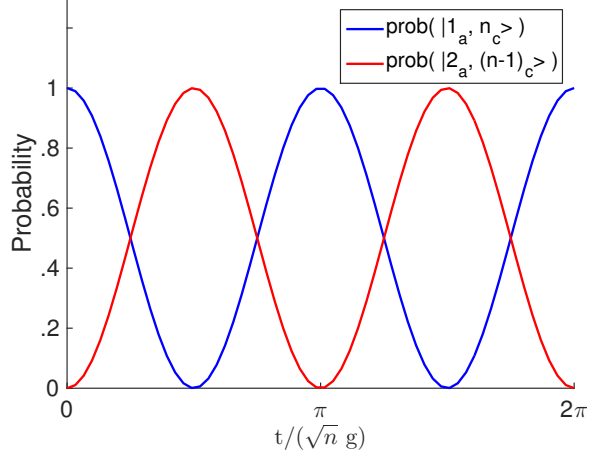


Figure 2.5: Probabilities of finding the coupled atom-cavity system in either of the states $|1_a, n_c\rangle$ or $|2_a, (n-1)_c\rangle$ as a function of time. As time passes one quantum of energy is continually swapped back-and-forth between the atom and the cavity.

At time t the system has probability $\cos^2(\sqrt{n}gt)$ of being found in state $|1_a, n_c\rangle$, and probability $\sin^2(\sqrt{n}gt)$ of being found in state $|2_a, (n-1)_c\rangle$. One of the n_c energy quanta in the system continually flops back-and-forth between the atom and the cavity. This phenomenon is referred to as “Rabi flopping” or “Rabi oscillation.” Such oscillations occur any time a 2-level quantum system is driven near one of its transition resonances by an external force or by coupling to another system. In our case the driving comes from the atom’s coupling with the cavity field. Figure 2.5 illustrates the time evolution of the state probabilities, given by Eq. 2.19.

Rabi oscillations are an interesting, but not a specifically quantum-mechanical phenomenon. The unique quantum-mechanical part of the dynamics in this case comes from the factor of \sqrt{n} in the splitting between the two eigenstates given in Eq. 2.17. For a classical system the scaling of the energy splitting between eigenstates goes as $\sim ng$, rather than $\sim \sqrt{n}g$. This facet of the Jaynes-Cummings model has been recognized as an important signature of quantum dynamics [49, 50]. More recently it has also been shown that this can also be a useful tool in quantum nonlinear optics.

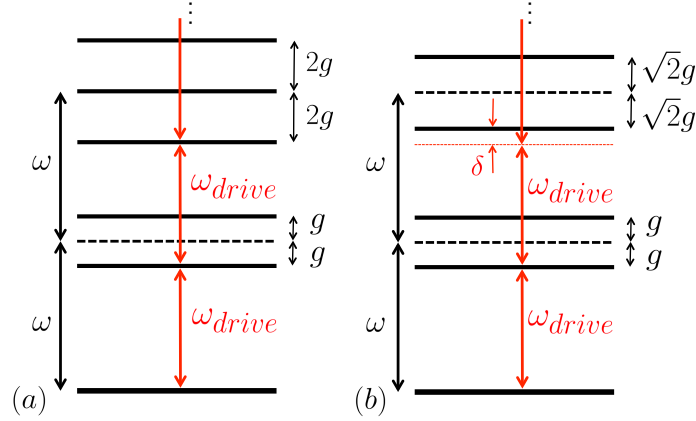


Figure 2.6: Energy level diagrams for (a) a generic system of macroscopic coupled oscillators, and (b) a single atom coupled to a cavity as described in the text. Note that the difference in energy of the split states in (a) is proportional to the number of excitations, whereas in (b) the dependence is nonlinear.

Figure 2.6 shows energy level diagram for the system of a single atom in a cavity as described above, and for a system composed of a macroscopic oscillator in a cavity (the macroscopic oscillator could be, for instance, a atomic cloud made up of a very large number of atoms). Consider the case in which each of these two systems is driven by a classical light field. Tuning the frequency of the driving field to $\omega_{drive} = (\omega - g)$, for example, would couple the ground and lowest excited states, causing the system to undergo transitions between them. In the classical case of Figure 2.6 (a), the driving field would also couple into the lower state of the second excitation manifold, and of the third, and so on. As a result the macroscopic oscillator would tend over time to evolve into an essentially classical state with many excitations. In the case illustrated in Figure 2.6 (b) though, the driving field is detuned by an amount $\delta = (2 - \sqrt{2})g$ from the transition between the first and second excitation manifolds. This detuning suppresses the probability for the system to absorb more than one excitation. As a result, driving a single atom cavity system with a classical field tends to place the system in a single-excitation state. This single excitation can then be coupled out through the cavity mirrors, allowing the system to function as a true single-photon source [51–53].

This may not sound like an impressive accomplishment. After all, a typical \$2 light bulb produces on the order of 10^{19} photons per second. These photons are emitted at random times with randomized quantum phases in what is called a thermal state. The unique advantage of a single-photon source though is that, ideally, photons are controllably produced one-at-a-time in a well-defined pure quantum state. These single-photon states are extremely useful in many branches of quantum optics, but they are also notoriously difficult to produce [54–62]. The ability to build a true single-photon source illustrates the unique power of cavity QED for quantum nonlinear optics.

As an aside, another interesting consequence of the nonlinear dependence of the splitting on excitation number is the presence of what are called “collapse and revival” phenomena in the population dynamics. A fair amount of literature comprising theoretical studies of this and similar phenomena was produced in the 1980’s and 90’s. For those interested in learning about this topic a good place to start is [44].

2.4 Theoretical Description of Dissipation and Dephasing

A great quantity of valuable work has come from examining the Jaynes-Cummings model of cavity QED, but the model itself cannot possibly provide a complete description of a real-world quantum system. In the real world, individual atoms and field modes are not free to interact with each other uninterrupted for eternity. Over time they system will tend to spontaneously relax to its ground state, either via atomic spontaneous emission into free space outside of the cavity mode, or through photon loss at the cavity mirrors. Additionally, realistic systems always interact in some measure with their surrounding environment, leading to entanglement between the simple quantum system and the highly complex dynamics of the environment. A system that interacts with its environment in this way is called an open quantum system. Entanglement between the system and its environment leads to the loss of information regarding sensitive quantum correlations. This phenomenon is called

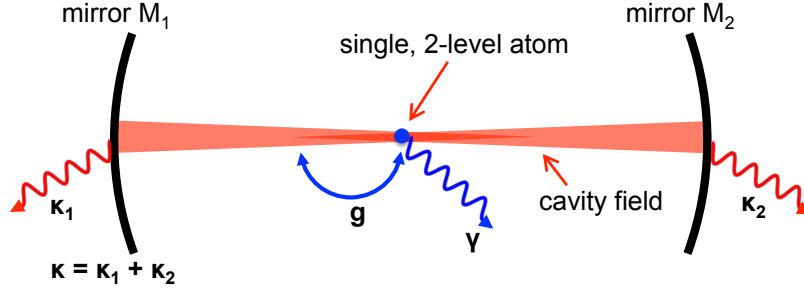


Figure 2.7: Conceptual diagram for an open quantum system of a 2-level atom in an optical cavity. The parameter g describes the coupling rate between atomic and cavity excitations. The rate of photon loss due to atomic spontaneous emission is given by γ . The κ_1 and κ_2 are the loss rates due to transmission through or imperfections of cavity mirrors 1 and 2, respectively. The total rate of loss from both mirrors taken together is $\kappa = \kappa_1 + \kappa_2$.

decoherence [63]. The effect of decoherence on a quantum system can be conceptualized as a stochastic randomization of the relative phases of quantum states. Over time this effect typically destroys the unique signatures of quantum mechanical dynamics.

Figure 2.7 illustrates a realistic cavity QED system subjected to the common sources of dissipation and decoherence. The ability of such a system to perform useful operations in quantum nonlinear optics is often characterized by a parameter called the cooperativity [12],

$$\eta = \frac{g^2}{2\kappa\gamma}. \quad (2.20)$$

A cavity QED system with cooperativity $\eta \gg 1$ will be capable of producing strong nonlinear optical effects at the single-photon level, while a cavity with $\eta \ll 1$ can be expected to produce only very weak single-photon nonlinearities. Thus it has been the goal of many research groups to build a cavity system with the largest possible value of η . This is accomplished by maximizing the coherent coupling rate g while keeping the dissipation rates κ and γ at a minimum.

For the moment though our primary concern is not the mitigation of the effects of dissipation and decoherence, but the proper description of them. To accomplish this task we need to apply the density operator formalism to our work with cavity QED and the

Jaynes-Cummings model. This formalism provides a more complete description of quantum systems than the state vector approach used above. The above analysis can describe the time evolution of quantum states when they and their relative phases can be known exactly, i.e. when they are “pure” states. This works in the ideal world of theory, but in the real world nonidealities and classical uncertainties need to be accounted for. The density operator allows us to describes systems for which the the quantum state is not precisely known.

Suppose we have an ensemble of identical systems for which the exact quantum states are unknown. Suppose though that we know that each system has probability p_1 of being in state $|\psi_1\rangle$, probability p_2 of being in state $|\psi_2\rangle$, etc. The (p_1, p_2, \dots) here are classical probabilities, not quantum probability amplitudes. The density operator for this ensemble is defined as

$$\hat{\rho} = \sum_k p_k |\psi_k\rangle\langle\psi_k|. \quad (2.21)$$

In an n -dimensional quantum system with the states written as column vectors of length n , as in Eq. 2.14, $\hat{\rho}$ can be written as an $n \times n$ matrix. In this form it is often referred to as the “density matrix.” The density operator is Hermitian, as clearly seen from Eq. 2.21.

Measurement results in quantum mechanics are probabilistic in nature. As a result, in order to obtain accurate information about the state of a quantum system one needs to have access to a large ensemble of identical copies of the system. Having many copies allows many measurements to be performed, and averages to be taken. Knowledge of the density operator is sufficient to completely describe any such ensemble. That is, if any piece of information about the state of a quantum system can be gained by any combination of manipulations and measurements on an ensemble of identical copies, this same information can be derived from the density operator.

A potential disadvantage of the density operator is that it can be difficult to properly conceptualize, and that calculations using this more complete formalism are often signif-

icantly more involved than they would be using Hamiltonian dynamics with pure states. The great advantage of this more difficult formalism though is that it allows us to directly describe interactions which gradually transform pure quantum states into classical mixtures of states through decoherence.

The master equation describing the time evolution of the density matrix is composed of two separate parts: a unitary part and a non-unitary part. The unitary part can be derived by calculating the evolution of the states $|\psi_k\rangle$ using the Schrödinger equation, $i\hbar \frac{\partial}{\partial t} |\psi_k(t)\rangle = \hat{H} |\psi_k(t)\rangle$. The result is called the Von Neumann equation:

$$\left(\frac{d\hat{\rho}}{dt}\right)_U = -\frac{i}{\hbar} [\hat{H}, \hat{\rho}], \quad (2.22)$$

where the brackets designate the commutator, $[\hat{H}, \hat{\rho}] \equiv \hat{H}\hat{\rho} - \hat{\rho}\hat{H}$, and \hat{H} is the Hamiltonian for the system. The derivation of the non-unitary part is somewhat more involved, and again we will simply skip to the result describing a single two-level atom in a cavity. We have

$$\begin{aligned} \left(\frac{d\hat{\rho}}{dt}\right)_{NU} = & -\gamma (\hat{\sigma}_{21}\hat{\sigma}_{12}\hat{\rho} - 2\hat{\sigma}_{12}\hat{\rho}\hat{\sigma}_{21} + \hat{\rho}\hat{\sigma}_{21}\hat{\sigma}_{12}) - \dots \\ & - \kappa (\hat{a}^\dagger\hat{a}\hat{\rho} - 2\hat{a}^\dagger\hat{\rho}\hat{a} + \hat{\rho}\hat{a}^\dagger\hat{a}), \end{aligned} \quad (2.23)$$

where γ is the rate of atomic spontaneous emission into modes other than the cavity mode, and κ is the rate of photon loss from the cavity [64]. Both atomic spontaneous emission and photon loss from the cavity lead to an interaction between the quantum system and the environment. Hence, in addition to leaking energy out of the system, these processes cause decoherence. The two terms of Eq. 2.23 describe the energy relaxation process (i.e. their action on $\hat{\rho}$ performs the transformations $|2_a\rangle \rightarrow |1_a\rangle$, and $|n_c\rangle \rightarrow |(n-1)_c\rangle$) and they account for the decoherence associated with it.

In addition to this there are other, non-dissipative processes that produce dephasing as well. For example, in gasses at sufficiently high densities collisions between atoms or

molecules lead to additional decoherence. These effects are small in the vacuum environments used in our experiments, however, so for the remainder of this work we will neglect this and all similar sources of decoherence. Adding Eqs. 2.22 and 2.23 we have [64]

$$\begin{aligned} \frac{d\hat{\rho}}{dt} = & -\frac{i}{\hbar} [\hat{H}, \hat{\rho}] - \gamma (\hat{\sigma}_{21}\hat{\sigma}_{12}\hat{\rho} - 2\hat{\sigma}_{12}\hat{\rho}\hat{\sigma}_{21} + \hat{\rho}\hat{\sigma}_{21}\hat{\sigma}_{12}) - \dots \\ & - \kappa (\hat{a}^\dagger \hat{a} \hat{\rho} - 2\hat{a}^\dagger \hat{\rho} \hat{a} + \hat{\rho} \hat{a}^\dagger \hat{a}). \end{aligned} \quad (2.24)$$

This is the Lindblad master equation for $\hat{\rho}$. It is valid within the Markov approximation, i.e. when the environment effectively does not contain any record of the state of the quantum system at previous times. We choose this form because of its relative simplicity, because it is very widely used, and because it accurately describes the evolution of nearly all experimental systems in quantum optics. Once the time evolution has been calculated and the density operator has been found at time t , the expectation value for any observable \hat{A} at that time can be calculated from

$$\langle \hat{A}(t) \rangle = \text{Tr}[\rho(t) A]. \quad (2.25)$$

To further illustrate the density matrix formalism, we will now assume that the intracavity fields are classical. The Hamiltonian and master equation for this case can be found by replacing the electric field operator in Eq. 2.10 with the classical electric field $E(t) = E_0 e^{-i\omega_c t} + E_0^* e^{i\omega_c t}$, and removing the terms that describe the evolution of the field's quantum state. We obtain

$$\hat{H} = \frac{1}{2} \hbar \omega_a \hat{\sigma}_z + \left(E_0 e^{-i\omega_c t} + E_0^* e^{i\omega_c t} \right) \cdot \hat{\mu}, \quad (2.26)$$

where $E(t) = E_0 e^{-i\omega_c t}$ is the complex amplitude of the classical light field. Analogously with the quantum-mechanical case above, we assume without loss of generality that E_0 and

μ_{12} are real and positive. Then applying the rotating wave approximation we obtain

$$\hat{H} = \frac{1}{2}\hbar\omega_a\hat{\sigma}_z + \mu_{12}E_0 (e^{i\omega_c t}\hat{\sigma}_{12} + e^{-i\omega_c t}\hat{\sigma}_{21}). \quad (2.27)$$

The master equation now is

$$\frac{d\hat{\rho}}{dt} = -\frac{i}{\hbar} [\hat{H}, \hat{\rho}] - \gamma (\hat{\sigma}_{21}\hat{\sigma}_{12}\hat{\rho} - 2\hat{\sigma}_{12}\hat{\rho}\hat{\sigma}_{21} + \hat{\rho}\hat{\sigma}_{21}\hat{\sigma}_{12}), \quad (2.28)$$

since we no longer need to account for the evolution of the quantum state of the light field. This master equation describes the evolution of a single 2-level atom under the influence of a classical light field.

When written in its current form, the meaning of the non-unitary part of Eq. 2.28 may be difficult to conceptualize. It can be made more transparent by writing the differential equations for each component of $\hat{\rho}$ explicitly. We choose the basis in which the atomic energy eigenstates are

$$\begin{aligned} |1_a\rangle &= \begin{bmatrix} 1 & 0 \end{bmatrix}^T \\ |2_a\rangle &= \begin{bmatrix} 0 & 1 \end{bmatrix}^T, \end{aligned} \quad (2.29)$$

in which case the density operator takes the form

$$\hat{\rho} = \begin{bmatrix} \rho_{11} & \rho_{12} \\ \rho_{21} & \rho_{22} \end{bmatrix}. \quad (2.30)$$

The diagonal elements ρ_{11} and ρ_{22} indicate the probability of finding the atom in states $|1_a\rangle$ and $|2_a\rangle$, respectively. If the atom is measured in this basis it must always be found in one of these two states, so we will always have $\rho_{11} + \rho_{22} = 1$. It is a general property of all density matrices that in any basis the sum of the diagonal elements is equal to 1, i.e. $\text{Tr}[\hat{\rho}] = 1$. The off-diagonal elements of $\hat{\rho}$ indicate the degree of quantum coherence present in the

system between these two states. For our simple two-state model, a pure state with perfect coherence would have $|\rho_{12}| = |\rho_{21}| = \sqrt{\rho_{11}\rho_{22}}$. Dissipation removes energy from the system, causing it to evolve over time into a lower-energy state (assuming that there are no thermal or other sources pumping energy back in). In our model this will tend to gradually remove population from ρ_{22} and place it into ρ_{11} . Decoherence effects on the other hand leave the diagonal elements of $\hat{\rho}$ unchanged but reduce the magnitudes of the off-diagonal elements.

The equations of motion for the components of the density matrix can now be written down from Eqs. 2.28 and 2.30:

$$\begin{aligned}
\dot{\rho}_{11} &= i \frac{E_0 \mu_{12}}{\hbar} (e^{-i\omega ct} \rho_{12} - e^{i\omega ct} \rho_{21}) + 2\gamma \rho_{22} \\
\dot{\rho}_{22} &= -i \frac{E_0 \mu_{12}}{\hbar} (e^{-i\omega ct} \rho_{12} - e^{i\omega ct} \rho_{21}) - 2\gamma \rho_{22} \\
\dot{\rho}_{12} &= i\omega_a \rho_{12} - i \frac{E_0 \mu_{12}}{\hbar} e^{i\omega ct} (\rho_{22} - \rho_{11}) - \gamma \rho_{12},
\end{aligned} \tag{2.31}$$

with $\rho_{21} = \rho_{12}^\dagger$ [65]. We see from this that, as expected, the dissipative process of atomic spontaneous emission causes a gradual relaxation into the ground state, with population being lost out of ρ_{22} at the rate $2\gamma\rho_{22}$. This process also causes decoherence that reduces the magnitude of ρ_{12} at the rate $|\gamma\rho_{12}|$.

We will analyze these results further and apply them to more specific experimental situations in the chapters to come. For now, we leave our Hamiltonians and master equations and turn our attention instead to the spectroscopic properties of atoms. The theoretical groundwork we have covered so far is hardly comprehensive, but it suffices as an introduction to the ideas and models that will be used throughout the remainder of this work.

Chapter 3

Xe Spectroscopy and Level Structure

3.1 Overview and Rationale for using Xe

Many experiments in atom optics make use of alkali atoms, including quite a few in our own group [66–69]. These atomic species are very useful because they have large dipole transition rates and resonances occurring conveniently within the near-infrared wavelength range. This has allowed the research community to develop sophisticated laboratory systems by building upon the commercially available lasers and optics available in this segment of the electromagnetic spectrum.

However, a room temperature vapor of alkali atoms would not be useful a nonlinear medium within a high-finesse cavity. In addition to interacting relatively strongly with near-infrared light fields these atoms are also very chemically active (Cs, for example, explodes on contact with water). When released into a vacuum chamber the gas atoms begin to react with exposed surfaces, and stick to them. This contamination tends to degrade the quality of exposed optical surfaces over time. Experiments passing light through an optical nanofiber roughly 1cm in length and immersed in Rb vapor showed a gradual reduction in transmission after only about 10 minutes of exposure. Heating the nanofiber during

exposure improved the transmission considerably, but losses were still typically greater than 50% [70]. This is certainly not an appropriate environment in which to place a pair of expensive, high-quality cavity mirrors. The alkali atoms would quickly destroy them.

One possible solution would be to place the warm alkali atoms within a vapor cell inside the cavity. In this case though reflection and scattering of light from the cell windows limit the cavity finesse to on the order of ~ 100 . The behavior of such a system can be described by the theory of classical optics (see, for example, Figure 2.6 (a) and the accompanying discussion). This system can be useful for observing nonlinear effects such as optical bistability, but quantum mechanical effects would not be noticeable [32, 33].

Noble gas atoms, on the other hand, are highly non-reactive and perfectly safe as an environment for sensitive optics. The relative difficulty in this case is that the energy difference between the ground and nearest excited states of noble gas atoms is very large. It would take a photon in the vacuum ultraviolet (VUV) band to excite one of these transitions, and equipment for emitting and manipulating VUV radiation is difficult to produce. To avoid this difficulty we decided to use xenon atoms in a long-lived metastable state. The choice of xenon over other noble gas atoms was motivated largely by practical considerations. Metastable xenon has a strong set of transitions in the near-IR, and the transition wavelengths are compatible with commercially available laboratory equipment. We will return to these pragmatic details later in Chapter 4 when we discuss methods of populating the metastable state. First though we need to understand some of the theory of the xenon energy level structure.

3.2 Xe's Electron Configuration

Any experimental work in atom optics requires some familiarity with the spectroscopy of the atomic species being used. Many experiments make use of alkali atoms, as has been pre-

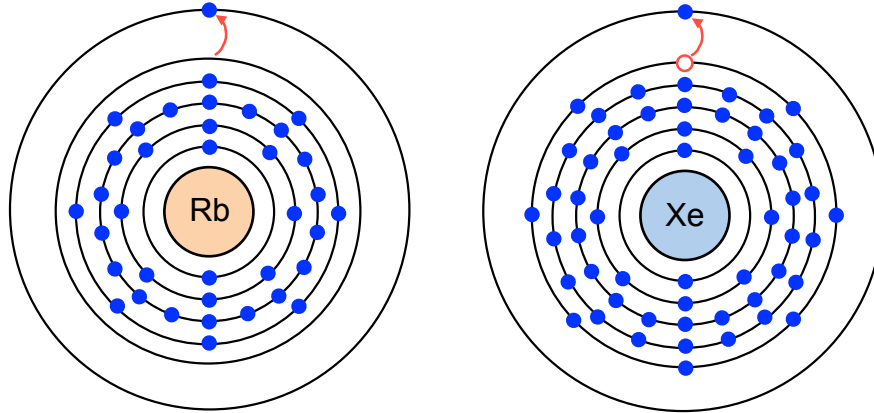


Figure 3.1: Illustration of the relationship between electronic excitations in Rb and in Xe. An electron excited from the valence band in Xe leaves behind a hole, illustrated here by an open red circle. This hole in the valence band couples with the excited electron through Coulomb forces and the spin-orbit interaction, leading to a complex energy level structure.

viously mentioned, and hence the spectroscopy of the alkali metals is relatively well-known in the field of quantum optics. The Ph.D. thesis of Daniel Jones from our group provides a helpful introduction to this topic [71]. We, however, need to know about the spectroscopy of xenon, which differs from that of the alkali metals in several critical respects. The relationship between electronic excitations in rubidium (an example alkali atom) and in xenon is illustrated in Figure 3.1.

In the electron configuration of a rubidium atom (or of any other alkali metal atom) there is only 1 valence electron. In the ground state this electron sits in a p orbital with orbital angular momentum quantum number $l = 1$. The excitation of a rubidium atom into a higher-lying energy state typically involves changes only in the state of this single valence electron. To a good approximation the atomic excited state can be described by the state of this electron only, and it is appropriate to label the states by referring to the electron's quantum numbers. These are the principal quantum number n , the orbital angular momentum quantum number l , and the total angular momentum quantum number (including the orbital and spin components) j [72].

The configuration of a xenon atom, on the other hand, contains a completely full $5p^6$ valence shell. When one of the valence electrons is excited into a higher-lying orbital it leaves behind a vacancy in the $5p$ shell. The vacancy has an additional set of degrees of freedom which communicate with the excited electron via the Coulomb and spin-orbit interactions. As a result the energy level structure is qualitatively different, and a different spectroscopic notation is used. If we hope to understand the potential of Xe as an intracavity nonlinear medium we need to understand this notation. We will begin by briefly reviewing some important results from the theory of the atomic spectra of multi-electron atoms.

3.3 Spectroscopy of Multi-Electron Atoms

3.3.1 The Hamiltonian

The problem of the calculation of energy eigenstates and eigenvalues of multi-electron atoms is an extremely difficult one. The Hamiltonian for such an atom is complicated by the fact that, in addition to the Coulomb field due to the atomic nucleus, each electron interacts with all other bound electrons as well. In general it is impossible or at least impractical to solve for the eigenstates of these systems exactly. To produce results that are both quantitatively accurate and conceptually helpful, one needs to adopt some approximations.

The largest contribution to the Hamiltonian for bound, excited electrons comes from the centrally-symmetric Coulomb potential produced by the nucleus and by all of the inner electrons in closed shells. This contribution is typically used as an “unperturbed” Hamiltonian for the system. Phenomena such as electrostatic interactions between unpaired electrons, relativistic effects, and magnetic interactions between the various angular momenta in the system are then accounted for using perturbation theory [73].

It is fairly common to begin with a Hamiltonian similar to

$$\hat{H} = \hat{H}_0 + \hat{H}_{es} + \hat{H}_{so} \quad (3.1)$$

$$\begin{aligned} \hat{H}_0 &= \sum_i \left(\frac{\hat{p}_i^2}{2m} + U(\hat{r}_i) \right) \\ \hat{H}_{es} &= \frac{1}{2} e^2 \sum_{i \neq k} \frac{1}{\hat{r}_{ik}} \\ \hat{H}_{so} &= \frac{\hbar^2}{2m^2 c^2} \sum_i \frac{1}{\hat{r}_i} \frac{\partial U(\hat{r}_i)}{\partial \hat{r}_i} \hat{l}_i \cdot \hat{s}_i, \end{aligned} \quad (3.2)$$

where $U(\hat{r}_i)$ is the centrally-symmetric potential, m the electron mass, e the electron charge, \hat{r}_i the position operator for electron i , and \hat{r}_{ik} the operator for the distance between electrons i and k . The operators \hat{l}_i and \hat{s}_i are the orbital and spin angular momentum operators for electron i , respectively. \hat{H}_0 is the unperturbed Hamiltonian, \hat{H}_{es} reflects the electrostatic contribution, and \hat{H}_{so} describes the spin-orbit interaction.

Note that Eq. 3.1 does not provide the complete Hamiltonian including all possible corrections. We have ignored for instance the relativistic correction to the electron kinetic energy, as well as the magnetic interactions between different electrons [73]. We will use the Hamiltonian of Eq. 3.1 only to illustrate the relationships between the various common forms of spectroscopic notation and their associated coupling schemes. For this purpose it will suffice. If one wishes to perform detailed calculations of exact atomic level energies, transition rates, etc., one should refer to the more complete discussion of refs. [72, 73].

Before moving on we would like to note that the magnetic interaction between the atomic nucleus and the outer electrons, called the hyperfine interaction, has also been neglected so far. It is very small compared to the spin-orbit and electrostatic terms of Eq. 3.1, but it will become important when we examine measurements of the xenon transmission spectrum in Section 3.5.5. We will consider the effects of the hyperfine interaction in that section.

3.3.2 Eigenstates

Now we consider the problem of finding and describing the energy eigenstates of an atomic system with a Hamiltonian like that of Eq. 3.1. In the idealized case of an atom with a purely centrally-symmetric Hamiltonian $\hat{H} = \hat{H}_0$, the energy of the system is completely determined by the values of the principal and orbital angular momentum quantum numbers n and l for each electron. For every l though there exist $(2l + 1)$ possible values of m_l , the quantum number for the projection of orbital angular momentum onto the z -axis. Additionally, for each m_l there are two possible values for the z -projection of the electron's spin, with quantum numbers $m_s = \pm \frac{1}{2}$. Consequently, in this model each energy level has a $2(2l + 1)$ -fold degeneracy. Application of perturbative corrections such as those of Eq. 3.1 lifts this degeneracy, splitting each energy level n, l into as many as $2(2l + 1)$ separate sublevels.

For an electron state with definite n, l, m_l , and m_s we write $|n, l, m_l, m_s\rangle \equiv |n, l\rangle |m_l, m_s\rangle$. Whatever the perturbing Hamiltonian, the eigenstate corresponding to each sublevel of the level n, l will consist of some superposition of the various $|m_l, m_s\rangle$ states. For the purpose of conveniently labeling these states it is helpful to assign a unique set of quantum numbers to each one, but it may not always be easy to see how these numbers can be assigned systematically and in a sensible way. As a silly example, one could try to imagine a reasonable system for labeling the states

$$\begin{aligned}
 |\psi_1\rangle &= \left(-.4179 \left| 1, \frac{1}{2} \right\rangle + .7071 \left| 0, \frac{1}{2} \right\rangle - .2319 \left| -1, -\frac{1}{2} \right\rangle + -.5211 \left| 1, -\frac{1}{2} \right\rangle \right) \\
 |\psi_2\rangle &= \left(.7530 \left| 1, \frac{1}{2} \right\rangle + .1032 \left| -1, -\frac{1}{2} \right\rangle - .6498 \left| 1, -\frac{1}{2} \right\rangle \right) \\
 |\psi_3\rangle &= \left(-.4179 \left| 1, \frac{1}{2} \right\rangle - .7071 \left| 0, \frac{1}{2} \right\rangle - .2319 \left| -1, -\frac{1}{2} \right\rangle - .5211 \left| 1, -\frac{1}{2} \right\rangle \right) \\
 |\psi_4\rangle &= \left(-.2892 \left| 1, \frac{1}{2} \right\rangle + .9390 \left| -1, -\frac{1}{2} \right\rangle - .1860 \left| 1, -\frac{1}{2} \right\rangle \right),
 \end{aligned}$$

where the ket $|i, j\rangle$ indicates a state with $m_l = i$ and $m_s = j$. Aside from simply assigning each of them a randomly-chosen number 1 through 4, which is not very informative, it is difficult to see how this should be done. Fortunately in most real-world cases atomic energy eigenstates turn out to be at least approximately equal to the eigenstates of some specific set of angular momentum operators. This provides an appropriate, if only approximate, system for labelling the states. The set of operators that is most appropriate varies however from one atomic species to another. It often varies among the levels of a single atomic species as well, depending on the degree of excitation [72, 73].

The correct set of operators and associated quantum numbers is typically determined through the use of coupling schemes that describe the relationships between the sizes of the various perturbative corrections to the Hamiltonian Eq. 3.1. The key to understanding the spectroscopic coupling schemes is to recognize that they exist primarily for purposes of classification. Specifying relationships between the sizes of the various corrections allows one to infer a set of quantum numbers that come close to describing the actual eigenstates of the system. Thus the goal of a coupling scheme is not necessarily the calculation of exact eigenstates, but the development of a reasonable and relatively systematic nomenclature for referring to the states. Any scientist working in atomic and optical physics will benefit from a basic understanding of the principles behind this nomenclature. For the sake of background, then, we will briefly review the two most well-known coupling schemes, then move on to describe the unique case of Xe and the other noble gases.

3.3.3 LS-Coupling

The first coupling scheme we will consider is called the LS-coupling approximation or the Russell-Saunders approximation. In many cases the Coulomb interaction between outer electrons is much stronger than the spin-orbit interaction. Typically this results when the average distance between the excited electron and its nearest neighbors is relatively small,

as is often the case with the lighter elements. In this approximation the perturbation of Eq. 3.1 is applied in two steps. First the eigenstates and level energies are calculated by treating the electrostatic term \hat{H}_{es} as a perturbation on top of \hat{H}_0 , and neglecting the spin-orbit term \hat{H}_{so} . Then a second round of perturbative calculations is performed on these results to include small corrections due to the spin-orbit term. Clearly this approximation is valid only when the terms in the Hamiltonian obey $|\hat{H}_0| \gg |\hat{H}_{es}| \gg |\hat{H}_{so}|$.

In the first step the states and level energies are calculated for $\hat{H}_0 + \hat{H}_{es}$ using perturbation theory. We note that the Hamiltonian for the electrostatic interaction can be written in terms of the operators $\hat{\mathbf{l}}_i \cdot \hat{\mathbf{l}}_k$ and $\hat{\mathbf{s}}_i \cdot \hat{\mathbf{s}}_k$ for two electrons i and k , where $\hat{\mathbf{s}}_i$ and $\hat{\mathbf{l}}_i$ are the vector spin and orbital angular momentum operators for electron i [73]. From this fact it is straightforward to show that the Hamiltonian aside from the spin-orbit term commutes with the total orbital and spin angular momentum operators $\hat{\mathbf{L}} = (\hat{\mathbf{l}}_1 + \hat{\mathbf{l}}_2 + \dots)$ and $\hat{\mathbf{S}} = (\hat{\mathbf{s}}_1 + \hat{\mathbf{s}}_2 + \dots)$. So for this first step all levels with the same quantum numbers L and S are degenerate in energy. Levels with differing L and S will have different energies. The dependence of energy on L can be understood roughly speaking by noticing that the value of L determines the relative orientations of the electron orbitals. The relative orientation influences the average distance between electrons, which in turn decides the effective Coulomb potential energy for the state. The dependence of energy on S results from the so-called exchange interaction. The exchange interaction takes into account the fact that the overall wavefunction of an atom must be antisymmetric upon the exchange of any two electrons, and it leads to energy splittings that depend on the relationships between electron spins. In this coupling scheme a group of levels with a given L and S are commonly called a “term”.

After the splittings between various terms have been calculated in this first step, another step of perturbation theory is applied to include the comparatively small effects of spin-orbit coupling. The relative orientations of spin and orbital angular momenta determine the energy corrections that account for this interaction. This relative orientation is

largely determined by the total angular momentum, with operator $\hat{\mathbf{J}} = \hat{\mathbf{L}} + \hat{\mathbf{S}}$ and corresponding quantum number J . As a result each term LS is split into a number of levels equal to the number of allowed values of J . This number is given by the rules for the addition of angular momenta: $L + S \geq J \geq |L - S|$. As long as the atom under consideration is isolated with no preferred orientation, each level given by LSJ retains a degeneracy equal to the number of allowed values of m_J , the quantum number for the z-component of the total angular momentum. If the rotational symmetry were to be broken, for instance by application of an external magnetic field, each level LSJ would be further split into $(2J + 1)$ sublevels with energies determined by m_J .

Atomic states in the LS coupling scheme are usually labeled using the notation $^{(2S+1)}L_J$. The number $(2S + 1)$ is called the ‘‘multiplicity’’ of the state. In the case $L \geq S$ the multiplicity is equal to the degeneracy of the level. The quantum number L is written using common spectroscopic notation that has been adopted for historical reasons: $L = 0$ is indicated by the letter ‘S,’ $L = 1$ with the letter ‘P,’ etc., as detailed in Table 3.1. For example, a state with $L = 1$, $S = +\frac{1}{2}$, and $J = \frac{3}{2}$ would be labeled $^2P_{3/2}$. If the state happens to have odd parity, this will often be indicated with a superscript ‘o’ as in $^2P_{3/2}^o$. Absence of the ‘o’ implies even parity. The symbol $^{(2S+1)}L$ is called the term symbol for the LS coupling scheme. In combination with the electron configuration, the term symbol and the value of J are sufficient to specify an atomic energy level with LS coupling [72, 73].

Table 3.1: Spectroscopic notation for the orbital angular momentum quantum number L .

L =	0	1	2	3	4	5	...
notation:	S	P	D	F	G	H	...

The LS coupling scheme produces a very clean description and concise notation for atomic excited states, but the approximations involved are not always valid. Particularly, as the atomic number of an atom increases the typical distance between the excited electron

and core electrons increases as well. When this distance becomes large the approximation of the LS-coupling scheme breaks down and a more appropriate means of describing the atomic states must be found.

3.3.4 jj-Coupling

The LS coupling scheme is a good choice when electrostatic forces overpower the spin-orbit interaction. It is sensible to assume that a similar approximation should be possible in the opposite extreme, where the spin-orbit interaction dominates. In this extreme the jj coupling scheme provides an appropriate description of atomic spectra.

As was previously discussed, using the Hamiltonian $\hat{H} = \hat{H}_0$ the energy of an atomic level depends only on the principal and orbital angular momentum quantum numbers n and l for bound electrons, leading to a $2(2l + 1)$ -fold degeneracy for each level. As before, small corrections such as the \hat{H}_{es} and \hat{H}_{so} of Eq. 3.2 are included by applying successive rounds of perturbation theory. This time though the perturbative effects of the two terms are calculated in the reverse order. The jj-coupling approximation is valid when $|\hat{H}_0| \gg |\hat{H}_{so}| \gg |\hat{H}_{es}|$.

Calculation begins with the inclusion of the spin-orbit interaction. This leads to an energy term that depends primarily on the relative orientation of an electron's spin and orbital angular momentum. For a given l_i , this relationship is determined by the value of j_i for electron i . For a single electron of course we can have either $j_i = l_i + \frac{1}{2}$ or $j_i = l_i - \frac{1}{2}$ (unless $l_i = 0$, in which case we must have $j_i = \frac{1}{2}$). After the first round of perturbation calculations the energy of an atomic level is specified by the values of n , l , and j for each electron, and each level possesses a $\sum_i (2j_i + 1)$ -fold degeneracy.

When the second stage of perturbations is applied to include effects of electrostatic interactions, the levels determined by $n_i l_i j_i$ for each electron are further split based on the total angular momentum J of all electrons together. The energy of each level is then deter-

mined by the values $n_i l_i j_i$ for each electron, and the value of J . States with two contributing electrons are written as $(j_1 j_2)_J$, where the $(j_1 j_2)$ symbol is the term symbol used with the jj coupling scheme. Terms with more than 2 contributing electrons require additional quantum numbers to completely describe the state. As in the case of LS coupling the electron configuration, term symbol, and value of J taken together describe an atomic energy level [72, 73].

The LS and the jj coupling schemes are idealizations. No real atomic spectrum exactly fits either of these descriptions. They do however provide a plausible basis for describing and labeling the real atomic states. Still, there are some intermediate cases in which neither the LS or the jj coupling description is appropriate. The noble gases, including xenon, belong to this category. They require a separate coupling system.

3.3.5 jl-Coupling

For the excited states of xenon and the other noble gases the excited electron is on average very far from the other electrons. Electrons in the atomic core, on the other hand, are relatively close together. As a result electrostatic forces between these core electrons can be quite strong. The spin-orbit interaction between the core electrons is typically weaker, similar to the case of LS coupling. Both of these interactions are considerably stronger than the electrostatic interaction between the core and the excited electron, as this electron is rather far away. The spin-orbit interaction of the excited electron is then weakest of all. These relationships constitute an intermediate regime between LS- and jj-coupling, neither of which will work, so a new coupling scheme is needed. This new system is called jl-coupling or jK-coupling [74].

We can state the conditions for the validity of this scheme in equation form, but for this we must rewrite Eqs 3.1 and 3.2. The contributions \hat{H}_{es} and \hat{H}_{so} must be split into two sets of terms: those referring to the excited electron and those referring to the core

electrons. Additionally, for the jl-coupling scheme the electrostatic term must be further separated into two parts, one caused purely by coulomb repulsion and another due to the exchange interaction. The mathematical details are not relevant to our discussion, so we will skip past them and simply refer to the Coulomb and exchange parts of the electrostatic terms using the notation $[\hat{H}_{es}]_C$ and $[\hat{H}_{es}]_E$, respectively. We have

$$\hat{H} = \hat{H}_0 + \hat{H}_{es}^{core} + \hat{H}_{es}^{exc} + \hat{H}_{so}^{core} + \hat{H}_{so}^{exc} \quad (3.3)$$

$$\begin{aligned} \hat{H}_{es}^{core} &= \frac{1}{2}e^2 \sum_{i,k>i}^{core} \frac{1}{\hat{r}_{ik}}, & \hat{H}_{es}^{exc} &= \frac{1}{2}e^2 \sum_i^{core} \frac{1}{\hat{r}_{ij}} \\ \hat{H}_{so}^{core} &= \frac{\hbar^2}{2m^2c^2} \sum_i^{core} \frac{1}{\hat{r}_i} \frac{\partial U(\hat{r}_i)}{\partial \hat{r}_i} \hat{\mathbf{l}}_i \cdot \hat{\mathbf{s}}_i, & \hat{H}_{so}^{exc} &= \frac{\hbar^2}{2m^2c^2} \frac{1}{\hat{r}_j} \frac{\partial U(\hat{r}_j)}{\partial \hat{r}_j} \hat{\mathbf{l}}_j \cdot \hat{\mathbf{s}}_j, \end{aligned} \quad (3.4)$$

where the index j refers to the excited electron. The condition for the validity of the jl coupling scheme is

$$|\hat{H}_0| \gg |\hat{H}_{es}^{core}| \gg |\hat{H}_{so}^{core}| \gg |[\hat{H}_{es}^{exc}]_C| \gg |\hat{H}_{so}^{exc} + [\hat{H}_{es}^{exc}]_E|.$$

This condition is typically (and quite surprisingly) satisfied for excited states of noble gas atoms [73, 74].

A calculation using the approximation of jl-coupling proceeds as follows. Beginning with \hat{H}_0 , one includes \hat{H}_{es}^{core} as a perturbation. The energy of the resulting system is determined by the electron configuration along with the values of L_1 and S_1 , the quantum numbers for the total orbital and spin angular momenta of the atomic core. Next \hat{H}_{so}^{core} is included, and these levels split depending on the value of J_1 , the total angular momentum of the core. The coupling of $[\hat{H}_{es}^{exc}]_C$ is incorporated next, and splits each of these levels depending on the orientation of the total core angular momentum relative to the orbital angular momentum of the excited electron. This relationship is described by K , the quantum number for the operator $\hat{\mathbf{K}} = \hat{\mathbf{L}}_1 + \hat{\mathbf{S}}_1 + \hat{\mathbf{l}}$, where $\hat{\mathbf{l}}$ is the orbital angular momentum operator

for the excited electron. Finally, the inclusion of $\hat{H}_{so}^{exc} + [\hat{H}_{es}^{exc}]_E$ leads to a further splitting depending on the relative orientations of $\hat{\mathbf{K}}$ and the excited electron's spin \hat{s} . The value of this last energy splitting is determined by J , the quantum number for $\hat{\mathbf{J}} = \hat{\mathbf{L}}_1 + \hat{\mathbf{S}}_1 + \hat{\mathbf{l}} + \hat{s}$. Table 3.2 provides a concise summary of the notation used with jl-coupling. This is the notation commonly used to describe excited states of the noble gas atoms [72, 73].

Table 3.2: Summary of the spectroscopic notation used with the jl-coupling scheme.

Notation	Meaning
$^{2S_1+1} (L_1)_{J_1}, l[K]_J =$	description of an atomic level using jl-coupling
$S_1 =$	spin angular momentum quantum number for atomic core
$L_1 =$	orbital angular momentum quantum number for atomic core
$J_1 =$	total angular momentum quantum number for atomic core
$l =$	orbital angular momentum quantum number for excited electron
$K =$	quantum number for $\hat{\mathbf{K}} = \hat{\mathbf{L}}_1 + \hat{\mathbf{S}}_1 + \hat{\mathbf{l}}$
$J =$	total angular momentum quantum number for all electrons

These coupling schemes might seem somewhat convoluted, and at times counterintuitive. It may at first appear odd, for instance, that the inclusion of the spin-orbit interaction in the jl coupling scheme leads to a coupling of the electron spin \hat{s} with $\hat{\mathbf{K}}$. After all, the spin-orbit term \hat{H}_{so}^{exc} as given in Eq. 3.4 indicates a coupling only between \hat{s} and $\hat{\mathbf{l}}$, whereas $\hat{\mathbf{K}}$ includes the angular momenta of the inner core electrons as well. (The contribution from $[\hat{H}_{es}^{exc}]_E$ couples \hat{s} with $\hat{\mathbf{S}}_1$, but still one might not naively expect to develop any relationship between \hat{s} and $\hat{\mathbf{L}}_1$ through this term.) We must remember though that special rules apply in the quantum-mechanical addition of angular momenta. In the jl coupling scheme $\hat{\mathbf{l}}$ is coupled to $\hat{\mathbf{L}}_1 + \hat{\mathbf{S}}_1$ through the relatively strong term $[\hat{H}_{es}^{exc}]_C$. Thus the state of the system before inclusion of spin-orbit coupling is a complicated superpositions of states of various m_l , m_{S_1} , and m_{L_1} . Strictly speaking the addition of \hat{s} with $\hat{\mathbf{l}}$ would interfere with this superposition state, and since the term $[\hat{H}_{es}^{exc}]_C$ is assumed to be much stronger than

$\hat{H}_{so}^{exc} + [\hat{H}_{es}^{exc}]_E$ in j1-coupling, this is not allowed to happen. As a result, poor helpless \hat{s} is forced to couple with the only other angular momentum still left uncoupled, and this just happens to be \hat{K} . Beggars can't be choosers.

3.4 Energy Level Structure of Xenon

In general, the complete description of an energy level in the j1-coupling scheme requires the specification of the electron configuration along with the complete set of quantum numbers $^{2S_1+1}(L_1)_{J_1}, l[K]_J$. In practice, however, transitions between levels typically involve changes to the state of only the excited electron. As a result the level structure of a noble gas atom can be divided into manifolds, with each manifold defined by the state of the atom's core electrons. This core state is described by the quantum numbers $^{2S_1+1}(L_1)_{J_1}$. In a noble gas atom with only 1 excited electron the core has quantum numbers $L_1 = 1$ and $S_1 = \frac{1}{2}$, so there are only two possible states for the core electrons: $^2P_{1/2}^\circ$ and $^2P_{3/2}^\circ$. Rather than writing this term in its entirety for each excited state it is common to write only the state of the excited electron $n l[K]_J$, where n is the excited electron's principle quantum number. A prime is then used to indicate that the core is in state $^2P_{1/2}^\circ$, otherwise it is assumed that the core state is $^2P_{3/2}^\circ$. This greatly simplifies the notation. Hence the notation $6s[3/2]_2^\circ$ indicates an excited state within the $^2P_{3/2}^\circ$ manifold, whereas $6s'[1/2]_1^\circ$ is a member of the manifold $^2P_{1/2}^\circ$.

Xenon has a rich level structure, but we will confine our discussion here to the levels relevant for the experiments we describe in Chapters 4 through 6. Figure 3.2 illustrates the energy levels of Xe that we will use, along with the dipole-allowed transitions amongst them. It is fairly easy to find commercially available lasers and optics to work within the wavelength range 700~950 nm, so transitions in this range are very convenient to work

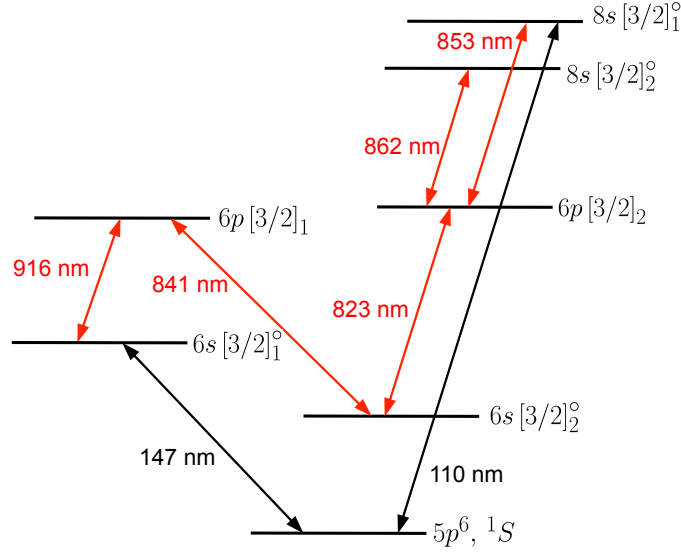


Figure 3.2: Illustration of the excited energy levels of neutral xenon used in this work. Relevant dipole-allowed transitions and their associated wavelengths are indicated with colored arrows. Transitions with wavelengths in the near infrared are shown with red arrows, and those with wavelengths in the ultraviolet with black arrows. Ultraviolet radiation is produced by transitions to the ground state $5p^6, ^1S$, which lies much lower in energy than any of the excited states. Distances between energy levels are not drawn to scale.

with in an optics laboratory. Notice however that the wavelengths of all transitions to/from the ground state of xenon fall within the vacuum ultraviolet region of the electromagnetic spectrum. There are not many sources and optical components available that work at these wavelengths, so these transitions are by comparison very difficult to probe and control. (Indeed, the vacuum ultraviolet region is so named because radiation of this kind cannot propagate in air even over a very short distance. As an example, the rate of attenuation of a 147 nm UV wave traveling through air is roughly 30% per micron! [75]) As a result practical laboratory experiments are not possible using xenon atoms in their ground state.

Fortunately the lowest-lying excited state $6s[3/2]_2^o$ is metastable, meaning that single-photon transitions between this state and the ground state are forbidden. The metastable state has $J = 2$ while the ground state has $J = 0$. A single photon carries only 1 quantum of angular momentum, so a single-photon transition between these two states would violate conservation of angular momentum. As a result this excited state has an ex-

tremely long radiative lifetime of roughly 43 seconds [76]. The timescale for decay from this state is so much longer than all other timescales in a typical experiment (usually on the order of 10's to 100's of ns) that the decay process can usually be neglected. Hence the $6s[3/2]_2$ state acts like an effective ground state of the xenon atom. Once it is populated, transitions to the adjacent levels shown in Figure 3.2 can be probed and manipulated for a variety of experiments.

Before moving on to our experimental methods and results, it will be helpful to note some of the practical characteristics of atomic transition lines in general and those of xenon in particular. An atomic transition line between two energy levels is characterized by 3 parameters: the energy difference between levels, the rate at which the transition occurs, and the probability for a given atom in the excited state to make this particular transition. The energy differences for the transitions of interest to us can be inferred from the wavelengths shown in Figure 3.2 using the relations $\nu = c/\lambda$ and $\Delta E = h\nu$, where λ is the wavelength of radiation associated with the transition and ν is the radiation frequency.

The rates of atomic transitions can typically be found in the published literature or in the NIST Atomic Spectra Database [77, 78]. The rates can also be calculated a priori from theoretical principles, though these calculations are in general quite laborious. The results depend on matrix elements of the dipole operator between the relevant atomic states. Since most of the time these states themselves are known only approximately (see the discussion of section 3.3 above), producing accurate results can be difficult.

The probability for an excited atom to make a given transition is determined by the branching ratio for that transition. For a transition from a higher state $|i\rangle$ to a lower state $|j\rangle$ the branching ratio is given by $BR = \Gamma_{ij}/\Gamma_i$, where Γ_{ij} is the rate for the transition $|i\rangle$ to $|j\rangle$ and Γ_i is the combined rate for all decays from state $|i\rangle$. The total decay rate is given by $\Gamma_i = \sum_j \Gamma_{ij}$, where the sum is taken over all of the possible final states. It can also be found using $\Gamma_i = \tau_i^{-1}$, where τ_i is the radiation-limited lifetime of state $|i\rangle$.

The wavelengths, transition rates, and branching ratios for some of the transitions shown in Figure 3.2 are given in Table 3.3 below.

Table 3.3: Transition rates, wavelengths λ , and frequencies ν for xenon transitions relevant to this work [77–80]. Much of the data given in [78] is qualitative in nature and may not necessarily be quantitatively accurate. The transition rates and branching ratios below are derived in part from this data, and should be treated as educated guesses rather than exact values. Wavelengths given are those measured in air, except for the 110 nm VUV transition, which was measured in vacuum.

Transition	λ (nm)	ν (THz)	Rate (MHz)	Branching Ratio
$8s[3/2]_1^{\circ} \rightarrow 6p[3/2]_2$	853.010	351.356	0.72	$\sim 2/39$
$8s[3/2]_1^{\circ} \rightarrow 5p^6, ^1S$	109.972	2726.08	43*	~ 1
$8s[3/2]_2^{\circ} \rightarrow 6p[3/2]_2$	862.424	347.520	1.5	3/25
$6p[3/2]_2 \rightarrow 6s[3/2]_2^{\circ}$	823.163	364.095	29	10/11
$6p[3/2]_1 \rightarrow 6s[3/2]_2^{\circ}$	840.919	356.408	1.0	4/5
$6p[3/2]_1 \rightarrow 6s[3/2]_1^{\circ}$	916.265	327.100	.25	1/5

* Note that there is a discrepancy in the published data between the measured lifetime of the $8s[3/2]_1$ state and its rate of decay into the ground state $5p^6, ^1S$.

3.5 Spectral Line Shapes and Broadening Mechanisms

3.5.1 Fundamental Theory

It is one thing to state the energy levels, resonance frequencies, transition rates, etc., for a given atomic species, and quite another thing to measure them. We will now begin to round out the theoretical considerations of the preceding sections into an experimentally robust picture of the behavior of xenon atoms and their excited states as they interact with radiation. For this we begin by revisiting Eq. 2.31, which gives us the master equation describing the interaction between a 2-level atom and a classical light field. We assume for

now that our system consists of a large number of identical, non-interacting atoms. We will first calculate the density matrix for one atom and then extrapolate to find the behavior of the ensemble. It is convenient to make the substitutions

$$\sigma_{11} = \rho_{11}, \quad \sigma_{22} = \rho_{22}, \quad \sigma_{21} = \rho_{21}e^{i\omega_p t}. \quad (3.5)$$

where ω_p , is the angular frequency of the probe field. Then using the fact $\sigma_{11} + \sigma_{22} = 1$, Eq. 2.31 can be rewritten:

$$\begin{aligned} \dot{\sigma}_{22} - \dot{\sigma}_{11} &= -i\frac{2E_0\mu_{12}}{\hbar} (\sigma_{12} - \sigma_{12}^*) - 2\gamma(\sigma_{22} - \sigma_{11} + 1) \\ \dot{\sigma}_{21} &= i\Delta\sigma_{21} + i\frac{E_0\mu_{12}}{\hbar} (\sigma_{22} - \sigma_{11}) - \gamma\sigma_{21}, \end{aligned} \quad (3.6)$$

where $\Delta \equiv \omega_p - \omega_a$, and ω_a is the angular frequency of the atomic transition.

The evolution of a system under the equations 3.6 possesses two distinct time scales. In the instant after the driving field has been turned on, the atom begins to respond in a complicated way that may be difficult to calculate analytically. However after some time this transient response dies away, and the system is left in a steady state. The length of time required to reach the steady state goes as the inverse of the decoherence rate for the system. In our case the requirement for the system to be in the steady state is $t \gg 1/\gamma$, and in our work $1/\gamma$ is typically on the order of 50 ns. We assume for now that the laser field interacting with the atom has been on much longer than 50 nanoseconds, and we neglect the transient part of the dynamics. The solution to Eq. 3.6 in the steady state is

$$\begin{aligned} \sigma_{22} - \sigma_{11} &= -\frac{\Delta^2 + \gamma^2}{\Delta^2 + \gamma^2 + 2\Omega^2} \\ \sigma_{21} &= \frac{\Omega(\Delta - i\gamma)}{\Delta^2 + \gamma^2 + 2\Omega^2}, \end{aligned} \quad (3.7)$$

using $\Omega \equiv E_0\mu_{12}/\hbar$ [65]. For the remainder of this chapter we will assume that the driving field is weak, in which case the terms Ω^2 can be neglected.

Now that we know the density matrix for a single atom we can calculate the rate at which the atoms absorb incoming radiation. Absorption is governed by the imaginary part of the susceptibility χ . The susceptibility in turn can be found using the relation

$$P(t) = \epsilon_0 \chi E(t) \quad (3.8)$$

where $P(t)$ is the complex atomic polarization density and $E(t)$ is the complex classical electric field. The polarization density can be found by taking the expectation value of the dipole operator,

$$P_{real}(t) \equiv P(t) + P^*(t) = N \langle \hat{\mu} \rangle = N \text{Tr}[\hat{\rho} \hat{\mu}], \quad (3.9)$$

where N is the number of atoms per unit volume interacting with the light field. This leads to

$$\chi = \frac{N \mu_{12}}{\hbar \epsilon_0 E(t)} \rho_{21} = \frac{N \mu_{12}}{\hbar \epsilon_0 E_0} \sigma_{21} = N \frac{\mu_{12}^2 (\Delta - i\gamma)}{\hbar \epsilon_0 (\Delta^2 + \gamma^2)} \quad (3.10)$$

An optical field of frequency ω_p traveling through the gas will be attenuated according to the relation

$$I(L) = I_0 e^{-OD_h} \quad (3.11)$$

$$OD_h \equiv -2 \frac{\omega_p}{c} \text{Im}[n] \cdot L \approx -\frac{\omega_p}{c} \text{Im}[\chi] \cdot L,$$

where OD_h is the optical depth of the gas, $n = \sqrt{1 + \chi}$ is the complex index of refraction for the gas, and c the speed of light in vacuum. I_0 the field intensity before entering the gas and $I(L)$ the intensity after traveling through the gas a distance L . Figure 3.3 shows a plot of the transmission vs. frequency for an 823 nm laser field tuned near the $6s[3/2]_2$ to $6p[3/2]_2$ xenon transition and passing through a gas of metastable xenon. The model parameters were chosen to correspond roughly to the propagation losses after passing through a vacuum chamber 5 cm in length, filled with metastable Xe atoms to a density of 10^9 1/cm³. This

absorption profile is commonly called a Lorentzian line. For this lineshape, in the limit of large $|\Delta|$ the optical depth decreases proportionately with $\frac{1}{\Delta^2}$.

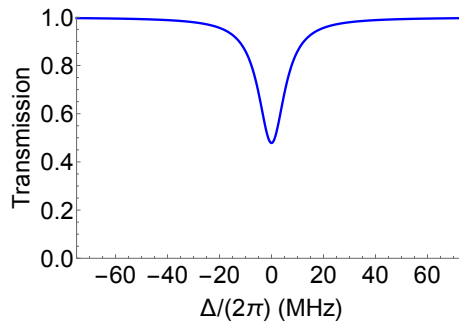


Figure 3.3: Calculated absorption spectrum for a gas of identical metastable xenon atoms. In the limit of large $|\Delta|$ the absorption rate falls off as $\frac{1}{\Delta^2}$.

3.5.2 Homogeneous Broadening

We have just calculated the transmission spectrum expected from a gas of identical, non-interacting metastable xenon atoms. In this case the intrinsic spontaneous decay rate of excited atoms determines the width and shape of the absorption line. Spontaneous decay is referred to as a “homogeneous broadening” mechanism. The fundamental feature of a homogeneous broadening mechanism is that it effects all atoms or other quantum emitters of a particular species in essentially the same way. The absorption spectrum of an ensemble of quantum emitters is referred to as “homogeneously broadened” if the shapes of the absorption lines are determined primarily by homogeneous mechanisms. The Lorentzian functional form of the optical depth given in Eq. 3.11 is a common characteristic of homogeneously-broadened systems.

There are other possible sources of homogeneous broadening in addition to spontaneous decay. These include for example collisions between atoms or between an atom and a container wall, or the shortness of transit times as atoms fly at high speed through a small optical mode volume [81]. These mechanisms cause absorption lines to become broader and shallower (hence the term “broadening”) because they reduce the effective interaction

time allowed for the coherent evolution of the atomic system. For the experiments that we will describe in this work spontaneous decay will be the dominant homogenous broadening mechanism, so we will neglect all other sources of homogeneous broadening.

3.5.3 Inhomogeneous Broadening

The derivation of Section 3.5.1 assumed that all metastable xenon atoms involved in the interaction were identical. In a typical laboratory environment though this will not be true. Most importantly, atoms in a room-temperature gas are always moving, each one with a random speed and direction.

The velocities of independent gas atoms can each be divided into independent x-, y-, and z-components, each of which constitutes an independent degree of freedom. The distributions of the velocities in the x, y, and z directions obey Maxwell-Boltzmann statistics. Modern lasers and detections systems are sophisticated enough that in this situation the Doppler effect needs to be taken into account. From the perspective of an inertial observer sitting in a lab, the Doppler effect causes the resonant energies of emitting and absorbing atoms to shift depending on their velocities. If we choose our coordinates to have the z-axis aligned with the optic axis of our measurement system, this shift is given by

$$\delta\omega_a \equiv \omega_a - \omega_{a,0} = \beta\omega_{a,0}, \quad (3.12)$$

where $\beta = v_z/c$ and v_z is the z-component of the velocity of the atom in question. The angular frequency of the atomic transition is ω_a , and $\omega_{a,0}$ is the angular frequency of the transition for an atom with $v_z = 0$. Eq. 3.12 is valid to first order in β .

The z-components of the atomic velocities follow Boltzmann statistics, i.e.

$$P(v_z) = \frac{e^{-mv_z^2/(2k_B T)}}{Z}, \quad (3.13)$$

where $P(v_z) dv_z$ is the probability for an atom to have the z-component of its velocity between v_z and $v_z + dv_z$. We have used k_B for Boltzmann's constant, T for the temperature in Kelvins, and m for the mass of a xenon atom. (Naturally-occurring xenon contains several isotopes, each of which has a slightly different mass, but the difference is small enough that we can neglect it here.). Z is the partition function given by $Z = \int_{-\infty}^{\infty} dv_z e^{-mv_z^2/(2k_B T)} = \sqrt{\frac{m}{2\pi k_B T}}$. Since $v_z = \frac{c}{\omega_a} \delta\omega_a$, the Gaussian statistical distribution of atomic velocities leads directly to a Gaussian distribution of transition frequencies:

$$P(\delta\omega_a) = \frac{c}{\omega_a} \sqrt{\frac{m}{2\pi k_B T}} \cdot e^{-\frac{mc^2 \delta\omega_a^2}{2\omega_a^2 k_B T}}. \quad (3.14)$$

For xenon atoms $m = 2.18 \cdot 10^{-25}$ kg, and at room temperature the standard deviation of the above distribution is $\sigma_{\delta\omega_a} = \frac{\omega_a}{c} \sqrt{\frac{k_B T}{m}} = 2\pi \cdot 167$ MHz.

The transition frequencies in our inhomogeneously-broadened, room-temperature gas of xenon atoms are spread across a Gaussian distribution with a standard deviation of 167 MHz, centered on the frequency $\omega_a = 2\pi \cdot 364.095$ THz. As a result, we cannot expect measured transmission spectra to look like the one calculated in the previous section and shown in Figure 3.3. The width of the inhomogeneous distribution (~ 340 MHz) is much larger than the homogeneous linewidth (~ 20 MHz, as seen from Figure 3.3). Since the inhomogeneous broadening mechanism dominates, it is a reasonable approximation to describe the absorption line of our room-temperature xenon atoms using the Gaussian profile of Eq. 3.14. The optical depth will be proportional to $P(\delta\omega_a)$, and the proportionality constant can be determined from the condition that the integrated optical depths for the homogeneous and inhomogeneous absorption profiles must be equal. I.e.,

$$\int_{-\infty}^{\infty} OD_{ih} d\Delta = \int_{-\infty}^{\infty} OD_h d\Delta, \quad (3.15)$$

where OD_{ih} is the optical depth including only inhomogeneous broadening, and OD_h is optical depth when including only homogeneous broadening as given in Eq. 3.11. This

leads to

$$OD_{ih} = \sqrt{\frac{\pi}{2}} \frac{NL\omega_a\mu_{12}^2}{c\hbar\epsilon_0\sigma} \cdot e^{-\frac{\Delta^2}{2\sigma^2}}. \quad (3.16)$$

3.5.4 The Voigt Lineshape

Eq. 3.16 is accurate enough for most of our purposes, but a rigorous calculation of the lineshape must include homogeneous and inhomogeneous broadening mechanisms simultaneously. The correct procedure for this is to convolve the Lorentzian optical depth function of Eq. 3.11 with the Gaussian distribution of Eq. 3.14. The result is called a Voigt lineshape or Voigt profile. It is very frequently used in the description of atomic spectra. The convolution cannot be carried out analytically without the use of advanced functions [82]. Fortunately, many computer algebra systems contain easy-to-use implementations of the Voigt profile. One need only know the linewidths of the constituent Lorentzian and Gaussian contributions. In our case these linewidths are given by γ and σ , respectively.

Figure 3.4 shows the theoretical transmission spectrum of a room-temperature gas of xenon atoms. The dashed red curves show the Gaussian profile derived by considering only the inhomogeneous contributions to the broadening, and the solid blue curve shows the Voigt profile which includes both homogeneous and inhomogeneous broadening mechanisms. For reference the dotted green curve shows the expected absorption from an equal number of atoms when the Doppler effect is neglected, using Eq. 3.11. The parameters used are the same as those used to produce Figure 3.3, but that the density of metastable atoms was increased to $3 \cdot 10^{10}$ 1/cm³. The inclusion of Doppler broadening considerably widens the transmission dip and reduces its depth proportionately, so this increase in the density of atoms was necessary to produce a spectrum with noticeable absorption.

The Voigt and Gaussian profiles are nearly identical for small $|\Delta|$. As $|\Delta|$ increases though the exponential profile of the Gaussian function causes it to decay much more quickly than the Voigt profile, as is evident in Figure 3.4 (b). Hence the inhomoge-

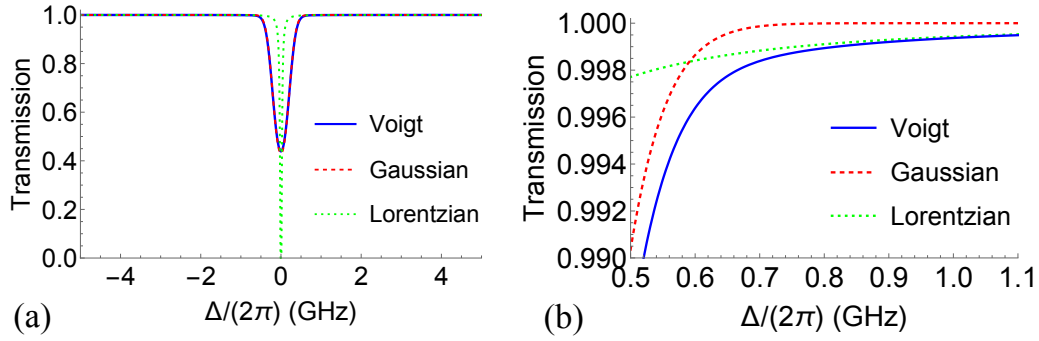


Figure 3.4: Calculated absorption spectrum for a gas of room-temperature metastable xenon atoms, neglecting hyperfine splitting. Part (a) shows the spectrum over a range of ± 5 GHz. Part (b) shows the same spectrum with the x-axis zoomed in to smaller section to illustrate the difference between the various lineshapes. In both plots the dashed red curve shows the absorption line calculated using only the inhomogeneous broadening mechanisms, the dotted green curve includes only homogeneous mechanisms, and the solid blue curve shows the Voigt lineshape which includes both.

neous nature of the lineshape tends to dominate the system dynamics for small $|\Delta|$ whereas homogeneous effects dominate for large $|\Delta|$.

3.5.5 Hyperfine Splitting and Comparison with Measurements

Now that we understand the lineshapes that occur in typical atomic absorption spectra, we are almost ready to compare theory with some experimental measurements. First though we must revisit the topic of the hyperfine interaction briefly introduced in Section 3.3.1.

The hyperfine interaction is the name given to interaction of the magnetic dipole and electric quadrupole moments of an atomic nucleus with the states of the bound electrons. Typically the magnetic dipole part of the interaction is stronger, and for the present qualitative discussion it will be sufficient to consider only this part. The interaction is similar in form to the spin-orbit interaction but is much weaker. Its size depends on the relative

orientation of the total electronic angular momentum $\hat{\mathbf{J}}$ and the nuclear angular momentum whose operator is commonly denoted $\hat{\mathbf{I}}$. This relative orientation is characterized by the total angular momentum $\hat{\mathbf{F}} = \hat{\mathbf{I}} + \hat{\mathbf{J}}$, with quantum number F . Consequently the interaction between $\hat{\mathbf{I}}$ and $\hat{\mathbf{J}}$ leads to an energy splitting between states with differing values of F [73].

Along with the presence of states with various values of F , one must also account for the existence of multiple isotopes. Naturally-occurring xenon contains 9 stable isotopes, summarized with their percent abundances in Table 3.4. Data for this table was taken from [83]. The isotope number determines the size, shape, and mass of a xenon nucleus. Changes between isotopes lead to slight alterations in excited state energies, on a level comparable with that caused by the hyperfine interaction.

Table 3.4: Stable isotopes of xenon and percent natural abundances.

Isotope:	^{132}Xe	^{129}Xe	^{131}Xe	^{134}Xe	^{136}Xe	^{130}Xe	^{128}Xe	^{124}Xe	^{126}Xe
% Abundance:	26.89	26.44	21.18	10.44	8.87	4.08	1.92	0.096	0.090

We now consider the the absorption spectrum of the $6s[3/2]_2^o$ to $6p[3/2]_2$ transition in xenon. The presence of hyperfine splitting leads to a multiplicity of resonances in this spectrum. Figure 3.5 illustrates the allowed transitions between the various hyperfine sublevels of the two involved states. Each of these allowed transitions leads to a separate absorption resonance, so we should expect a measurement of the spectrum to contain evidence of many absorption dips with varying intensities and frequency detunings.

Figure 3.6 shows the transmission spectrum of the 823 nm $6s[3/2]_2^o$ to $6p[3/2]_2$ xenon transition as measured in our lab. The spectrum can be verified by comparison with references [84] and [85]. As expected it contains several distinct absorption dips. On visual inspection, the shapes and widths of the individual transmission dips seem to be well described qualitatively by either the Gaussian or Voigt lineshapes derived above and shown in Figure 3.4. There are however small quantitative discrepancies. Notice for instance that

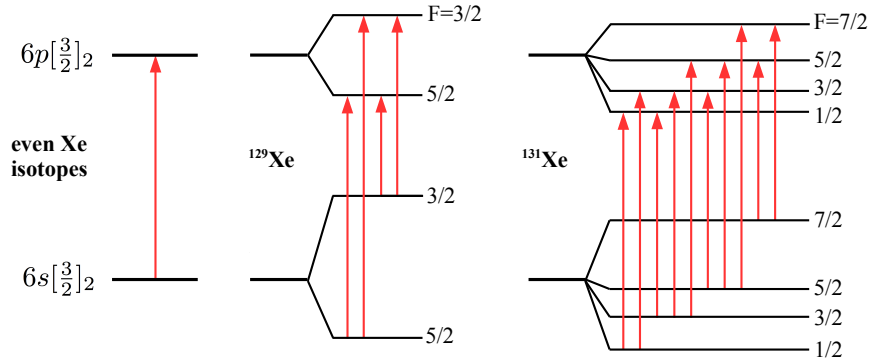


Figure 3.5: Illustration of the allowed transitions between the various hyperfine sublevels of the xenon $6s[3/2]_2^0$ and $6p[3/2]_2$ states. The even isotopes all have $I = 0$, so hyperfine splitting does not occur for them. Information for this figure was taken from p. 5 of [83].

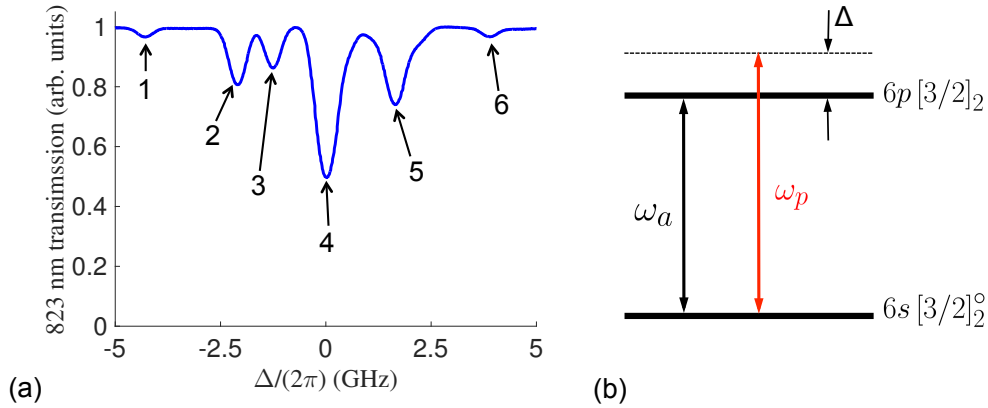


Figure 3.6: (a) Measured transmission of an 823 nm probe laser through a gas of metastable xenon, as its frequency was scanned across the 823 nm resonance. For convenience the transmission dips are labeled with the numbers 1 through 6, as shown. (b) Illustration of the energy levels and frequencies involved in the measurement. The atomic transition frequency is $\omega_a = 364.095$ THz, and the detuning parameter is defined $\Delta = \omega_p - \omega_a$.

while 21 separate hyperfine resonances exist for this transition (7 even isotopes plus 4 allowed hyperfine transitions for Xe^{129} and 10 for Xe^{131}), only 6 transmission dips are visible in Figure 3.6.

In fact all 21 hyperfine transitions are present in the spectrum of Figure 3.6, but broadening prevents some of them from being distinguished with a simple transmission measurement. Figure 3.7 (a) shows the same measurement superposed with a set of Voigt

lines calculated using the theory of Sections 3.5.1 through 3.5.4. Linewidths were calculated as before using the natural lifetime of the excited state and the Doppler broadening expected in a room-temperature gas of xenon atoms. Depths of the calculated lines were adjusted to match the experimental values, but otherwise no free parameters were used to achieve the fits. The agreement is very good for most of the dips, but for dips 4 and 5 there is marked disagreement.

This disagreement can be explained by reference to Figure 3.7 (b). This figure superposes the measured spectrum on top of a line graph illustrating the strengths and frequencies of each of the hyperfine components. Information for the various hyperfine transitions was taken from page 5 of [83]. Each of dips 4 and 5 is composed of one very strong hyperfine transition component along with a number of weaker components close by. It is easy to see that the presence of these other components could produce to the differences between the measured lineshapes and the theory.

The strong agreement in Figure 3.7 (a) verifies our theory of atomic transition line broadening, and we have developed a sufficient understanding of atomic spectra and hyperfine splitting to serve as a background for the experimental work that follows. In the next chapter we move from theory to application, as we discuss the technical requirements and challenges associated with building our experimental apparatus.

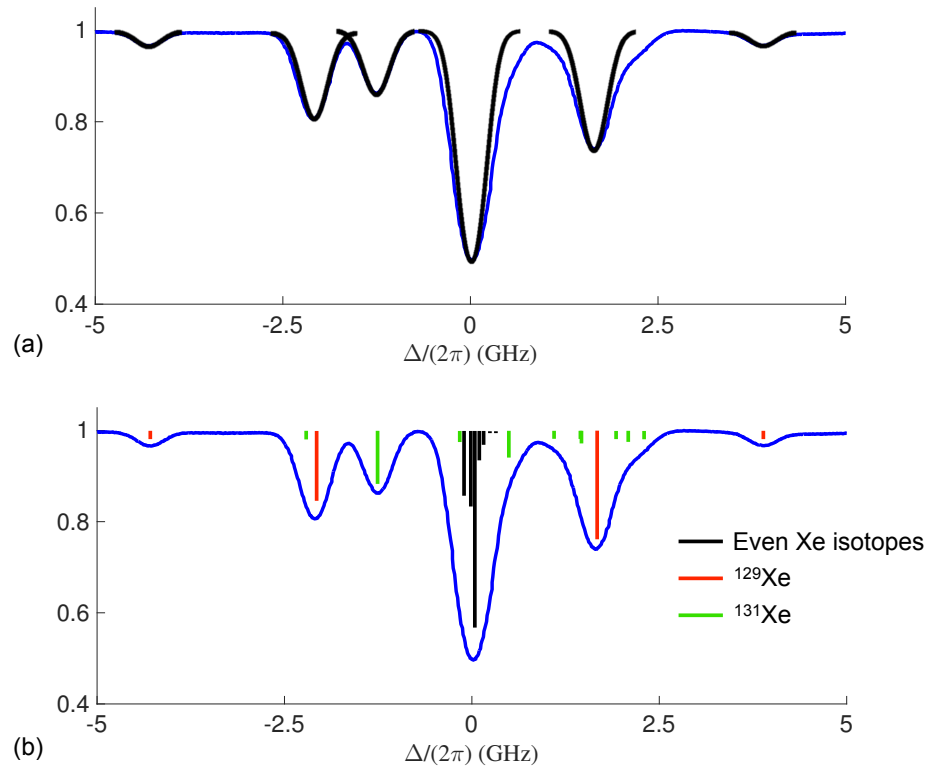


Figure 3.7: (a) Measured transmission spectrum of the 823 nm xenon transition, superposed with Voigt absorption profiles calculated using the theory of Sections 3.5.1 through 3.5.4. The agreement is very good for 4 of the dips, but the measured lineshapes of dips 4 and 5 are noticeably different from the theory. (b) Another copy of the measured spectrum, superposed with a diagram showing the frequencies and relative strengths of the various hyperfine components. Each resonance is marked with a vertical line. The height of the line denotes the relative strength of that component, and its position along the x-axis indicates its resonance frequency. Data on the strengths and frequencies of the hyperfine components was taken from [83].

Chapter 4

Experimental Methods

4.1 Overview

Cutting-edge work in experimental quantum optics requires a significant investment in equipment, supplies, and time spent designing and assembling a laboratory system. In this chapter we discuss the most important laboratory components and techniques that formed the technical foundation for the experiments discussed in chapters 5 and 6. We begin with a brief description of the vacuum system used in our work. We then describe methods used for the production of metastable xenon (Xe^*). We close this chapter with a description of our experience using fiber-coupled vs. free-space optics, and a short review of some lessons learned in handling and using sensitive high-finesse cavity mirrors.

4.2 Vacuum System

The vacuum chamber used in this work consisted of a standard 4.5” 6-way ConFlat (CF) cube. Five of the cube’s ports were closed off with window flanges and blanks, while the remaining port connected the cube with another chamber containing a capacitance manome-

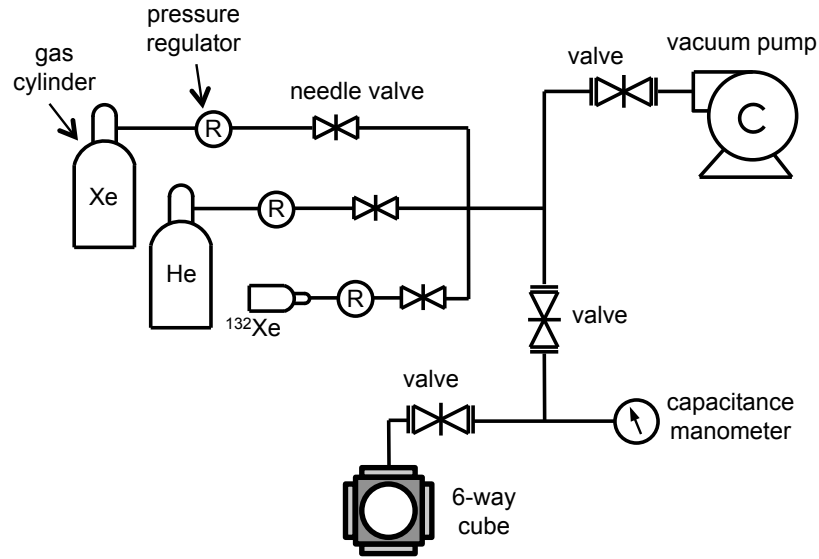


Figure 4.1: Diagram of the vacuum system used in this work.

ter. The connection was accomplished using a flexible bellows flange to facilitate the easy removal from and reattachment of the 6-way cube. A second valve linked this chamber with our gas sources. These sources included tanks of naturally-occurring xenon and of single-isotope ^{132}Xe , along with a tank of naturally-occurring Helium for use as a buffer gas. The delivery system for each gas cylinder included a pressure regulator to bridge the gap between the extremely high pressure environment of the tank with the low pressure vacuum system. Each pressure regulator was followed by an on-off valve used to stop gas flow when needed, and a needle valve to regulate the flow. The gas sources section was then connected to our vacuum turbopump (Varian TPS-Bench 9698212) through another on-off valve. The system is illustrated in diagrammatic form in Figure 4.1, and a photo of the laboratory setup is given in Figure 4.2.

4.3 Production of Metastable Xenon

The vacuum system described above was capable of removing atmosphere from our chamber to pressures below 10^{-5} Torr, and filling it with any desired density of xenon gas. The

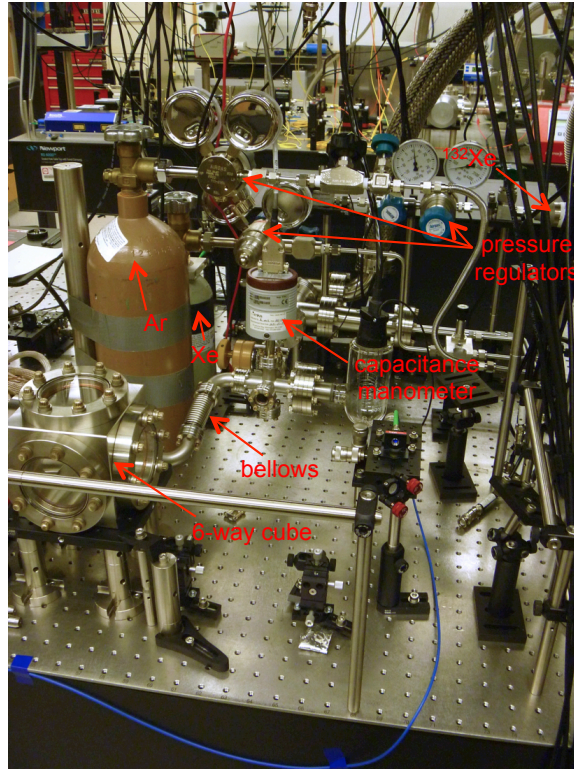


Figure 4.2: Photo of our vacuum system in the laboratory.

next step in the development of our experimental system was to devise a means for exciting xenon atoms into the metastable state. We investigated 4 separate methods of excitation: a DC plasma discharge, an RF plasma discharge, a method based on optical pumping, and a hybrid method incorporating optical pumping within an RF discharge. We will spend a short time reviewing each of these techniques.

4.3.1 DC Discharge Production

One crude but effective method of populating the xenon metastable state is to simply pump energy into the atoms randomly and incoherently. As highly-excited xenon atoms decay back to the ground state a fraction of them branch to the metastable state $6s[3/2]_2$. Because of its extremely long radiative lifetime (~ 43 seconds) atoms in this level tend to stay there for some time, and as a result the level accumulates a relatively large steady-state

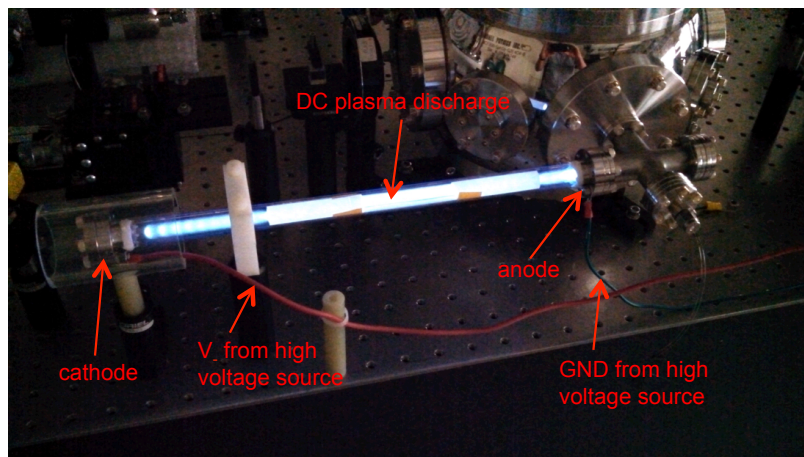


Figure 4.3: A DC discharge inside a xenon-filled vacuum chamber. A high voltage source provides a large negative voltage V_- through the red wire shown toward bottom, and ground potential through the green wire shown at the right. The photo was made available by courtesy of Todd Pittman.

population [86]. The incoherent pumping can be accomplished in a number of ways. Early in our work with Xe^* production, Todd Pittman in our group investigated the use of a DC plasma discharge.

The discharge was produced by applying a very large voltage between two electrodes inside a vacuum chamber filled with xenon gas. Once the applied voltage was strong enough to overcome the work function of the cathode, electrons streamed from the cathode to the anode, colliding randomly with xenon atoms along the way. A fraction of these collisions resulted in an electronic excitation of a xenon atom, and a fraction of these excitations resulted in the atom finally decaying into the metastable state. A photo of the DC discharge system is shown in Figure 4.3.

The DC discharge system was capable of producing a reasonable density of metastable xenon atoms, on the order of 10^{10} or 10^{11} $1/\text{cm}^3$. However, the experiment encountered several other difficulties. For strong discharge intensities electrons tended to collide with the anode with large kinetic energies, which often caused sputtering the anode material onto optical surfaces inside the vacuum chamber. Optical components cannot survive long in such an environment, so it was typically necessary to reduce the discharge intensity,

resulting in a lower density of metastable atoms. Several other disadvantages of the DC discharge system include difficulty in maintaining a stable discharge, and danger inherent in the use of a high-voltage, high-current power source. More discussion can be found in reference [87].

4.3.2 RF Discharge Production

It is also possible to produce a plasma discharge using a strong radio frequency (RF) field. Equipment required includes an RF source (an inexpensive benchtop source is sufficient) and an RF amplifier capable of providing at least several Watts of continuous power. These sources can be used to drive a resonating wire coil designed to radiate the power into a gas chamber, producing an RF plasma discharge in the chamber.

Figure 4.4 shows a schematic diagram of two possible methods for building the wire coil circuit. One option is to inductively couple the source to a resonating tank circuit composed of wire coils and capacitors. A coil of wire is an effective antenna at RF frequencies, and the inductive impedance of the coils in the tank circuit can be offset by incorporating a bank of capacitors to cancel it out at the desired frequency. This circuit is illustrated in Figure 4.4 (a). Inductive coupling allows the source to drive significantly greater current in the LC tank circuit than would otherwise be possible, depending on the ratio of the number of coils in inductors L_0 and L_1 . This can be advantageous when source power is limited.

The second option, shown in Figure 4.4 (b), is to wire the RF source directly to the resonating circuit. This is illustrated in Figure 4.4 (a). At the resonant frequency of the LC circuit the current is limited by the power output of the source and the impedance of the transmission line. Our transmission lines were 50 Ω BNC cables and our source used a 50 watt RF amplifier, so the maximum achievable current using this circuit in our lab was roughly 1 A.

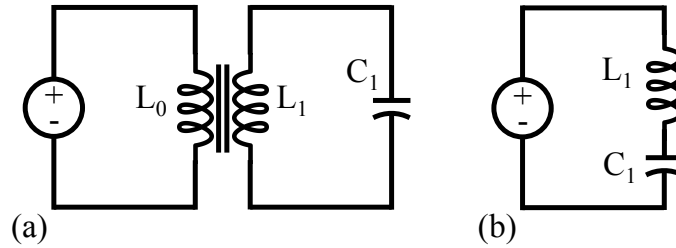


Figure 4.4: The two RF circuit designs used for the radiating wire coil in our work with RF discharge excitation. In (a) the RF source is inductively coupled to a resonating tank circuit. This design has the potential to allow a very large current to flow through L_1 , producing intense RF radiation inside the gas chamber. In (b) the source is wired directly to the tank circuit. This design has the disadvantage that the maximum current is limited by the impedance of the RF transmission line (in our case the line was a $50\ \Omega$ BNC cable), but the circuit is simple and relatively easy to build.

We typically designed our RF discharge circuits to place the resonance near 150 MHz. The actual resonance frequency usually fell within ± 20 MHz of this value. A variable frequency source was used and its frequency was swept to locate the resonance. The intensity of radiation emitted from the circuit scales directly with the current flowing through it, so during normal operation the source frequency was kept fixed at the circuit resonance. For our system the discharge tended to occur most easily when a large number of wire loops was used, when the loop radii were about $3/4$ the radius of our vacuum chamber windows, and when the loops were positioned as close to the window as possible. Also, the precise value of the circuit's resonant frequency seemed to have little effect on the size of the discharge.

Figure 4.5 provides a laboratory photo of a discharge coil circuit of the first type (a). It produced a stable discharge, but it also radiated a large amount of RF power into the laboratory and surrounding environment. This stray radiation caused a great deal of undesirable interference in many nearby pieces of laboratory equipment. Additionally, high voltages across the wire loops made the circuit quite difficult to build. The wire had to be wound very precisely to prevent any contact between adjacent conductors, since this would short-circuit the radiating coil. Use of insulated wire did not help, as the voltages

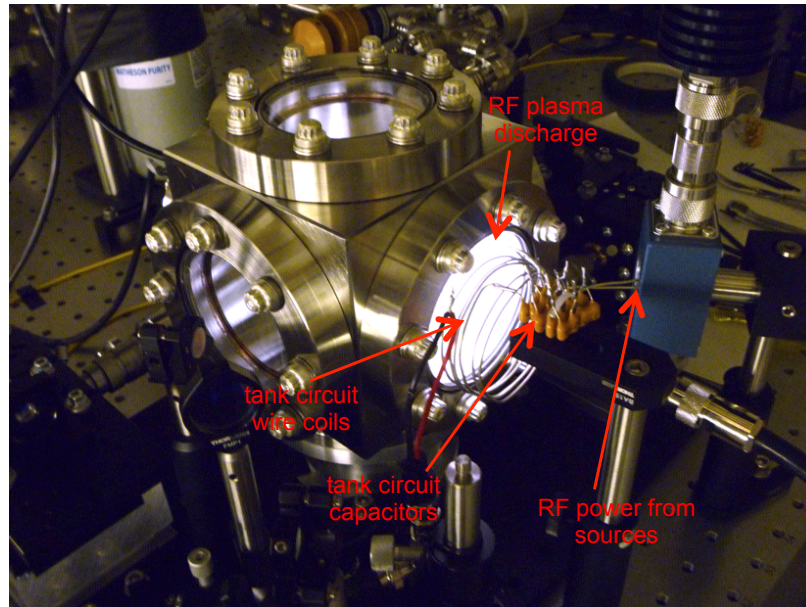


Figure 4.5: Laboratory photo of a circuit of type (a), consisting of a resonant tank circuit inductively coupled to an RF source. The circuit is shown here producing a plasma discharge in a vacuum chamber filled with xenon gas.

between loops were often strong enough to cause dielectric breakdown and arcing through the insulation.

A metal cap can be used to house the circuit and to direct the radiated energy into the gas chamber, where it would be largely dissipated in heating the gas. However, we found that the already difficult task of winding the circuit coils became almost impracticable when forced into the confined space of a metal cap. Consequently we began to design resonant circuits using the simpler schematic of Figure 4.4 (b).

Figure 4.6 shows a pair of photos of a discharge coil built using the second design (b). The image on the left shows the interior of an aluminum cap that was used to house the circuit. Layers of Teflon and plastic insulated the cap from the high voltages present in the coil. The image on the right shows the housing cap connected to our vacuum chamber and producing a discharge in xenon gas. Our source provided enough power to produce a bright, stable discharge with this circuit layout. Because of its relative simplicity this became our standard circuit design for producing RF discharges.

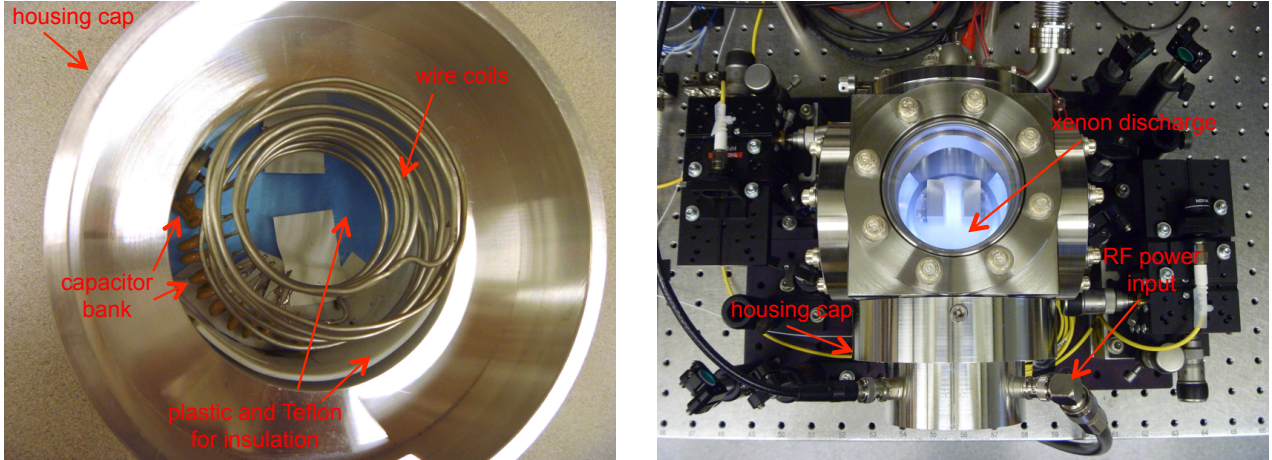


Figure 4.6: Laboratory photo of a circuit of type (b), consisting of a resonant tank circuit wired directly to an RF source. The image on the left shows the circuit inside of its metal housing cap, and the image to the right shows the system producing a plasma discharge in xenon gas.

The RF discharge techniques described in this section typically produced Xe^* densities of from 10^{10} to 10^{12} $1/\text{cm}^3$, comparable to those achieved using a DC discharge. The RF approach had the advantage though that it did not cause sputtering, hence it did not damage sensitive optical components inside the vacuum chamber. Stray RF fields emitted by the discharge circuit occasionally caused problems with other sensitive pieces of electronic laboratory equipment, but the aluminum cap shown in Figure 4.6 largely mitigated these effects.

4.3.3 All-Optical Production

The methods described in Sections 4.3.1 and 4.3.2 could be called “incoherent” excitation methods, in that they use a brute-force mechanism to pump atoms into many different excited states. It is also possible though to populate the metastable state with coherent excitation, for instance using laser fields tuned to a specific series of dipole-allowed transitions. This method is called optical production [88].

Figure 4.7 illustrates the idea behind this excitation strategy. A direct transition from the xenon ground state to the metastable state $6s[3/2]_2^o$ is dipole forbidden because

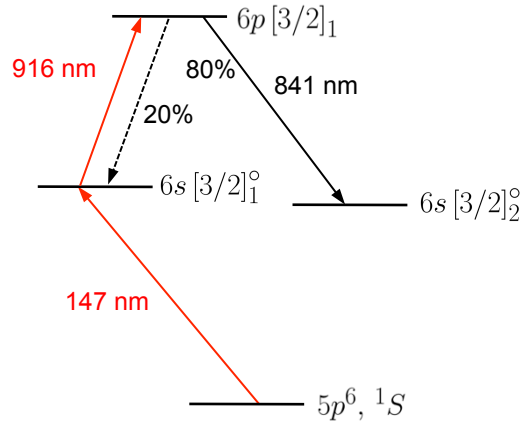


Figure 4.7: Energy level diagram for all-optical production of Xe^* . Red arrows indicate transitions that must be actively driven. The 841 nm transition labeled with a black arrow occurs as a result of spontaneous emission. The relatively large branching ratio from $6p[3/2]_1$ to $6s[3/2]_2^o$ facilitates the buildup of population in the metastable state. The branching ratio was estimated using data found in [78].

of the difference of total angular momentum between the two states, $\Delta J = 2$. Since these two states also have opposite parity, an optical transition between them requires at least 3 photons. First a 147 nm vacuum ultraviolet (VUV) light source can be used to excite ground state atoms into the $6s[3/2]_1^o$ state. A 916 nm laser can then transfers this population to the state $6p[3/2]_1$. This state spontaneously decays to the metastable state $6s[3/2]_2^o$ with a branching ratio of roughly 80%, and since the rate of radiative decay from this state is extremely slow it can accumulate a large population.

The difficulty of implementing all-optical production comes from the need for a 147 nm radiation source. Light of this wavelength could be generated by frequency quadrupling a 588 nm laser. The efficiency of this process though is typically very low, so the resulting 147 nm beam would be quite weak. Additionally VUV radiation is strongly absorbed in air, so the final step of frequency conversion would need to take place under vacuum [75]. This would significantly complicate the technical requirements of an experimental system.

Alternatively the required VUV light can be produced by a plasma discharge lamp. These lamps use an electrical discharge to excite gas atoms in a vapor cell. Atoms excited in the discharge radiate when they undergo spontaneous decay, which results in the emission of light from the lamp. The frequency of the dominant atomic transition determines the frequency of the emitted radiation. Xenon discharge lamps capable of producing narrowband 147 nm VUV light are commercially available.

We chose to attempt all-optical production using a xenon discharge lamp bought from Resonance Ltd., and a Toptica DL Pro diode laser tuned to 916 nm. Though the experiment was quite simple in theory several months were spent trying to find evidence of Xe^* production. We implemented various methods of measuring the presence of metastable xenon in the system, but in the end we found no evidence at all that 147 nm photons emitted from the lamp led to the production of Xe^* . This may have been the result of a faulty lamp, or of degradation of the MgF_2 window connecting the lamp with our vacuum chamber (these windows transmit VUV light reasonably well, but their transmission tends to deteriorate over time). It seems likely that our discharge lamp simply did not provide enough 147 nm photons to produce a measurable density of metastable atoms.

Figure 4.8 illustrates one of the difficulties encountered during this period. Note from Figure 4.7 that without the 916 nm field it is not possible to excite the metastable state using the all-optical method. We discovered at one point that our discharge lamp was producing metastable atoms in our vacuum chamber, but that it did so without the help of any 916 nm light. On closer examination we discovered that in these cases the lamp was generating an RF discharge within our vacuum chamber. As far as we could tell, the excitations to the metastable state were produced entirely by this secondary discharge. Thus the discharge lamp added nothing to our system, since it only provided us with a more expensive and less effective means of reproducing the results described in Section 4.3.2. Shortly after this discovery we stopped pursuing all-optical production in favor of the other, more convenient and more practical methods. We note before moving on that other groups

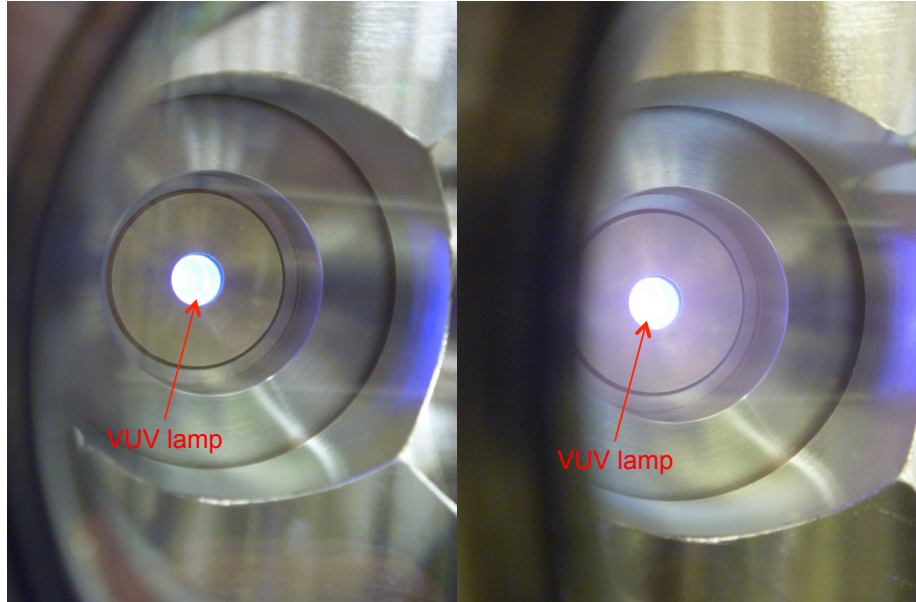


Figure 4.8: Left: view of the VUV xenon discharge lamp from within our vacuum chamber when the chamber had been evacuated. Right: the same view of the discharge lamp when the chamber had been filled to 0.14 Torr with naturally-occurring xenon. Notice that in comparison with the left image, the presence of a faint purple glow is evident in photo on the right, near the discharge lamp window. This confirmed our suspicion that the lamp was producing a secondary discharge within our vacuum chamber.

have succeeded in performing all-optical metastable production with other noble gas atoms [88, 89], but to our knowledge this has not yet been done with xenon.

4.3.4 Optically-Enhanced Production

After the frustrations described in the previous section we began to look for alternative ways of producing 147 nm photons. It occurred to us that any bright RF discharge in xenon gas should produce these photons. Rather than using a relatively weak VUV lamp as a source, we decided attempt optical production of Xe^* atoms within one of our own RF discharges. This study resulted in a publication which contains many of the details of our implementation [90]. To minimize redundancy we will only briefly summarize them here, adding a few qualitative comments along the way for the purpose of illustration. The reader already familiar with reference [90] may wish to skip ahead to Section 4.4.

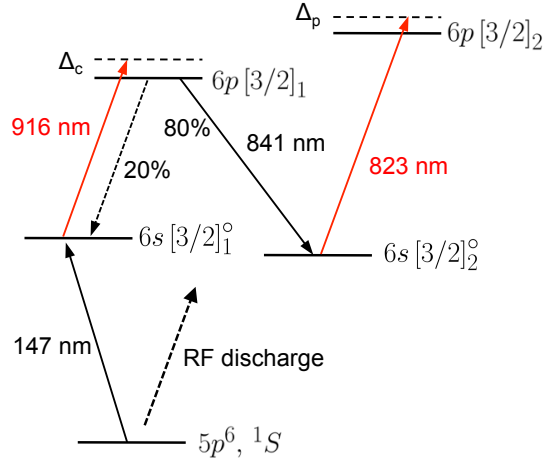


Figure 4.9: Energy level diagram for the experimental demonstration of optically-enhanced Xe^* production.

Figure 4.9 illustrates the energy level diagram used in this experiment. The transmission of an 823 nm laser tuned to the $6s[3/2]_2^o$ to $6p[3/2]_2$ transition was used to measure the density of Xe^* . The detunings of the lasers from atomic resonance are defined as $\Delta_c = \omega_c - \omega_{a,c}$ and $\Delta_p = \omega_p - \omega_{a,p}$. Here ω_c and ω_p are the angular frequencies of the 916 nm control and 823 nm probe beams, respectively. The parameters $\omega_{a,c}$ and $\omega_{a,p}$ represent the angular frequencies of the atomic $6s[3/2]_1^o$ to $6p[3/2]_1$, and $6s[3/2]_2^o$ to $6p[3/2]_2$ transitions, respectively.

The operation of this excitation scheme may be qualitatively understood as follows. First an RF discharge was applied in a gas of xenon atoms, transferring a large number of atoms into many different excited states. As these states decayed back to ground a fraction of them branched through the metastable state $6s[3/2]_2^o$, resulting in an accumulated population there. However, many other branching chains passed instead through the state $6s[3/2]_1^o$. Atoms in this state rapidly decayed to ground and emitted a 147 nm photon. Each of these emitted VUV photons had a relatively high probability of undergoing near-resonant scattering by another xenon atom. At relatively high gas densities the mean free path of these photons is small enough that their propagation through the chamber resembles

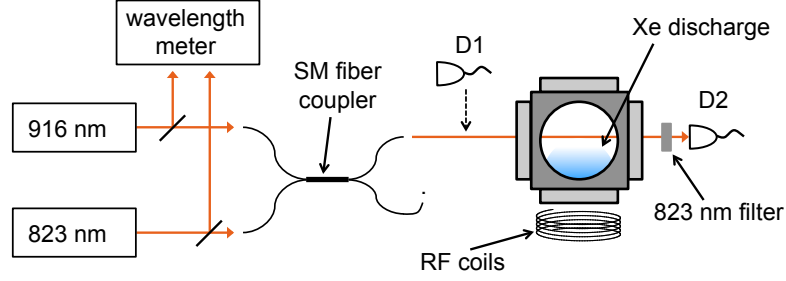


Figure 4.10: Diagram of the experimental system for performing optically-enhanced production of Xe^* .

a random walk [88]. Hence in addition to metastable excitations, the discharge produced a large number of 147 nm photons, which diffused outward through the xenon gas.

Next a laser field was applied and tuned to the 916 nm transition, transferring the $6s[3/2]_1^{\circ}$ state population to the $6p[3/2]_1$ state. This state preferentially decays to the $6s[3/2]_2^{\circ}$ state, so the net result of the application of the laser was an increase in the density of metastable atoms. It is worthwhile to note that the $6s[3/2]_1^{\circ}$ state population in this method was produced by a combination of direct excitation from the discharge, decays from higher-lying atomic states, and absorption of 147 nm photons emitted by other xenon atoms.

Figure 4.10 illustrates the experimental setup used to implement this excitation method, and to measure the resulting density of Xe^* . Two Toptica DL Pro tunable diode lasers were used, one tuned to 916 nm to implement our excitation method and the other tuned to 823 nm to measure the optical depth of the $6s[3/2]_2^{\circ}$ to $6p[3/2]_1$ transition. A HighFinesse WSU30 wavelength meter continuously monitored the frequencies of both beams. The two fields were coupled into a common single-mode (SM) optical fiber to assure good mode matching, and sent through an RF discharge in our xenon-filled vacuum chamber. Detectors D_1 and D_2 were used to monitor the power of the 823 nm beam and to measure its transmission through the chamber. The experiment consisted in measuring the transmission of the 823 nm field for various values of the 916 nm input power and of the detunings Δ_c and Δ_p .

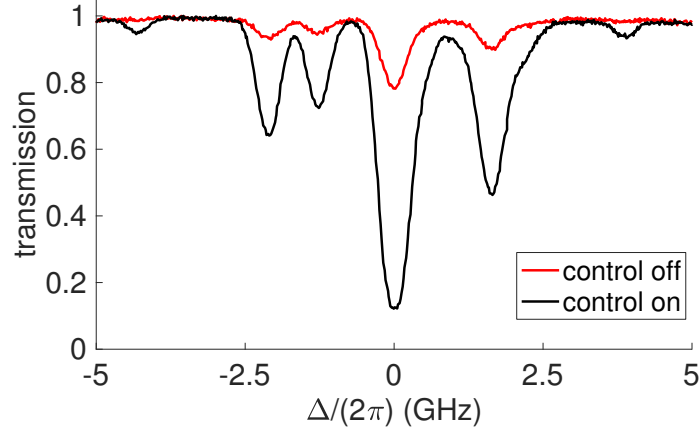


Figure 4.11: Measured absorption spectrum of the 823 nm $6s[3/2]_2$ to $6p[3/2]_2$ transition in xenon when the 916 nm control beam was turned off (red curve) and when it was turned on at our maximum available power of ~ 4 mW (black curve).

Figure 4.11 shows the main result of this investigation. The absorption spectrum of the metastable xenon atoms was measured by sweeping the frequency of the probe field across the xenon $6s[3/2]_2$ to $6p[3/2]_2$ transition resonance. The black curve in Figure 4.11 shows the spectrum measured with the control beam turned off. This spectrum matches the measurements shown in Section 3.5.5. The absorption of this curve was caused by Xe^* produced in the RF discharge. The red curve shows the spectrum as it appeared when the control beam was switched on. Application of the 916 nm field increased the density of Xe^* by roughly a factor of 11 [90].

The increased metastable density possible with the optically-enhanced method may be particularly useful in situations which require a large Xe^* density but can only tolerate a relatively weak discharge. This might be the case if, for instance, excess heating by the discharge tends to disrupt a sensitive piece of equipment located nearby. Optical enhancement could then be used to compensate for the lower Xe^* densities achievable by a weaker discharge.

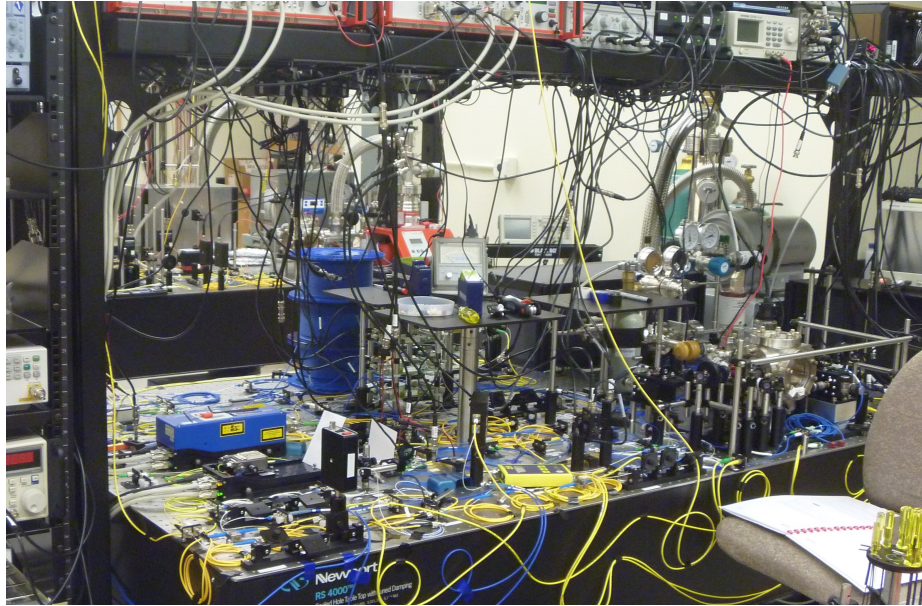


Figure 4.12: Photograph of the experimental system as of July 10, 2015. The setup included several dozens of fibers and fiber-coupled components.

4.4 Fiber-Coupled Optical Components

For decades experiments in optics have been performed using bulk laboratory optical elements - i.e. cube beam splitters, Glan-Thompson polarizers, lenses, mirrors, etc. More recently however, the success of optical fiber in the telecommunications industry has led to a wide range of advances in fiber optical technology. As of this writing most commercially available optical components can be bought in either the more traditional bulk free-space variety or in a fiber-coupled form. As a result it has become possible to build most of one's experimental optical system within fiber.

Research groups and experimental systems tend either to follow the traditional approach of using free-space optical elements or to depend more exclusively on fiber-coupled elements. Our group at UMBC has opted to focus on the use of fiber. Consequently, the experimental systems used in this work were built almost entirely of single-mode (SM) fiber and fiber-coupled components. Figure 4.12 shows a photo of the laboratory system used to perform the measurements of Chapter 6, as an illustration of a typical setup.

Fiber-coupled experimental systems have the important advantage of increased modularity and interchangeability. For instance, an experimenter might build a complete optical system, and subsequently decide that it should be altered by the addition of one more component. If the experiment was built in fiber it would suffice to disconnect the relevant fiber couplings in the system and reconnect them to the new element. In contrast, insertion of an additional component into a system built with free-space bulk optics typically requires very careful placement and tedious realignment of all the affected elements. The use of fiber-coupled components can significantly reduce the amount of time and effort required to build and troubleshoot an experiment. However, it carries a set of disadvantages as well. The most important of these include bend-induced birefringence, time-dependent changes in refractive index, and spurious back-reflections.

Bend-induced birefringence occurs whenever an optical fiber is strained in a direction orthogonal to the fiber axis. Fibers are made of glass. Glass is an amorphous substance without any well-defined crystal shape or preferred orientation, so it is not intrinsically birefringent. Bending of an optical fiber though introduces strain into the glass and breaks the material's natural isotropy. The result is an induced birefringence, with the strength of birefringence depending on the degree to which the fiber has been bent. On one hand this phenomena has been exploited to design fiber polarization controllers (FPC's), which are essentially fiber-based versions of variable optical waveplates. On the other hand, if bending is not very carefully controlled (and this is essentially impossible in a laboratory environment), SM fibers tend to scramble optical polarization states in an unpredictable way. This scrambling can be un-done through the use of an FPC, but as laboratory temperature and air currents change throughout the day the polarization state must be periodically monitored and corrected. This may need to be done once every couple of hours, depending on the sensitivity of the measurements being performed. Thus the obstacles of bend-induced birefringence can be overcome, but this often requires additional planning and labor.

In addition to bend-induced birefringence, time-dependent index changes can also cause problems. The refractive index of an optical fiber undergoes small changes over time, due to changes in temperature and other ambient conditions. Most of the time these changes are too small to pose any concern, but they need to be taken into account in the construction of fiber-based interferometers. For example fiber-based Mach-Zehnder interferometers tend to be unstable, as the difference between the refractive indices of the two arms varies randomly over time and washes out the interference. Active phase stabilization can counteract the problem to a great degree, but it also adds to the complexity of an experiment setup. Sagnac interferometers on the other hand are relatively stable, since the field amplitudes in both arms travel through the same length of fiber.

A further difficulty common in the use of fiber is the presence of back-reflections from fiber surfaces. The capacity of SM fiber to couple light of various frequencies into a common single mode is one of its most appealing advantages as a laboratory tool. Coupling light fields from one fiber to another can be difficult because of the strict mode-matching requirements. Commercially-available FC/PC connectors though are carefully polished and follow tight tolerances that make the process quite easy. Connecting two of these fibers is nearly as simple as connecting electrical cable. A side-effect of the careful polishing though is that light reflected from a fiber tip couples back into the fiber with relatively high efficiency. In a large optical setup with dozens of fibers these back-reflections can occur in many places at once. Taken together these reflecting surfaces comprise a complicated series of low-finesse, nested Fabry-Perot cavities. The presence of these spurious Fabry-Perots (FP's) in an optical beam path leads to undesirable intensity fluctuations in the transmission spectrum of an experimental system. To make matters worse, variations in the fiber's optical index cause this spectrum to shift over time.

Figure 4.13 illustrates the effects of low-finesse FP's along an optical fiber. The image on the left shows an oscilloscope plot of the transmission spectrum of an optical cavity of moderate finesse, measured using a fiber-based optical system. The plot was

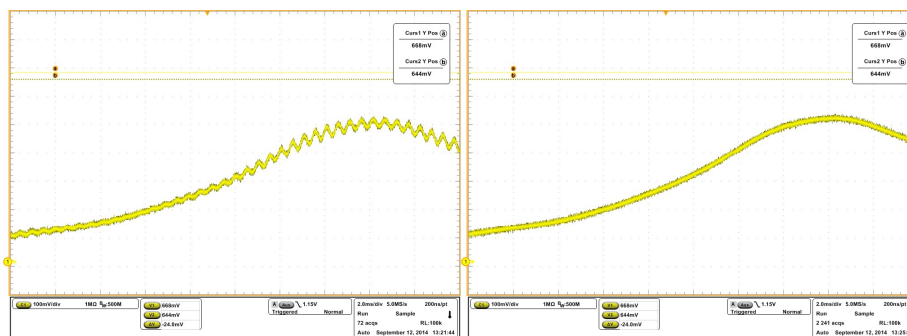


Figure 4.13: Oscilloscope traces showing the transmission of a tunable laser as its frequency was swept across a range of roughly 500 MHz. The image on the left shows the spectrum measured under normal circumstances. The photo on the right shows the transmission after measures were taken to eliminate a spurious Fabry-Perot from the beam path.

generated by scanning the frequency of an input laser over a range of roughly 500 MHz and observing the output on a standard photodetector. The spectrum includes a broad peak several hundreds of MHz wide superimposed with a series of small, fast oscillations. The smaller oscillations are the result of a low-finesse FP occurring between fiber end-faces. In many cases these oscillations constitute a systematic error mechanism for the measurement system, and they need to be eliminated or compensated for.

It is generally possible to eliminate these undesirable Fabry-Perot effects by using angled FC/APC fiber connectors. The faces of these connectors are polished at an angle so that back-reflections scatter out of the fiber. The image on the right side of Figure 4.13 shows a measurement of the same spectrum made after one fiber connector had been replaced with an angled FC/APC version. The spurious FP oscillations were eliminated. In theory the use of angled connectors solves the problem of spurious back-reflections. In practice though our laboratory was stocked with many flat FC/PC-connectorized components and relatively few components with angled connectors. As a result we encountered these spurious oscillations on many occasions. We will revisit this problem when we discuss our initial measurements of light absorption in a xenon-filled cavity, in Section 5.6.

4.5 The Proof-of-Principle Optical Cavity

4.5.1 Cavity Design

The high-finesse optical cavity was the most important component of our experimental system, and the most sensitive. The work described here was our group's first experience with high-finesse Fabry-Perot cavities, so we decided to begin with a relatively simple and stable design. Experiments performed using this cavity would function as proof-of-principle demonstrations. Once this was done, we planned to produce weak single-photon nonlinearities by simply building an improved cavity and incorporating it into the remainder of the experiment. This first cavity consisted of a pair of superpolished dielectric mirrors placed $d = 2.5$ cm apart, with radii of curvature $R = 2.5$ cm. A cavity with $d = R$ is referred to as a confocal cavity, since the foci of the two mirrors fall on the same point. The mirrors were purchased from the company Advanced Thin Films, located in Boulder, CO. The reflectivities of the mirrors were roughly $R = 99.9\%$, giving our cavity a finesse of about 3,000. The free spectral range was $FSR = 6.0$ GHz and the linewidth was $\delta f \approx 1.5$ MHz. The width of the fundamental mode at the beam waist was roughly $120 \mu\text{m}$.

The prospect of handling high-finesse cavity mirrors was initially a intimidating one. Mirrors used in state-of-the-art Fabry-Perot cavities are often so sensitive that the presence of a single microscopic dust particle on the mirror face can destroy the cavity. In practice though we found our 99.9% reflecting mirrors to be quite robust. Each of our cavities was assembled in air, taking care only to avoid touching the mirror surfaces. Cavities that were to be left in the lab outside of vacuum were kept in a sealed plastic bag or covered with tin foil, and this seems to have been sufficient protection. Several other groups use mirrors with reflectivities of roughly 99.999%. These are quite a bit more sensitive, but they can reportedly be assembled and stored in air with little risk as well (thanks to Dr. Luis Orozco from the University of Maryland, College Park for this piece of advice). Our group

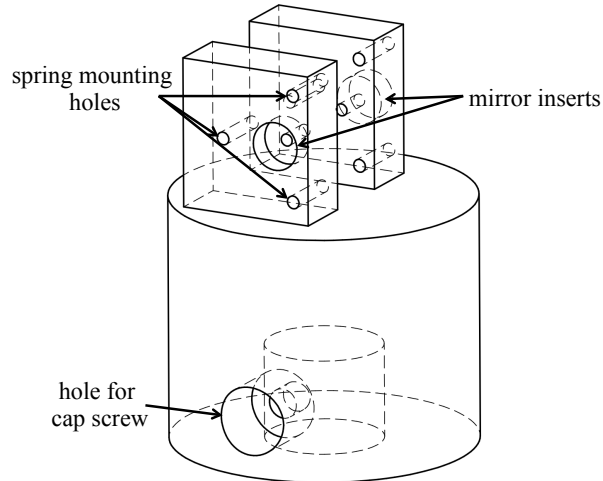


Figure 4.14: Diagram of the nickel block used to house the cavity mirrors.

has recently built a cavity with mirrors of this quality, and it is currently being tested. In Chapter 7 we review some of our recent progress along these lines.

Figure 4.14 shows a diagram of the nickel block that was used to hold the cavity mirrors. Piezoelectric elements (piezos) are often used to mount cavity mirrors, since they allow fast active tuning of the separation distance d . In our case though the RF discharge used to produce Xe^* posed a danger to any piezos in our vacuum chamber. The presence of an ionized gas in the chamber could facilitate arcing between the piezo's electrodes, which would destroy the piezos and probably damage our cavity mirrors as well. As a result we decided to control the separation between mirrors through temperature. Nickel, rather than stainless steel, was chosen for the cavity housing because of its high thermal conductivity ($90.9 \frac{\text{W}}{\text{m}\cdot\text{K}}$) and coefficient of thermal expansion ($13.0 \frac{\mu\text{m}}{\text{m}\cdot\text{K}}$).

The block was designed using the Solid Edge software package. A cylindrical design was chosen to allow the block to be quite large, for better thermal stability, and still to fit easily inside the vacuum chamber holes for mounting. A pair of rectangular “wings” were machined into the top of the block with insets for the mirrors, and with a small hole drilled through the center of each inset to leave space for light to couple into the cavity.

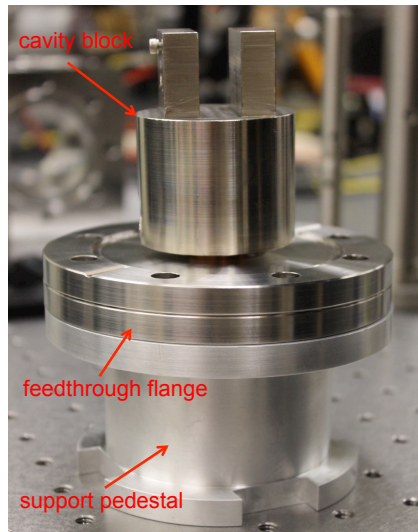


Figure 4.15: Photograph illustrating the mounting of the cavity on a vacuum feedthrough flange within the vacuum chamber. The image shows the assembled system before integration into our 4.5” vacuum cube.

Separate screw holes provided anchor points for springs that held the mirrors in place. The springs were shaped by hand from stainless steel shim stock using pliers and tin snips.

Figure 4.15 illustrates the process of integrating the cavity system with our vacuum chamber. After the mirrors were installed, the cavity block was mounted on a copper vacuum feedthrough flange. The feedthrough provided mechanical support as well as thermal contact with the cavity. The flange was placed on a custom-built aluminum pedestal before being mounted within our vacuum chamber. A copper disk was custom-machined to fit around the bottom end of the feedthrough rod and glued in place using a thermally-conducting epoxy (Electrodag 5810). Heaters and thermistors were then glued into the disk, as shown in Figure 4.16. This allowed us to monitor and control the temperature of the feedthrough rod and of the cavity block. A temperature change of only a fraction of a degree C was enough to sweep the cavity transmission spectrum by a full FSR. Figure 4.17 shows the completely assembled cavity inside an RF discharge within the vacuum chamber.

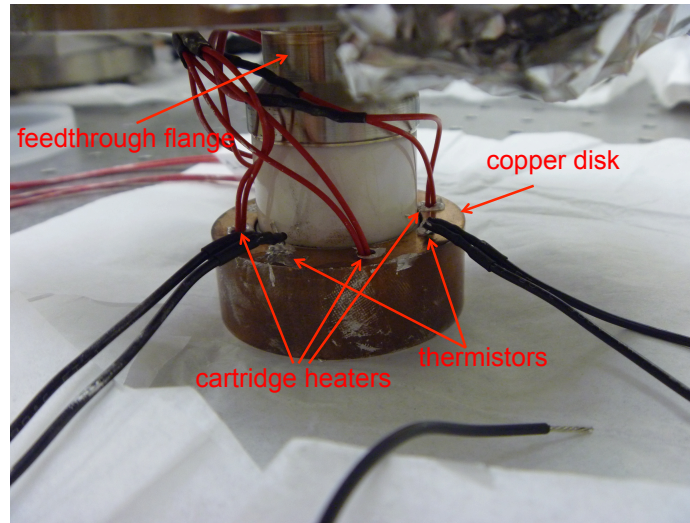


Figure 4.16: Photograph of the copper disk used to control the temperature of the vacuum feedthrough rod. The thermal contact between the feedthrough rod and the cavity block allowed us to control the cavity temperature using these heaters.

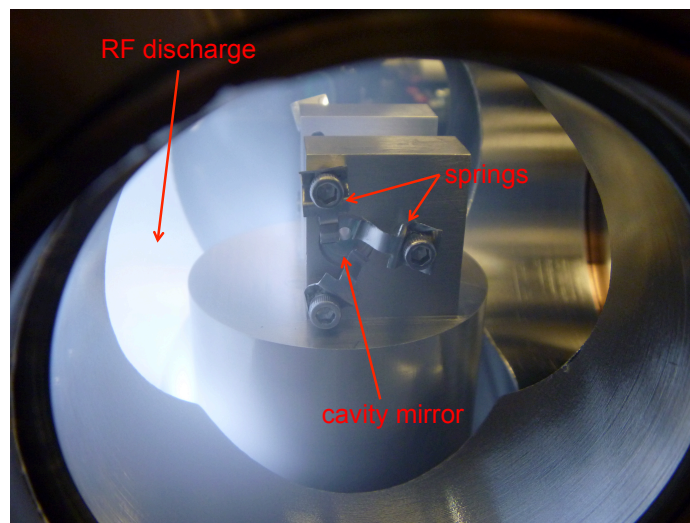


Figure 4.17: Photo of the completed cavity within an RF discharge in the vacuum chamber.

4.5.2 Early Work with the Cavity

After the cavity was assembled considerable time was spent looking for the transmission modes. Figure 4.18 (a) shows a sample of the cavity transmission spectrum as it appeared soon after being first observed. In the confocal configuration, the resonant frequencies of all higher-order transverse modes either coincide with exactly or fall halfway between the

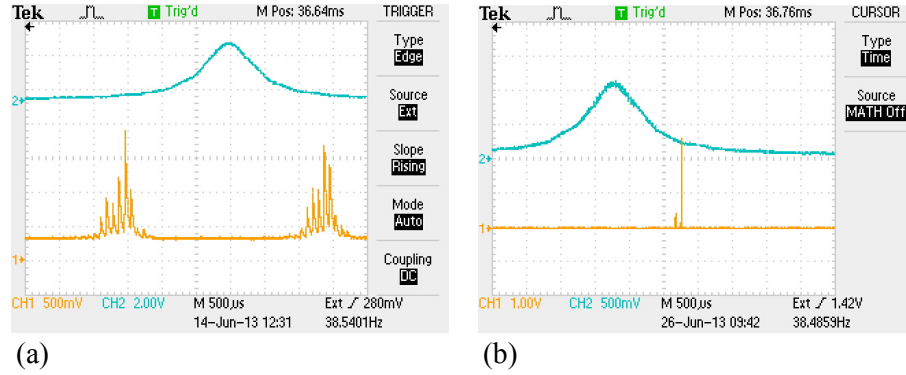


Figure 4.18: (a) Oscilloscope trace of cavity transmission spectrum as seen soon after its first finding. (b) Transmission spectrum as seen when alignment was improved to reject all modes other than the fundamental. For both (a) and (b), the blue (upper) trace shows the transmission through a commercial etalon used as a reference and the yellow (lower) trace shows the high finesse cavity transmission. Distance along the x-axis is proportional to the change in frequency of the probe light field.

fundamental mode frequencies. If a cavity is nearly but not exactly confocal the higher-order modes are slightly detuned, with the size of the detuning increasing linearly with mode number. In the case of relatively poor optical alignment a train of peaks appears in the transmission spectrum, as in Figure 4.18 (a). The fundamental mode lies at one end of the train with the other modes trailing away from it. This allowed an iterative adjustment process to isolate the fundamental mode, resulting in a transmission spectrum closer to the one in Figure 4.18 (b).

As an aside, we note that the potential for some confusion exists in the definition of the free spectral range of an exactly confocal cavity. When coupling into multiple transverse modes simultaneously, the peaks in the transmission spectrum of such a cavity occur at frequency intervals of $\frac{c}{4nd}$. However this is simply a result of coupling into multiple modes. The free spectral range for a given transverse mode is still $FSR = \frac{c}{2nd}$, as described in Section 2.1.

Figure 4.19 illustrates a serious problem discovered soon after our initial observation of the cavity's fundamental mode. On-resonance transmission through the cavity was not constant in time but varied chaotically, often on timescales of a few seconds. During

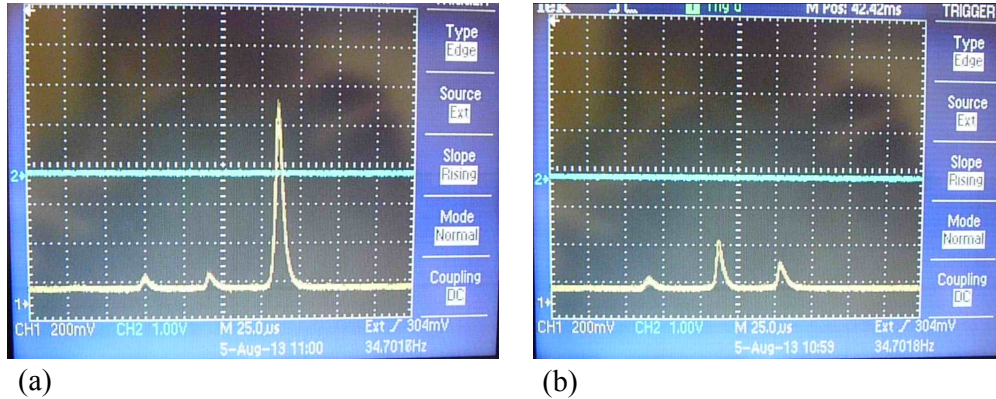


Figure 4.19: (a) Oscilloscope trace of cavity transmission spectrum with good coupling into the fundamental mode. (b) The same spectrum observed approximately 30 seconds earlier. In both (a) and (b) the yellow (lower) trace shows the high finesse cavity transmission. The fundamental mode transmission peak clearly visible in (a) had almost disappeared in (b).

some trials the spectrum remained quite stable for a whole day, while on other occasions it was nearly impossible to align the cavity input beam because of the chaotic instability.

Much time was spent attempting to understand the chaotic transmission variations. Several possibilities were suggested, but no progress was made until it was observed that bending or disturbing the optical fibers in the experiment tended at times to aggravate these variations in the cavity transmission. This suggested that something outside of the xenon-cavity system might have been responsible for the instability. Thus far these tests had all been performed with 853 nm light. When we began soon after this to probe the cavity transmission using a different laser at 823 nm, we found the instability to be even worse.

Figure 4.20 illustrates the cavity transmission instability as observed with the 823 nm laser. For this test the laser intensity was split with a fiber coupler before being sent to the cavity, and a detector was used to monitor the intensity at the unused coupler output. Figure 4.20 shows both the unused coupler output and the cavity transmission. The cavity peak was deformed with sharp intensity jumps. We expected variations in the output intensity at the unused coupler also, because of spurious FP's present in our fiber system as described earlier in Section 4.4. It was surprising though to see that sharp jumps also occurred in

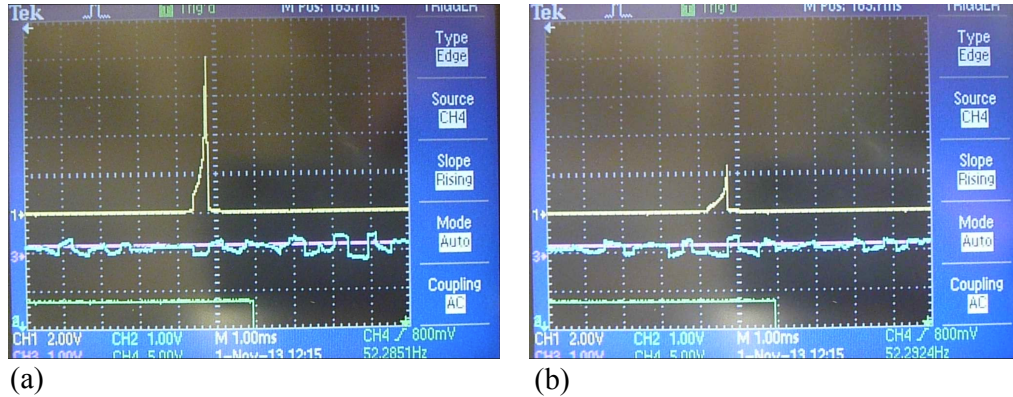


Figure 4.20: (a) Oscilloscope trace of cavity transmission spectrum when probed with the 823 nm laser. (b) The same spectrum observed approximately 5 seconds later. In (a) and (b) the yellow (upper) trace shows the cavity transmission and the blue (lower) trace shows the laser intensity as observed before passing through the cavity. The pink and green traces were not used. In both (a) and (b) the peak contained sharp jumps in transmission, each of which occurred at exactly the same point as a smaller jump in the observed laser intensity, suggesting a correlation between the two.

the transmission through the unused output, lining up exactly with the ones observed in the cavity.

Figure 4.21 shows the results of another test. Our High-Finesse wavelength meter was used to monitor the frequency tunable diode lasers being used to probe the cavity transmission. An optics system was assembled in which the user could choose between extinguishing the laser beam at an attenuator or allowing it to pass on to the rest of the setup. The setup contained a number of fiber-to-free-space interfaces that reflected a fraction of the beam back into the laser head. Thus the effect of these back-reflections could be quickly toggled on and off, and the difference observed. Figure 4.21 shows frequency as a function of time for the 853 nm laser used in this setup. At $t = 0$, back-reflections were suppressed and the frequency behaved normally. At $t \approx 17$ seconds the attenuation was removed and back-reflections were allowed, leading to mode-hopping of the laser frequency. Reflections were suppressed again at $t \approx 45$ seconds and the frequency behavior returned to normal.

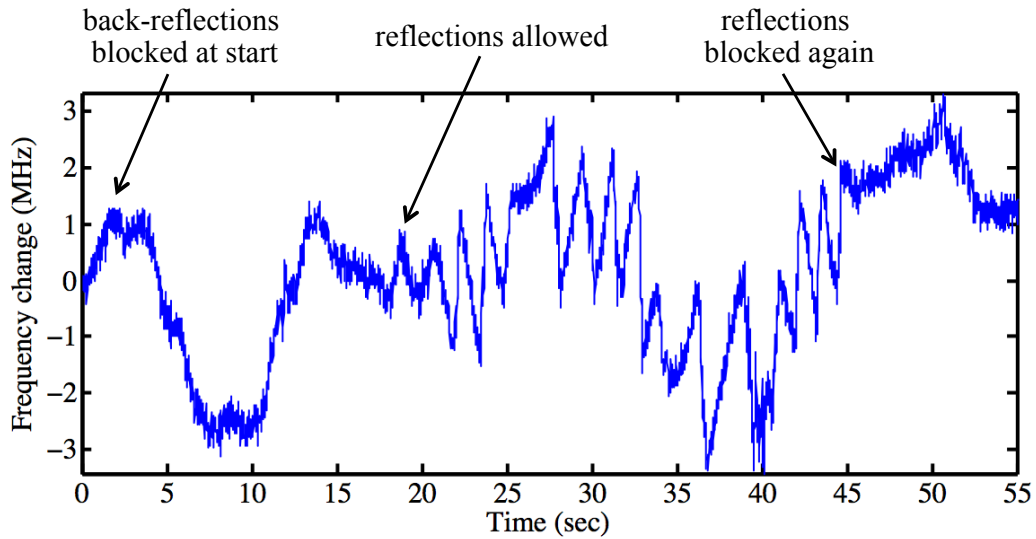


Figure 4.21: Frequency of 853 nm laser as a function of time, relative to a fixed reference. Back-reflections were suppressed for $0 < t < 17\text{s}$ and for $45\text{s} < t < 55\text{s}$, and allowed for $17\text{s} < t < 45\text{s}$. The frequency behaved normally when back-reflections were blocked, but showed numerous small mode hops when reflections were allowed.

From Figure 4.21 it was clear that light reflections coupling back into the laser diode caused frequency instability. It manifested itself in mode hops and in unpredictable narrowing and/or broadening of the laser linewidth. The instabilities were small, on the order of 1 to 2 MHz, but since our cavity linewidth was only 1.5 MHz they noticeably distorted the appearance of the transmission peak.

Because of 30 dB of optical isolation built into our laser, the back-reflected light coupling into the laser diode was about 50 dB weaker than the outgoing beam. It was difficult to believe that back-reflections of such small amplitude could cause such a pervasive problem. However, continued testing repeatedly confirmed our suspicions. Finally we bought and installed an additional 30 dB of optical isolation into each laser, and the cavity transmission instability disappeared.

Chapter 5

Ultra-Low Power Absorption Saturation

5.1 Overview

With the laser instabilities of Section 4.5.2 resolved, the xenon-cavity system was ready to perform experiments in nonlinear optics. As a preliminary step we used this proof-of-principle cavity system to measure ultra-low power absorption saturation on the $6s[3/2]_2$ to $6p[3/2]_2$ transition of metastable xenon. This allowed us to demonstrate the strength of the nonlinearity achievable with this system. The reader familiar with reference [34] should note that, while some of the content in this chapter was drawn from that work, considerable new material has been added as well.

5.2 Absorption in a Cavity

The saturation behavior of an atomic medium within a high-finesse cavity is markedly different from that of the same medium without the cavity, because of the interaction of atomic absorption with the resonant nature of the cavity. In a single-pass configuration (i.e. with no cavity), attenuation of a light field traveling through an absorbing medium results simply

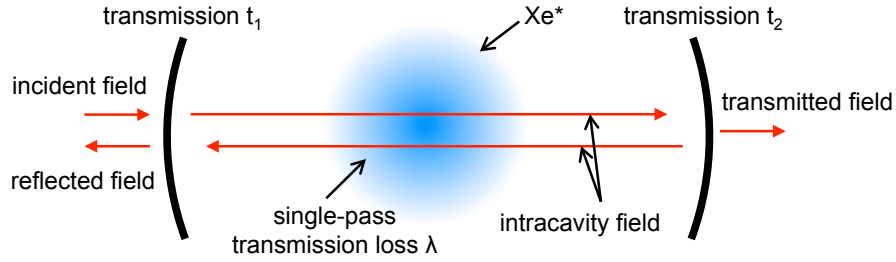


Figure 5.1: Diagram illustrating our Fabry-Perot cavity and the parameters relevant to critical coupling. Intracavity optical losses arise both from absorption by Xe^* atoms λ and from transmission through the output mirror t_2 .

in a reduction of the transmitted field intensity. In a cavity however, absorption leads also to a redistribution of the remaining field energy.

We saw in Section 2.1 that an on-resonance field incident on optical cavity tends to couple into a cavity, while an off-resonant field does not. This occurs because efficient coupling depends on constructive interference between the input field and the field circulating within the cavity. Thus the amount of light coupled depends on the condition of resonance, and also on the relative amplitudes of the interfering fields. These relative amplitudes are influenced by the relationships between the various intracavity loss mechanisms.

Figure 5.1 illustrates the parameters relevant to the description of efficient cavity coupling. Perfectly efficient coupling occurs when the loss inside the cavity, including the transmission of the output mirror, is equal to the transmission of the input mirror. Such a cavity is referred to as being “critically coupled” [91, 92]. Using the notation of the figure the condition for critical coupling is $t_1 = t_2 + 2\lambda$. For the cavity used in our work $t_1 \approx t_2$, so critical coupling should occur only in the absence of absorption losses.

Thus the losses induced by the presence of metastable xenon atoms in our cavity should have the effect not only of attenuating the intracavity field, but also of spoiling the cavity coupling. We can see precisely how this occurs by repeating the derivation of Section

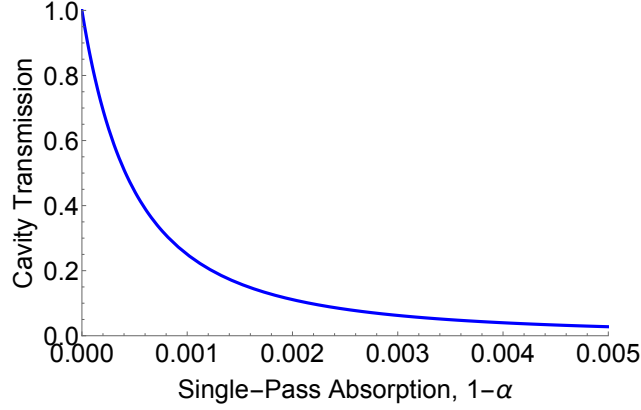


Figure 5.2: Cavity transmission plotted vs. the loss α in a single pass through the intracavity medium.

2.1 and including absorption losses. The result is a more general version of Eq. 2.2:

$$I_t = \frac{T_1 T_2 \alpha}{1 + R_1 R_2 \alpha^2 - 2\sqrt{R_1 R_2} \alpha \cos\theta} I_i, \quad (5.1)$$

where $\alpha = 1 - \lambda$ is the fraction of optical intensity transmitted after a single pass through the intracavity medium. On-resonance ($\theta = 0$) this becomes

$$I_t = \frac{T_1 T_2 \alpha}{(1 - 2\sqrt{R_1 R_2} \alpha)^2} I_i. \quad (5.2)$$

Figure 5.2 shows a plot of Eq. 5.2 for a cavity similar to ours with mirror reflectivities of $R_1 = R_2 = 0.999$. The transmitted intensity depends on absorption losses in a highly non-linear way. As a result a detailed comparison of cavity measurements with a standard model for absorption saturation would be somewhat more complicated and less transparent than what is typically seen in the literature. The purpose of performing our absorption saturation measurement though was to demonstrate the strength of the optical nonlinearity in our system, not necessarily to provide a detailed description of the saturation mechanism. For this purpose it was sufficient to simply measure the input power levels at which saturation effects began to take place.

5.3 Experiment Setup

Figure 5.3 provides an overview of the design for the optics and control electronics used in the experiment. The cavity block was cleaned using common UHV techniques and placed into the vacuum chamber. The chamber was pumped with a turbopump down to a pressure of approximately 10^{-6} torr, then filled with approximately 0.1 torr of naturally-occurring xenon and 0.9 torr of helium buffer gas. A frequency-stabilized diode laser (Toptica DL 100 pro design) was tuned to 823 nm, and the output was coupled into an optical fiber and split using a fiber coupler. The additional signal was fed into our precision wavelength meter (HighFinesse WSU30) to continually monitor the laser frequency. The field was then further divided into a high-power and a low-power beam, with the intensity in each arm controlled by in-line fiber optic attenuators. The high-intensity beam was required to saturate the absorption while locking the laser frequency to the cavity transmission peak, since there was very little transmission through the cavity at low intensities when on resonance with the atomic transition. The low intensity beam was then used to perform the actual experiment.

Switching was accomplished using a set of fiber-coupled optical switches, Thorlabs models OSW 12-830-E and OSW 12-780-E. These switches offer a 60 dB rejection ratio with roughly 1.5 dB of insertion loss and switching times on the order of 1 ms. Two photodetectors D1 and D2 monitored the optical intensity in the high power and low power arms before the beam passed through the cavity. A third fiber-coupled switch was used at the cavity output to choose between a fast photoreceiver to measure the high-intensity transmission (D3) and a more sensitive detector to measure the low-intensity signal (D4). A Labview routine running on a laptop computer controlled the laser frequency and the switch states, and oversaw the data collection. The interface between the computer and the laboratory hardware was accomplished using a National Instruments data acquisition mod-

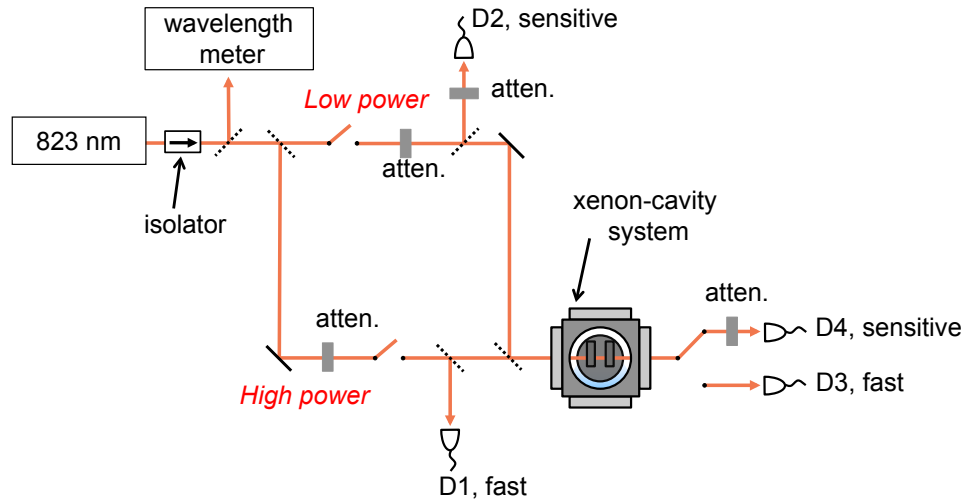


Figure 5.3: Overview of experiment layout to measure absorption saturation in the $6s[3/2]_2^o$ to $6p[3/2]_2$ transition of metastable xenon. Variable attenuators and fiber-coupled switches allowed the system to switch quickly between high-intensity for finding the cavity resonance and low-intensity for probing xenon absorption. The experiment was implemented using mostly fiber-coupled optics. They are illustrated here as bulk components for the sake of clarity.

ule (DAQ), model number USB 6251. The DAQ communicated with the computer via a USB (universal serial bus) connector.

Figure 5.4 illustrates the Labview program used to run the experiment. In hindsight, the program may have been simpler if implemented using another language, for instance Matlab or C++. One source of repeated frustrations was the need for data types and variables to be explicitly defined separately in each subroutine. If for instance we needed to change an array variable by adding one additional element, it was necessary to make the change not only in the main program file but in every connected subroutine as well. As a result, maintaining and modifying the program became quite difficult. Workaround solutions were added to the program one by one, and its complexity gradually increased to the point illustrated in the figure.

Additionally, Labview's documentation is not as easily accessible or as transparent as is the documentation of comparable software packages such as Matlab. National Instruments (NI), the developer of Labview, keeps a repository of example Labview programs as

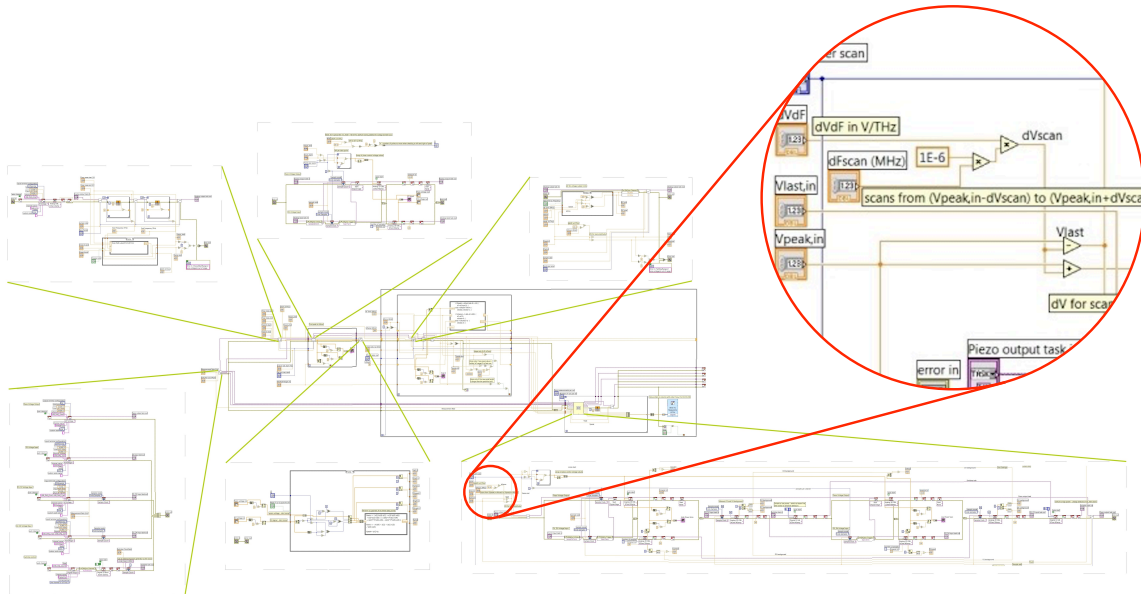


Figure 5.4: Overview of the Labview program used to control the experiment. The main routine is shown at the center of the image, with each of the constituent subroutines expanded around it. Because of the complexity of the system the programming interface became quite cumbersome, as is easily seen here.

an aid in learning the language. So far though we have found these not to be particularly helpful. In our experience they offer easy solutions for specific problems, but without explaining the reasoning behind the design. Hence the program development process for our group consisted in a great deal of trial and error, with various sections of Labview example files cut-and-pasted into our code and crudely stitched together.

National Instruments developed the Labview software and also manufactured our DAQ modules. They designed the Labview software and DAQ hardware to work together, so interfacing our computer with the DAQ was relatively easy. Because programming in Labview can be quite cumbersome though, it may be advantageous for future students to invest some time learning to interface our DAQ's with a different software language. (It may also be the case that, once properly acquainted with the language, programming in Labview is not particularly difficult. The author recognizes that he may well have quite a lot to learn in this subject, and would be happy to receive any relevant advice!)

Locking the laser to the cavity resonance was accomplished by first scanning the laser frequency over a predefined range and finding the point of maximum cavity transmission. If the maximum exceeded a given threshold value the Labview program marked the frequency as the location of the cavity resonance. Hysteresis in the control of the laser frequency made it necessary to then repeat the scan several times, each time reducing the scanning range by roughly a factor of 2. This was done until the program had isolated the resonance frequency to within a window of $10 \sim 20$ MHz.

5.4 Lock-and-Measure Method

In our first attempts at this measurement we followed a 2-step approach, alternatively performing the frequency locking and then making a measurement. First the the switches were set to use the high-power beam path of Figure 5.3 and the cavity transmission peak was located through the procedure described above. The laser frequency was then held fixed at the location of the resonance. Next the program began switching rapidly between the high-power and low-power paths while measuring transmission through the cavity. The high-power beam saturated the xenon atomic transition, hence it experienced negligible absorption within the cavity and could be used as a transmission reference. A normalized measurement of the xenon-cavity transmission was obtained by taking the ratio of the transmission values measured using the high-power versus the low-power beam paths. After taking data for about 300 ms the program switched back to the high-power beam path and re-established the laser frequency lock. The process was repeated until the desired amount of data had been collected.

Figure 5.5 shows a sample oscilloscope trace of the cavity transmission during the measurement segment of the 2-step process just described. On the left side of the image the double peak in the cavity transmission spectrum indicates that the control program had just performed a frequency sweep across the resonance. After determining that the resonance

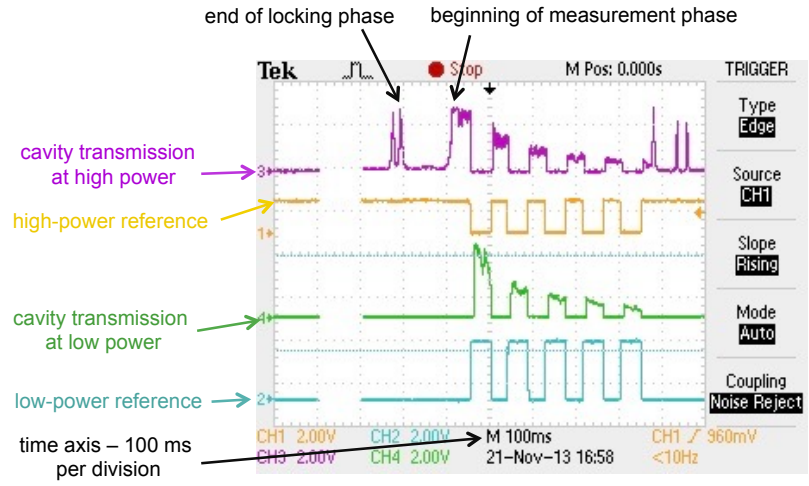


Figure 5.5: Oscilloscope trace of the cavity transmission during the locking and measurement phases of the 2-step lock-and-measure process.

had been located with sufficient accuracy the program switched to the measurement mode. This took roughly 100 ms, as seen in the figure. The alternating rectangular pulses that follow in the high-power and low-power reference channels indicate that during measurement the beam was being switched back-and-forth between high-power and low-power modes, as expected. The switching times were limited by the latency inherent in software-defined control and by the use of a USB computer interface.

While in measurement mode the program was not able to re-lock the laser to the cavity. Over the course of the measurement the laser and cavity frequencies tended to drift. The effects of this on the results shown in Figure 5.5 are pronounced. Within 200 ms of the beginning of the measurement phase the cavity transmission had degraded to roughly $\frac{1}{2}$ of its initial value. This corresponds to a frequency drift of roughly 1 MHz. The drifting was chaotic and unpredictable, and as a result the two-step process was not able to produce reliable measurements of the cavity transmission.

The lock-and-measure process could have been successful if the control software worked on a faster timescale. This may have been possible using a different control architecture. Field-programmable gate arrays (FPGA's) are commonly used for control and

data acquisition in sophisticated quantum optics setups. Experimental operations can be performed on these devices at frequencies on the order of MHz [26, 93, 94]. However, because of our group's limited experience with FPGA's they seemed not to be the best choice. The ready availability and relative ease of use of the NI DAQ made them a more appealing alternative.

5.5 Frequency Sweep Method

Given the limitations of our experiment software interface, we decided to pursue another measurement method that did not require high-speed controls. Rather than measuring transmission with the laser frequency “parked” at the cavity resonance, the new implementation performed measurements by scanning across the full cavity transmission line. The program first completed the frequency locking procedure described in the Section 5.3. After a lock was obtained two more scans were performed, first with the high-intensity beam and then the low-intensity probe beam. A normalized measurement of the cavity transmission was made by taking the ratio of the maximum transmissions measured at the two power levels. We found that the data produced using this method was consistent and repeatable, so we began making measurements of the 823 nm absorption spectrum of intracavity xenon atoms.

To perform the measurements, the Labview control program was executed and the temperature of the cavity was varied to cause the cavity resonance to slowly drift across the metastable xenon absorption spectrum. Because of the frequency locking routine the laser followed the frequency drifting of the cavity. Measurements of the optical frequency and the cavity transmission were acquired continuously throughout the scan.

5.6 Initial Measurements

We began by making a measurement of the transmission spectrum of our xenon-filled cavity, using the frequency sweep method. A sample set of raw data is plotted in Figure 5.6. Part (a) shows the transmission measurements made of the probe beam using detector D3. The 6 absorption dips of Figures 3.6, 3.7, and 4.11 appeared again, as expected, but with significant distortion. The distortion was caused by spurious Fabry-Perot cavities within our fiber-coupled optical system, as discussed in Section 4.4. Part (b) shows transmission measurements of the high-power reference beam using detector D4. The sinusoidal variation of the transmission measured at this detector also indicates the influence of at least one undesired Fabry-Perot in our fiber-optical system. The measurement was taken over the course of roughly 30 minutes. Small variations in ambient conditions caused the FP spectrum to shift over time, evidenced by a partial washing out of the sinusoidal oscillations in several places.

Part (c) of Figure 5.6 shows the result of taking the ratio of the two data sets, D4/D3. The spurious FP effects disappear, and the shape of the absorption spectrum agrees with what we have seen in previous chapters. A significant amount of noise persists though, with the noise amplitude roughly 10% of the signal size. This was probably the result of technical noise, i.e. chaotic variations in the frequency and/or linewidth of our laser system. Locating the maximum transmission of our cavity resonance to within 10% required a laser frequency stability of ± 300 kHz. It is quite possible that our laser was not more stable than this, particularly taking into account the observations described in Section 4.5.2.

It is worthwhile to comment on one more interesting feature in the spectrum of Figure 5.6 (c). Several of the absorption dips in this spectrum show a slight decrease in the apparent optical depth at the very center of the dip, taking on the appearance of a very

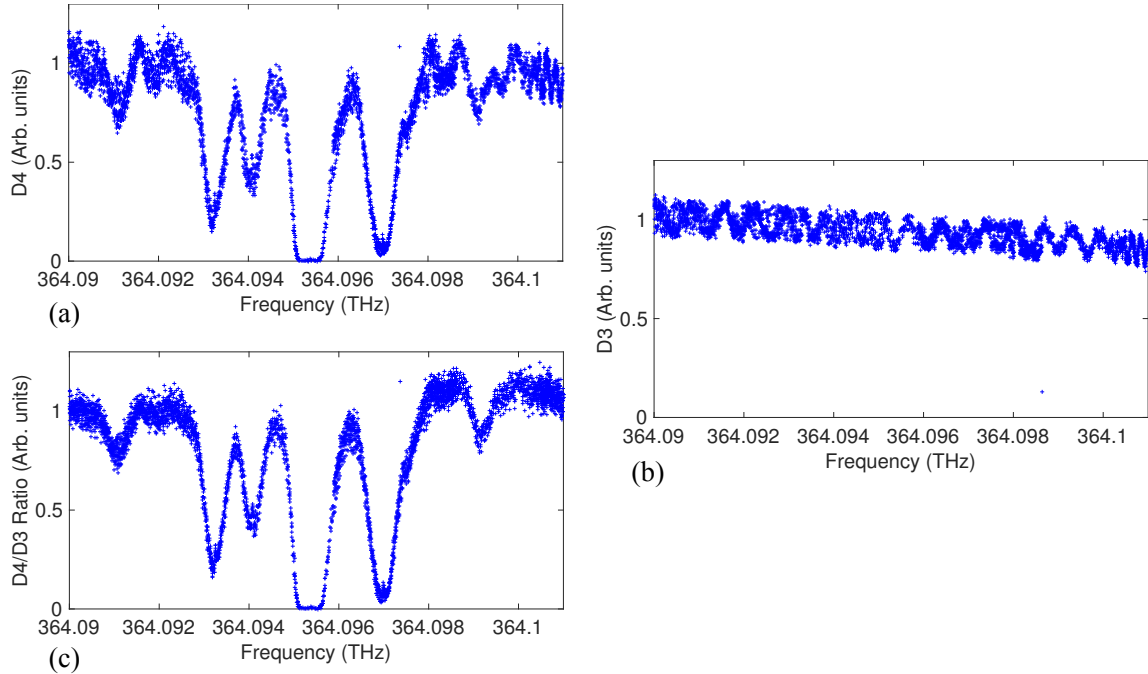


Figure 5.6: Raw data from absorption measurements using intracavity xenon atoms. Given are: (a) measurements of the weak probe beam taken by detector D3, (b) transmission of the high-power reference beam seen by detector D4, and (c) the ratio of two transmission measurements, D4/D3. Oscillations caused by spurious FP's within the fiber-based experiment system are evident in the data of (a) and (b), but largely disappear when the ratio of the two datasets is taken as in (c).

narrow upward-pointing transmission spike. This feature was not present in any of our earlier results taken without the help of the cavity, such as those shown in Figure 4.11.

Consider for a moment one of the absorption dips shown in Figure 5.6 (c), say dip 3. Let's say that a light field detuned from this transition by +100 MHz is traveling from the first to the second cavity mirror. It interacts most strongly with the atomic velocity group that happens to be Doppler shifted by exactly +100 MHz. After reflecting from the second mirror though the Doppler shifts of the atomic velocity groups are reversed, from the field's perspective. Hence the forward- and backward-propagating field components effectively interact with 2 separate atomic ensembles. This is true unless the field is tuned very close to resonance, in which case the forward- and backward-propagating components both interact primarily with atoms that have near-zero longitudinal velocity. Thus an on-resonance field

effectively sees only half as many atoms as does a field that is detuned from resonance, and as a result the on-resonance field finds the intracavity medium slightly easier to saturate. This leads to a small increase in transmission, as was observed. Note that this phenomena is closely related to the Lamb dip commonly used in saturated absorption spectroscopy [95–97]. Obviously the effect observed here only occurs in optical systems with standing wave geometry, such as a that of a Fabry-Perot cavity.

5.7 Results and Discussion

Satisfied that our measurements were sufficiently accurate and consistent, we moved on to measure absorption saturation. To accomplish this we repeated the measurement process outlined in Section 5.5 several times using different probe field intensities. Figure 5.7 shows the experimental results obtained using probe beams with power levels of 0.5, 2 and 19 nW. The data show a significant increase in the relative transmission when the probe power was changed from 0.5 to 2 nW. This change in transmission as a function of input power indicated a nonlinear optical effect taking place. In contrast, if there were no nonlinearity present in this system the three curves represented by the data in Figure 5.7 would lie directly on top of one another.

As a technical aside, we note that the nonlinear effects observed here could have been caused by saturation of the atomic transition, by optical pumping, or by a combination of the two [98]. Optical pumping occurs when the state excited by the probe field decays to one or more energy levels other than the initial state. These additional levels can be different hyperfine components of the initial state, or entirely separate states. For example, a probe field tuned to dip 3 of the 823 nm xenon absorption spectrum at 364.094 THz couples the $F = 7/2$ hyperfine sublevel of $6p[3/2]_2$ in ^{131}Xe with the $F = 7/2$ sublevel of $6s[3/2]_2^{\circ}$ [83]. The level $6p[3/2]_2$, $F = 7/2$ can decay to any of the states $6s[3/2]_2^{\circ}$, $F = 7/2$; $6s[3/2]_2^{\circ}$, $F = 5/2$; or $6s[3/2]_1^{\circ}$, $F = 5/2$. Only population in sublevel $6s[3/2]_2^{\circ}$, $F = 7/2$ however

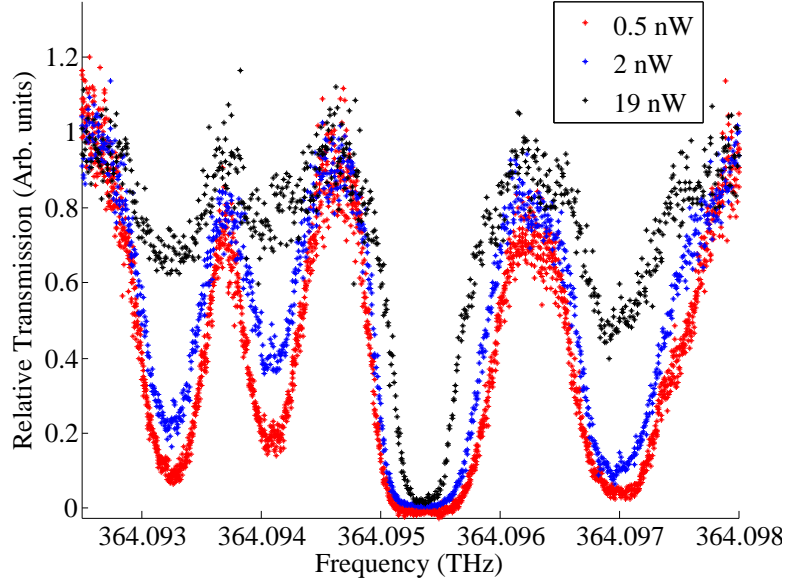


Figure 5.7: Absorption data for intra-cavity metastable xenon with input power levels of 0.5, 2, and 19 nW. From the 2 nW to the 19 nW levels the absorption was dramatically reduced, indicating a saturation nonlinearity. Most of the signal noise was caused by Fabry Perot-type interference effects along the beam path and will be suppressed in future experiments. [figure taken from reference [34]]

contributes to absorption of the probe field, since the other levels are far detuned. Hence a decay to either of states $6s[3/2]_2^o, F = 5/2$ or $6s[3/2]_1^o, F = 5/2$ results in a decrease in the optical depth of the Xe^* atoms. The effects of this phenomenon increase with the length of time that atoms are allowed to interact with the probe, and with the intensity of the probe field. A more detailed discussion of the interplay between optical pumping and atomic saturation can be found in references [68] and [71].

Because of the narrow beam width of the field in our cavity ($\sim 120 \mu\text{m}$), atoms traveling at typical thermal speeds passed through the field mode in only a few 100's of ns. As a result the effects of optical pumping were significantly smaller than they would have been for a wider-diameter beam. Rough calculations indicated that optical pumping and atomic saturation effects should begin to occur in our cavity at roughly the same power levels. Thus the saturation effects evident in Figure 5.7 were likely caused by a combination of these two mechanisms working together.

5.8 Conclusions

The increase in transmission with increasing input power shown in Figure 5.7 indicates saturation effects occurring at nanowatt power levels. If a similar experiment had been performed without the help of a cavity, nonlinear effects should not have been observed until probe power levels reached orders of μW . This indicates that the use of our cavity, with a finesse of 3,000, resulted in an enhancement of the nonlinearity of Xe atoms by roughly 3 orders of magnitude.

Saturation effects occurring at these low power levels indicate the high nonlinearities possible with our xenon-cavity system [34]. Also the relative simplicity of this experiment using atomic vapor is an advantage compared with the complexity of other, trap-based approaches for producing strong optical nonlinearities [99–103]. This work helped us to convince ourselves of the feasibility and the practical advantages of doing nonlinear optics with xenon gas in a cavity. Having accomplished this, the natural next step for our project was the measurement of cross-phase modulation in the cavity. This would provide a more direct means of comparing our cavity's performance with that of other sophisticated cavity QED systems. It would also demonstrate the degree of improvement required for a similar cavity to be able to produce sizable single-photon cross-phase shifts.

Chapter 6

Ultra-Low Power Cross-Phase Modulation

6.1 Overview

We have demonstrated the ability of our xenon-cavity system to produce nonlinear optical effects with ultra-low input power levels. In this context absorption saturation is an interesting effect from a scientific perspective, but many practical applications depend on other nonlinear processes such as cross-phase modulation. Single-photon cross-phase shifts, in particular, have a wide range of applications in quantum optics and quantum information processing [8, 9, 30, 104, 105]. The finesse of our proof-of-principle cavity was not high enough to produce cross-phase shifts at the single-photon level, but the demonstration of cross-phase modulation in using macroscopic fields still constituted a significant step toward this goal.

Here we review our experimental demonstration of cross-phase modulation using our xenon-cavity system. As with Chapter 5 some of the work described in this chapter

has been previously published [35], though we have taken the liberty of including many additional experimental and theoretical details.

6.2 Cross-Phase Modulation with Xenon

Producing a cross-phase shift requires a system with two separate field frequencies. One field is typically chosen to be the control while the other is used as a probe. There are several ways in which an atomic medium can provide the nonlinear mechanism in such an interaction. A two-level diagram such as the one used in the experiments of the previous chapter, and shown in Figure 3.6, could accomplish this [38]. This setup has the disadvantage though that the control and probe fields must be very close together in frequency, making it difficult to distinguish between them at the detection side of an experiment. Additionally, the probe field in such a configuration interacts with the atomic medium even when the control is absent, and as a result it suffers absorption losses. These difficulties can be overcome by using a 3-level diagram.

Figure 6.1 shows the energy level diagram used in our cross-phase shift experiment. The probe in this diagram is tuned near the 853 nm $6p[3/2]_2$ to $8s[3/2]_1^o$ transition. This is very far detuned from the lower transition $6s[3/2]_2^o$ to $6p[3/2]_2$, so this transition does not lead directly to absorption of the probe. In the absence of a control field the probe passes straight through the xenon gas without being noticeably affected. If however the 823 nm control field is turned on and tuned close to the lower transition, the state $6p[3/2]_2$ accumulates population. This population is free to interact with the probe through the transition from $6p[3/2]_2$ to $8s[3/2]_1^o$. If the detunings are chosen properly the presence of the control field produces a cross-phase shift on the probe. For convenience we label the atomic states $|1\rangle$, $|2\rangle$, and $|3\rangle$ in order of increasing energy, as shown in the figure.

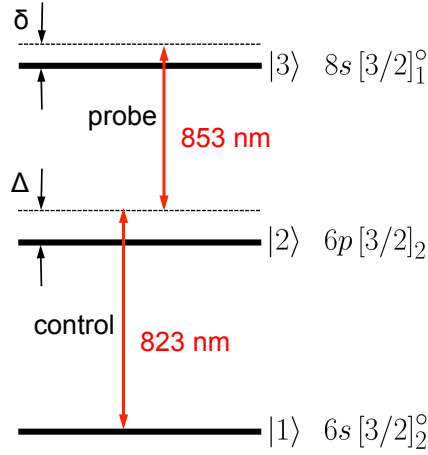


Figure 6.1: Energy level diagram used for producing cross-phase shifts with metastable xenon gas in a cavity. A 3-level system allows the 823 nm control and 853 nm probe fields to be widely separated in frequency. The probe field in this configuration does not suffer from absorption, except for a small amount of 2-photon absorption that occurs in the presence of the control.

Use of the 3-level diagram of Figure 6.1 has the additional advantage that the two wavelengths are relatively close together. As a result, when the 823 nm and 853 nm fields counterpropagate through the atomic medium the 2-photon transition is essentially unaffected by Doppler broadening. The Doppler width of the $|1\rangle$ to $|2\rangle$ transition is roughly 440 MHz. In contrast, the effective Doppler width of the $|1\rangle$ to $|3\rangle$ transition in the counter-propagating configuration is only ~ 16 MHz, due to the 3.6% difference between the two wavelengths.

Within the standing-wave geometry of a Fabry-Perot cavity the two fields effectively spend half of their time copropagating and half counterpropagating. For cases in which the fields copropagate, Doppler broadening washes out the 2-photon transition and essentially nothing happens. Thus the results when using a standing-wave field geometry are nearly identical to those of an experiment with counter-propagating fields, but that the nonlinear interaction occurs at one-half the rate [35].

The strength of the nonlinearity in this system depends on the rates at which the two transitions occur. These rates are governed by the dipole matrix elements μ_{21} and μ_{32} for the

transitions $|1\rangle$ to $|2\rangle$ and $|2\rangle$ to $|3\rangle$, respectively [106]. We calculated the transition dipole moments using lifetimes and branching ratios taken from [78], aided by the results of some two-photon absorption measurements performed in our lab. We found $\mu_{21} = 7.6 \times 10^{-30}$ Coulomb-meters (Cm) and $\mu_{32} = 1.2 \times 10^{-30}$ Cm. For a point of comparison, these dipole moments are of roughly the same size as those of commonly used transitions in Rb.

6.3 Design of the Experiment

The measurement of a phase shift is in general somewhat more difficult than that of an absorption rate. Standard photodetectors see only the time-averaged intensity of an incident light field, so phase information must be gleaned through interferometry. Additionally, because applications of cross-phase modulation typically depend on operation in a pulsed rather than in the continuous-wave (CW) regime, we wanted to implement the phase-shift measurement using pulses. The sensitive timing control necessary for this placed additional demands on the experiment.

As our system was to be built using fiber-coupled components, when designing our interferometer we needed to take into account the small changes in refractive index that occur in optical fiber. As mentioned in Section 4.4, it is possible to compensate for these index variations with active phase correction. We however chose to circumvent the problem by using a Sagnac interferometer.

Figure 6.2 illustrates the design of the system used for this experiment. Optical pulses from the control and probe lasers were combined and sent into a Sagnac interferometer containing the cavity. Upon striking the beam splitter at the Sagnac loop input, each control and probe pulse was split into two counterpropagating pulses. The loop geometry and pulse timings were then adjusted such that only one of the two counterpropagating probe pulses received a cross-phase shift in the cavity.

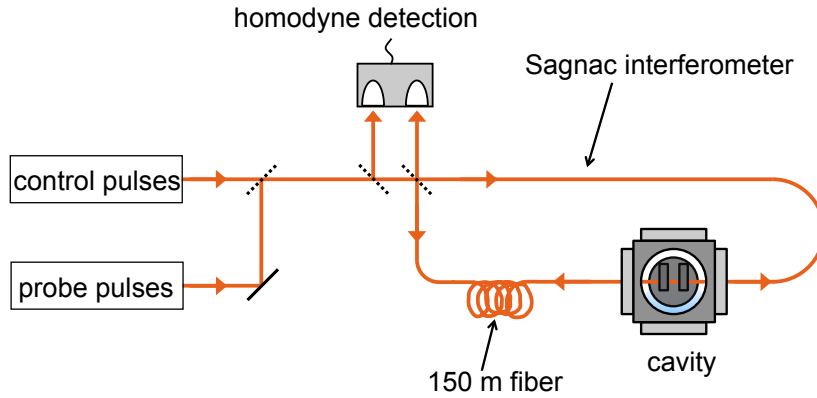


Figure 6.2: Conceptual diagram of the system for measuring the cross-phase shift. Homodyne detection was used to measure interference between two probe pulses counterpropagating within a Sagnac loop. An extra 150 m fiber delay line was used to separate the two pulses of each pair. The timing between control and probe fields was carefully chosen so that only one of the counterpropagating probe pulses received a cross-phase shift in the cavity.

This was accomplished by inserting an extra 150 m of optical fiber into the loop. A light pulse takes about 700 ns to travel through this length of fiber. The counterclockwise-propagating control pulses were timed to reach the cavity at the same time as the clockwise-propagating probe pulses, resulting in a phase shift. The counterclockwise-propagating probe pulses, on the other hand, passed through the cavity 700 ns later and were not phase shifted. These latter probe pulses functioned as a local oscillator. Interference between the probe and local oscillator pulses was then measured using homodyne detection at the interferometer output ports, as shown in the figure.

The experiment was built using optical fiber and fiber-coupled components. Two tunable diode lasers (Toptica DL pro) were tuned to 823 and 853 nm to produce the control and probe beams, respectively. Each laser field passed through an EOSpace GHz fiber-coupled amplitude modulator, which was used to cut the beam into pulses with durations of 30 ~ 60 ns. The Sagnac loop was made with polarization-maintaining (PM) single-mode fiber, to more easily maintain the polarization of the fields interacting with Xe atoms in the cavity. A time-dependent phase modulator, also from EOSpace, was placed in the Sagnac loop as well. This was used to impart a 90° shift on one but not both of the counterpropagat-

ing pulses, maximizing the sensitivity of the output interference pattern to any additional small relative phase shifts. With the inclusion of this extra time-dependent phase, the signal received at the balanced detector was directly proportional to the measured phase shift. Our balanced detector was a Thorlabs model PDB420A, with a bandwidth of 75 MHz.

Figure 6.3 shows an oscilloscope trace of some calibration measurements made using the setup we just described. Probe pulses were sent into the Sagnac loop containing the cavity with a repetition rate of 200 kHz, and an oscilloscope with a 10 Gs/s sampling rate was used to monitor the balanced detector output. The scope images shown in the figure were produced after accumulating data from more than one thousand repetitions of the experiment. Noise in the signals is represented by the thickness of the scope traces. The top trace in the figure shows the output of the balanced detector. The trace below that shows the electrical signal sent to the amplitude modulators for switching the probe field on and off. No phase shifts were produced during this test run, but interference between pulses transmitted through the cavity and back-reflections within the system produced a small signal at the balanced detector. Since the cavity was located far away from the center of the Sagnac loop, back-reflections from the two sides of the cavity also produced small detector signals, but at different times. The x-axis in the figure spans a time interval of 5 μs .

6.4 Optical Amplifiers to Improve SNR

The signal to noise ratio (SNR) for measuring mrad phase shifts with the simple measurement system described above was quite poor, roughly on the order of 10^{-3} . A practical implementation of the experiment needed some means to effectively amplify the signal received at the balanced receiver.

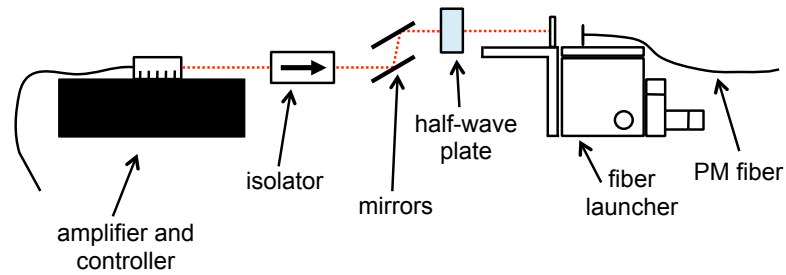


Figure 6.4: Diagram of the optics used to couple light from a Thorlabs tapered amplifier into single-mode polarization-maintaining (PM) optical fiber.

This proved to be technically challenging. The amplifier emission was produced in a free space mode with a highly non-Gaussian profile, so efficiently coupling the field into fiber was quite difficult. The mode profile also varied as a function of distance away from the amplifier output facet, and as a result the best possible coupling into single-mode fiber was possible only with the fiber placed roughly 20 cm away. Free-space isolators needed to be placed immediately after the amplifier output facets to prevent damage from back-reflections. A half-wave plate was also required for each amplifier, to ensure proper polarization of the output. Finding an effective way to fit the necessary isolators, waveplates, and alignment mirrors within a 20 cm length limit was challenging. Figure 6.4 illustrates the setup that was finally successful. Figure 6.5 provides a photo of the physical setup in the laboratory.

Figure 6.6 shows a series of images taken of an amplifier’s transverse mode profile at various distances from the output facet. We had removed the plastic housing and the focusing optics from a commercially available webcam, and we used the leftover ccd array to take the images (thanks to Todd Pittman for devising this apparatus). The photos were taken using a very weak seed beam so as to avoid damaging the detector. At a distance of roughly 20 ~ 30 cm this resulted in relatively efficient coupling to single-mode fiber. The efficiency achieved in our setup was 32%, resulting in slightly more than 300 mW of optical power coupled into in the fiber. Without the amplifiers the maximum available power was about 1 mW.

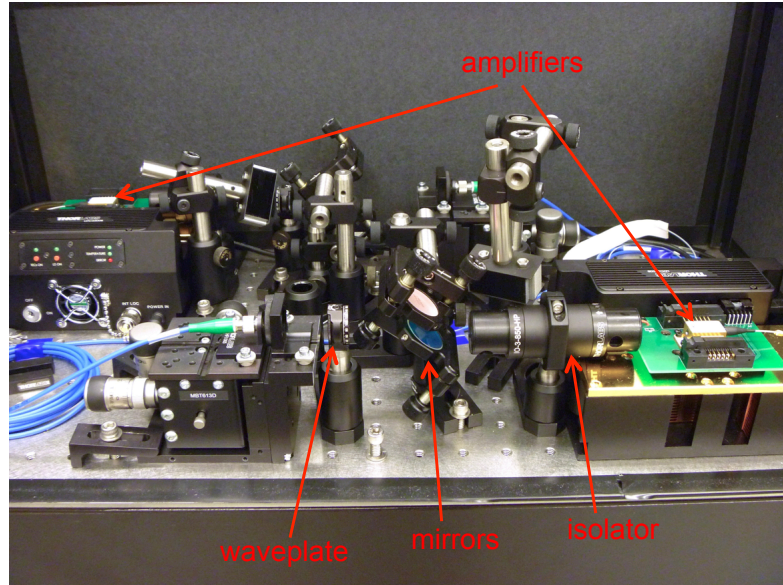


Figure 6.5: Laboratory photo of the optics used to couple light from a Thorlabs tapered amplifier into PM fiber.

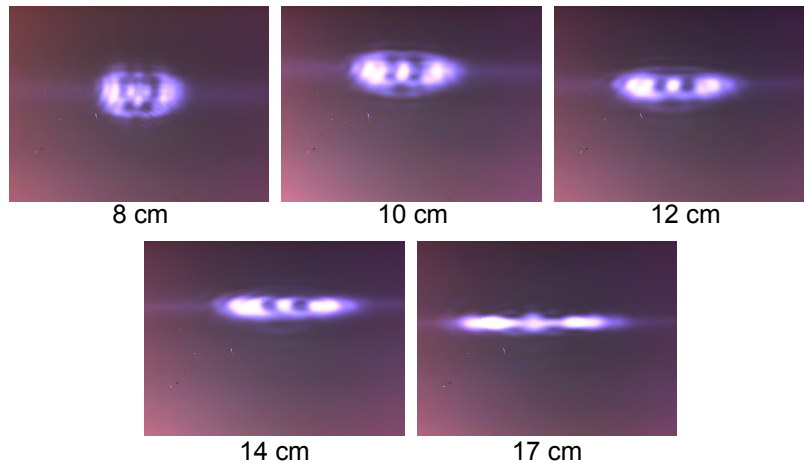


Figure 6.6: CCD images of the mode profile of an amplifier's emission, taken at various distances from the output facet. A very weak pump was used to seed the amplifier for these images, to avoid damaging the detector.

After adding the amplifiers to our setup we needed to attenuate the clockwise-propagating probe pulses, to prevent them from saturating the cross-phase shift. This was done by placing an optical isolator in the Sagnac loop. The clockwise-propagating probe passed through the isolator in the reverse direction and was attenuated by 30 dB, while the counterclockwise propagating local oscillator was not attenuated. Also the inclusion

of the isolator eliminated one out of the two cavity back-reflected pulses typically seen in experiment trials. Compare for example the measurements of Figure 6.3 above (taken without an isolator) with those of Figure 6.7 or Figure 6.8 below (for which the isolator was used).

6.5 Noise from Back-Reflections

The addition of optical amplifiers into our fiber-based system led to a wide variety of technical problems. The amplitude modulators used to create our optical pulses were susceptible to damage if used with optical power levels above 5 mW. Clearly it would not have been suitable to use them to modulate the 300 mW field produced at the amplifiers. Initially we tried using these modulators to control the amplifier seed beam only, hoping that if the seed field were pulsed, the amplifier output would follow the same temporal shape.

Figure 6.7 illustrates the performance of our measurement system under these conditions. Part (a) of the figure shows a conceptual diagram illustrating the laboratory layout. Part (b) shows the behavior of the measured homodyne signal when amplitude modulators were used to switch the field seeding the amplifiers. Use of the amplifiers greatly improved the measurement signal strength, but introduced a great deal of noise as well. The problem of this setup was that it allowed amplified spontaneous emission (ASE) to couple into our optical system. Back-reflections within the fiber optical beam path then caused the ASE to overlap with and obscure our measurement pulses.

Figure 6.8 (a) shows our solution to this problem. In addition to the amplitude modulators switching the amplifiers' seed field, we included a Pockels cell after the amplifiers. This allowed us to switch the amplifier output on and off with an extinction ratio of roughly 20 dB. With this addition the ASE noise was reduced to an acceptable level, as can be seen in the oscilloscope trace in part (b) of the figure.

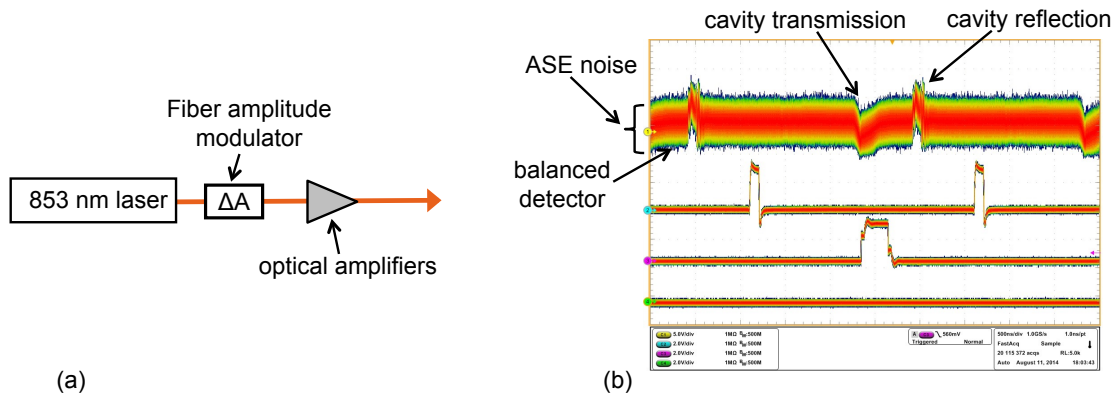


Figure 6.7: (a) Illustration of the optics used in the laboratory to produce the probe field pulses. An amplitude modulator was used to switch the seed laser on and off. (b) Oscilloscope trace of the balanced detector reading for this system. The output of the balanced detector is shown in the top trace. The remaining traces may be ignored. Compared with the results shown in Figure 6.3 the addition of the amplifiers here produced a larger signal, but also a great deal more noise. The noise was caused by amplified spontaneous emission (ASE) from the amplifiers.

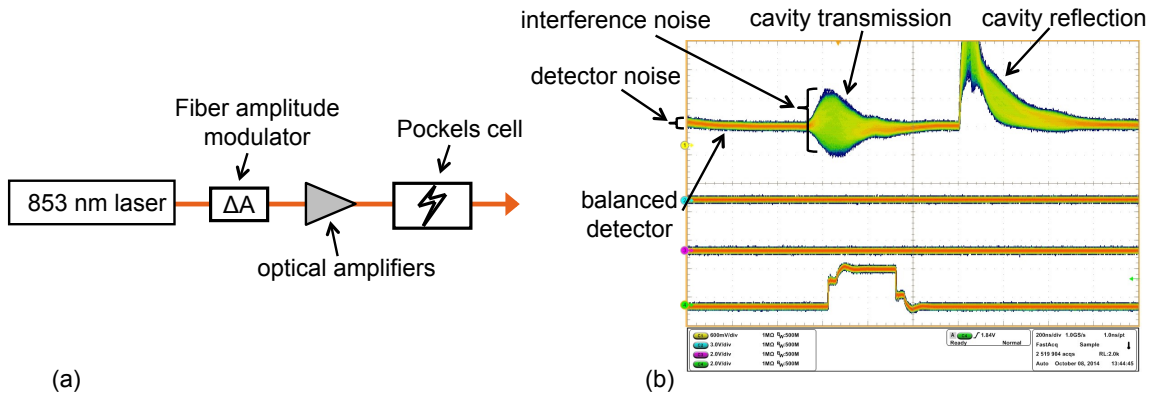


Figure 6.8: (a) Illustration of the updated optics for producing the probe field pulses. An amplitude modulator was used to switch the seed laser on and off, and a Pockels cell was used to switch the amplifier output. (b) Oscilloscope trace of the balanced detector reading during a test of this system, where the output of the balanced detector is shown in the top trace. The ASE noise evident in Figure 6.7 had been removed. During detection of the cavity transmitted pulses though, a large amount of noise remained.

Soon though we discovered that ASE was not the only prominent noise source. The Pockels cell seemed to be leaking a small amount of narrowband light as well. Because of interference with strong local oscillator pulses a very small leakage of narrowband light at the probe frequency produced a great deal of noise. This can be seen in Figure 6.8 (b). As one would expect, the noise amplitude was largest at the points of overlap with the cavity

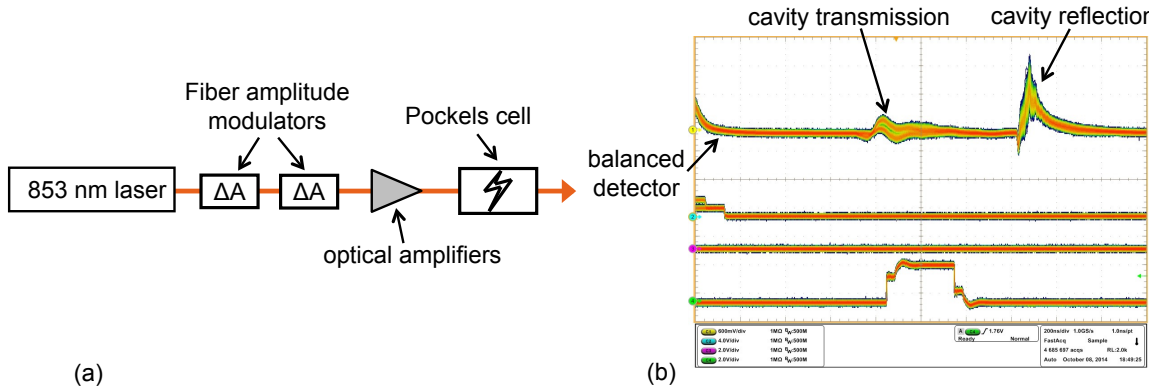


Figure 6.9: (a) Optics used to produce the probe field pulses with minimized leakage of narrowband probe light. The addition of an extra amplitude modulator in front of the amplifiers limited the leakage. (b) Oscilloscope traces of the balanced detector reading during a system test run. The output of the balanced detector is shown in the top trace. Noises were small enough that phase shift measurements were possible.

transmission and reflection pulses. The amplifiers produced this narrowband emission even when the amplitude modulator shown in Figure 6.8 (a) was used to shut off the seed laser. The amplitude modulator’s extinction ratio was roughly 30 dB.

Figure 6.9 illustrates our final solution. Using two fiber-coupled modulators in series reduced the narrowband leakage rate and removed the interference noise. Part (b) of the figure shows an oscilloscope trace obtained during a trial run of this system with the control field turned off. These trial runs were accomplished in two-step iterations. During the first step a normal phase-shift measurement was performed. In the second step the measurement was repeated, but with the time-dependent phase modulator applying an extra 90° phase shift. The two separate measurement results are clearly distinguishable in the cavity transmission signal in Figure 6.9 (b). Test runs such as this were used to calibrate the homodyne detector’s sensitivity to a given phase shift.

However, the oscillating shape of the cavity transmission signal in Figure 6.9 indicated that some interference noise was still present. This interference was probably caused by very weak back-reflections within our fiber-coupled optical system, and it seemed to be unavoidable. Fortunately the characteristic timescale for variations in the amplitude of this

noise was on the order of seconds. To remove the noise our phase shift measurements were performed using a two-step method. First a normal cross-phase shift measurement was performed, then the measurement was repeated several microseconds later but with the control field turned off. The balanced detector signals obtained in these two runs were subtracted to remove the noise.

After the additions and modifications described in this section, our experimental system was ready to take measurements. Before moving to discuss the process of performing the experiment, in the next section we briefly mention a few remaining details of our laboratory setup and the computer control system.

6.6 Laboratory Setup

Figure 6.10 provides a detailed diagram of the laboratory layout for our experiment. After passing through the amplitude modulators used to produce nanosecond pulses, each laser field was fed to a pair of photodetectors, labeled D1 and D2 in the figure, to monitor the beam intensities and to ensure proper biasing of the modulators. The frequencies of both fields were also continuously monitored using our high-precision wavelength meter. To facilitate high-speed frequency locking of the lasers, two high-bandwidth photodetectors D3 and D4 measured the transmission of the beams through the cavity. Relatively high intensities of the two beams were required in order to produce a sufficiently large signal at the detectors. To accomplish this, the control beam was divided into two separate paths using a set of fiber-coupled optical switches (Thorlabs OSW12-830E and OSW12-780E), as was done previously in our measurement of absorption saturation. A variable attenuator was added to one of the paths for the low-intensity measurements, while the higher intensity in the other path was used to periodically lock the laser frequency to the cavity.

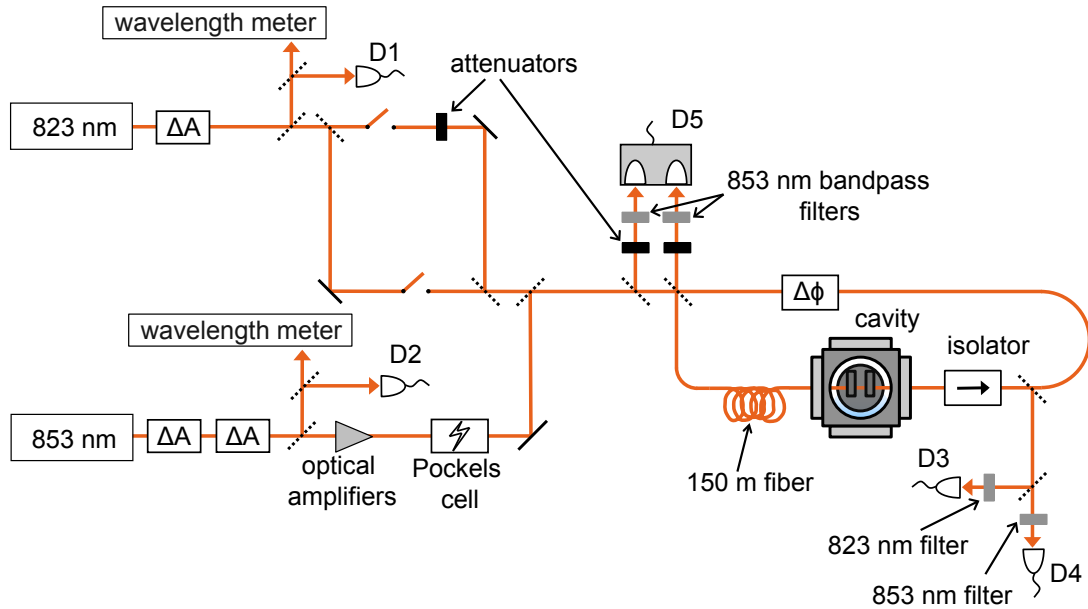


Figure 6.10: Diagram of experiment layout for the cross-phase shift measurement. The setup followed the basic operating principle illustrated in Figure 6.2, but with additional components included to accomplish frequency locking and to improve the signal-to-noise ratio. Note that while the system is illustrated with bulk free-space components for simplicity, most of the experiment was implemented within optical fiber.

Noise from the back-reflection signals evident in part (b) of Figures 6.7, 6.8, and 6.9 was eliminated through the use of a nanosecond analog-to-digital converter (FAST ComTec 7072) in combination with our fast balanced photoreceiver. These allowed the system to sample the cross-phase shift signal while ignoring the reflected pulses. The data collection system operated at a repetition rate of 200 kHz using high-speed nuclear instrumentation module (NIM)-bin electronics. An average over approximately 10^5 such measurements was used to estimate the cross-phase shift due to the presence of the control beam.

As described in Section 5.3, a Labview program on a laptop computer controlled the laser frequencies and data acquisition. Two National Instruments DAQ's, models USB 6251 and USB 6363, communicated with the laptop through a USB connector to interface the laboratory equipment with the computer. The cavity's temperature and resonance fre-

quency were controlled separately with an external heater and a variable voltage source, as discussed in Section 4.5.1.

The control system used an analog of the “lock-and-measure” method described in Section 5.4. The system first located two cavity resonances close to the control and probe field frequencies, and matched the laser frequencies to them. Then the lasers were held fixed at those frequencies while the measurement was performed. This method failed to produce consistent results in Section 5.4 because of the slow response time of our software-defined control routine, and the relatively fast rate of laser frequency drifting. The laser frequency tended to drift at rates of roughly ~ 1 MHz/s, and coupling to the cavity degraded quickly in that experiment because of the narrow cavity linewidth of 1.5 MHz. The phase shift measurements we are describing here though were implemented using optical pulses of 30 \sim 60 ns. The linewidths of these pulses was on the order of 15 MHz, so the cavity coupling efficiency was much less sensitive to small ~ 1 MHz frequency drifts. We found that it was quite possible to maintain consistent coupling efficiency throughout the experiment, as long as the rate of change of the cavity resonance frequency due to temperature variations was kept below ~ 1 MHz/s.

6.7 Frequency Tuning

The measurement required careful control of the detunings between cavity and atomic resonances. Achieving this was quite difficult, as the experiment required that one cavity resonance to be located close to each of the $|1\rangle$ to $|2\rangle$ and $|2\rangle$ to $|3\rangle$ transition frequencies at the same time. A good cavity frequency control system for this experiment should have two degrees of freedom to separately control the two resonance frequencies. Tuning of the cavity’s temperature though provided us with only one degree of freedom.

The difficulty of independently controlling the two cavity resonance frequencies can be more easily described with a change of variables. Using f_c and f_p for the frequencies of the control and probe field modes, respectively, we let $x \equiv f_c + f_p$ and $y \equiv f_c - f_p$. The coefficient of thermal expansion of nickel is roughly $\alpha_L = 13 \cdot 10^{-6} 1/^\circ\text{C}$. Thus an increase dT in the block's temperature led to a proportionate increase in the cavity length, $dL = \alpha_L L dT$. For an 823 nm control field it takes roughly $n_c \approx 30,400$ wavelengths to span the length of a 2.5 cm cavity. If the cavity length were to increase by dL , the wavelength of the field would need to increase by $d\lambda_c = dL/n_c$ in order to maintain resonance. Thus the frequency of the 823 field would be forced to change by $df_c = -\frac{2\pi c}{\lambda_c^2 n_c} dL$. The case was similar for the 853 nm probe. The result was that a cavity temperature change of dT produced a shift in x of $dx = (-9.3 \text{ GHz}/^\circ\text{C}) dT$. Because of the slight wavelength difference between our control and probe fields changing the cavity temperature also produced a small shift in y , $dy = (-160 \text{ MHz}/^\circ\text{C}) dT$.

Independent, simultaneous control of the two detunings x and y was accomplished in the following way. First the cavity temperature was tuned to place x near the desired value. The value of y was then checked. Typically y would be found to be ~ 1000 MHz or more away from the desired value. Next the cavity temperature was changed by ΔT such as to increase (decrease) x by exactly 12 GHz. This resulted in a change in y of magnitude roughly 210 MHz, with the same sign as the change in x . The 823 and 853 nm lasers were then each tuned 6 GHz lower (higher) to match cavity resonances one free spectral range away. The net result of this process was that x was left unaltered while y was changed by ± 210 MHz.

By repeated application of this procedure y could be scanned to within ~ 210 MHz of any desired value. The primary source of difficulty in the laboratory was the time required to complete the operation. Figure 6.11 shows the response of a cavity resonance frequency after a delta function pulse was applied to the heaters. The response time of this system to thermal inputs from the heaters was on the order of 30 minutes. To avoid

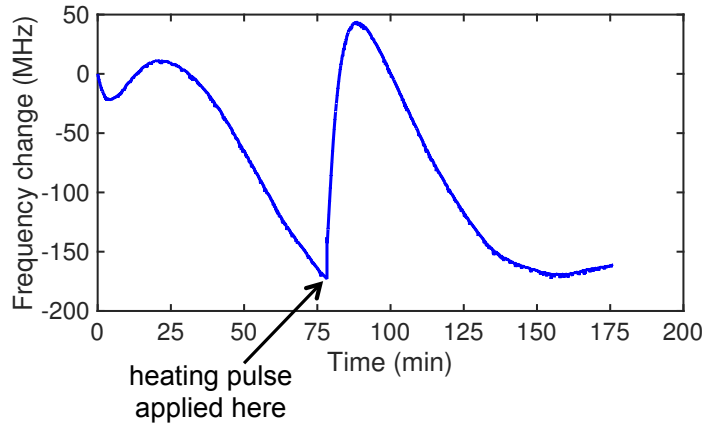


Figure 6.11: Plot of the frequency drift of a cavity resonance after receiving a delta function heating pulse. The cavity recovered from the effects of the pulse after roughly one hour.

overshooting it was typically necessary to perform a given tuning control task in iterative steps separated by intervals of 30 ~ 60 minutes. Thus the initial temperature tuning at the beginning of a day of data taking often required multiple hours.

The task of frequency tuning was further complicated by the presence of an RF discharge in the vacuum chamber during experiment runs. The plasma discharge was often more effective at changing the cavity temperature than our heaters were. To compensate, when the experiment was not running we used the heaters to stabilize our cavity at a relatively high temperature of near 60 ~ 80 °C. Before beginning an experiment the detunings were adjusted using the procedure outlined above, and then the heater power was reduced by 2 ~ 4 watts. After ~ 10 minutes the cavity temperature would begin to fall. The RF discharge was then applied, and its power was adjusted to stabilize the cavity temperature and restore the frequency detunings. Hysteresis and a high degree of nonlinearity in the response of the discharge to a change in the input RF power level made this process quite difficult. Additionally, the lock-and-measure control method required that the drifting rate of the cavity resonance frequency be kept below $\sim \pm 1$ MHz/s during the measurement. It was often necessary to make iterative adjustments to the RF discharge and heater power levels to achieve the desired detuning values, discharge intensity, and temperature stability.

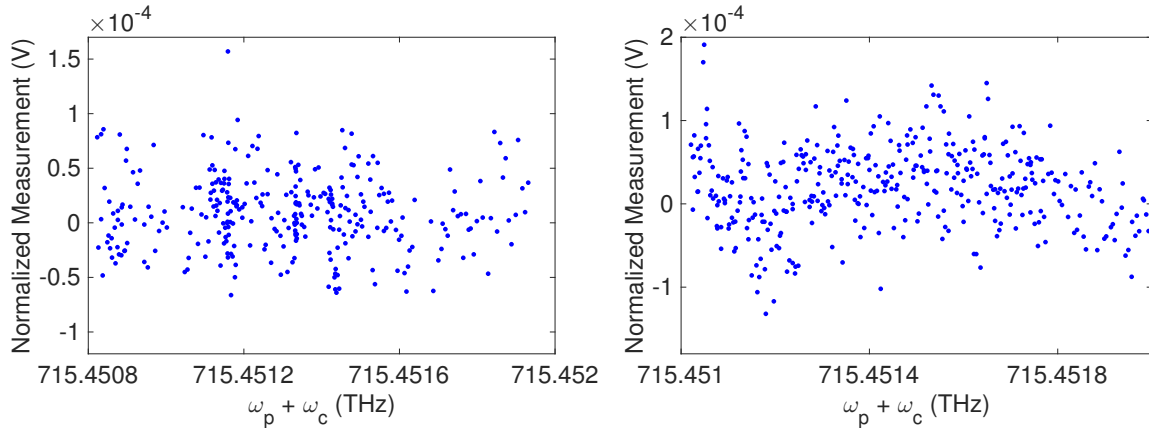


Figure 6.12: Data from our initial phase shift measurements. There is no evidence in this data of a cross-phase shift signal. The chaotic variations evident in the data were probably caused by small, spurious back-reflections within our fiber-coupled optics.

With roughly 15 ~ 30 minutes required for each iteration, the initial tuning process often required half of a day or more of work.

A tuning control system that required this much setup time was not ideal, but it did accomplish its task. Before long we were ready to take our first phase shift measurements.

6.8 Searching for the Signal

Figure 6.12 shows some of the data acquired during our first 1 ~ 2 weeks of making measurements. The data shown in the figure exhibits some interesting, chaotic behavior. One particularly optimistic, and perhaps relatively naive, member of our group (not to mention any names!) initially hoped that the fluctuations in this and similar data sets might contain indications of a phase shift signal. Eventually though we were forced to conclude that this behavior was caused by residual back-reflections in our fiber optics. These back-reflections produced slowly-varying noise, with changes occurring in time scales on the order of seconds or minutes. As a result these spurious signals occasionally resembled genuine measurement results.

With some slight disappointment we decided to take one step back from measuring phase shifts, and to examine more carefully the spectroscopic properties of our metastable xenon atoms. The frequency of the 853 nm transition illustrated in Figure 6.1 is documented in the literature [78], but only with precision of roughly ± 2 GHz. To the best of our knowledge, the hyperfine structure of this transition was previously not well documented. We decided to take some time away from the phase shift experiment so as to search for and study this transition by making two-photon absorption measurements of metastable Xe in free-space. The measurement apparatus would be comparatively simple, and the results would help us a great deal in finding the phase shift signals we had been looking for.

Figure 6.13 illustrates the experimental setup used for these measurements. Our 823 and 853 nm lasers were coaligned using SM fiber and sent through the vacuum chamber. The fields were set up in a counterpropagating configuration to mitigate the effects of Doppler broadening on the two-photon absorption spectrum. We did not use the cavity for these measurements. We modulated the amplitude of the 823 nm control field at a rate of roughly 25 kHz using an EOSpace modulator, and used a lock-in amplifier to monitor the transmission of the the 853 nm probe. The use of the lock-in amplifier allowed this system to measure absorption losses of less than 0.01% with very high SNR. To perform the measurements, first the control field was tuned close to one of the six 823 nm xenon absorption dips. The 853 nm probe frequency was then swept over several GHz across the frequency range where two-photon absorption was expected to occur. Tuning the control field to a different absorption dip resulted in coupling between a different set of hyperfine components, which then produced a different two-photon absorption spectrum. We measured this spectrum using several of the 823 nm xenon absorption dips and several values of the control field detuning.

Figure 6.14 shows two samples of measured two-photon absorption spectra. Because of the use of counterpropagating control and probe fields the two-photon spectrum was essentially Doppler-free. This is evident in the narrower widths of the absorption dips

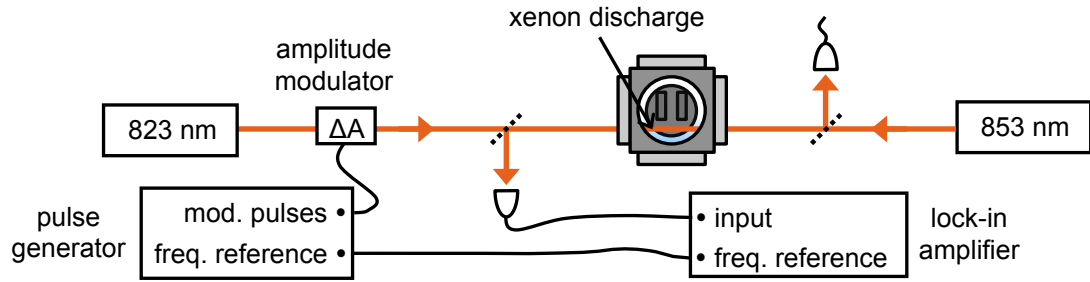


Figure 6.13: Experiment setup for two-photon absorption measurements. Counterpropagating 823 and 853 nm fields passed through the xenon RF discharge inside our vacuum chamber. The fields passed straight through the chamber without coupling into the cavity.

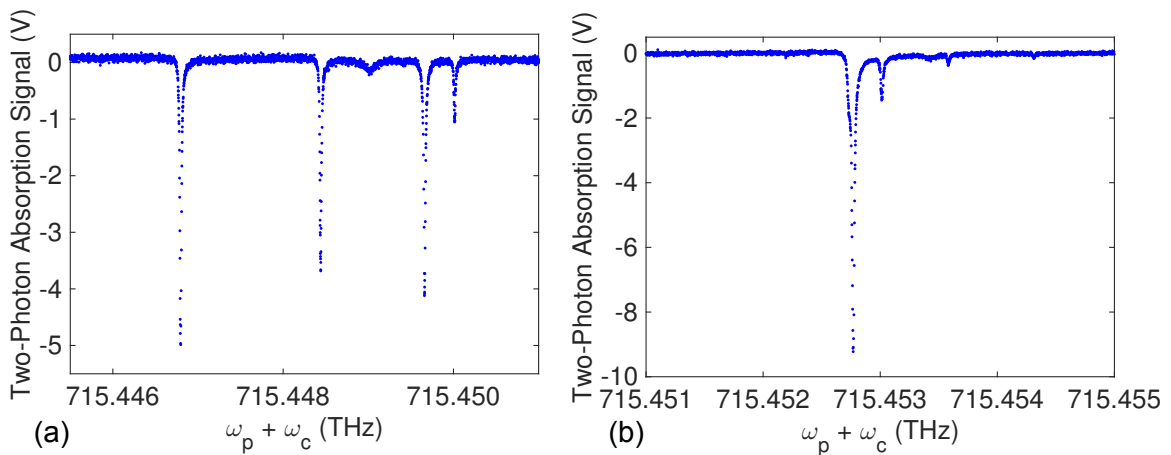


Figure 6.14: A sample of our two-photon absorption measurement results. Measurements were taken with the 823 field tuned to (a) dip 2 and (b) dip 5.

in the figure, compared for example with those of the single beam measurements recorded in Figure 5.7. This data provided us with precise measurements of the frequencies and the relative transition rates for the various hyperfine components of the xenon $|2\rangle$ to $|3\rangle$ transition. The results informed us as to the precise combinations of control and probe field frequencies at which cross-phase modulation would occur, and they allowed us to determine which hyperfine components would produce the strongest phase shifts.

Finding the best candidate hyperfine component was not quite as simple though as simply choosing the one for which the two-photon absorption rate was strongest. It was important to avoid cases which would allow competition between two or more components.

For example, it initially seemed like a good idea to tune the control field near dip 4 of the 823 nm xenon absorption spectrum (see Figure 3.6) because of the strong absorption there. However, Figure 3.7 indicates that this dip was composed not of a single transition but of many different hyperfine components packed closely together. A control field tuned near dip 4 would couple to all of these components simultaneously. It was not possible for more than one component to contribute to cross-phase modulation at any given time. Coupling the control field to many hyperfine components at once would simply result in higher optical losses, and would reduce the measured phase shift.

Given these considerations, the best hyperfine components for producing phase shifts were those arising from dips 1 and 6 of the 823 nm spectrum (refer to Figure 3.6). These had the disadvantage that they were the smallest absorption dips in the spectrum, but their frequencies were well separated from the other hyperfine components.

6.9 Cross-Phase Shift Measurement

We then returned to our phase shift measurement, tuning our control field to dip 1 of the xenon 823 nm spectrum and using the strongest available two-photon hyperfine component. Simultaneously monitoring the laser frequency control system, the stabilization of the amplitude modulators and Pockels cell, and the cavity temperature and RF discharge intensity was a demanding task. Within a couple of weeks though we found our first verifiable phase shift measurements.

Figure 6.15 (b) shows a sample of the data from one of our most successful initial phase shift measurement runs. For comparison, part (a) of the figure reproduces the data from a two-photon absorption measurement performed on the previous day. The phase shift signal occurred at almost exactly the same frequency as the two-photon absorption resonance, confirming that this phase shift was caused by the interaction of our two light

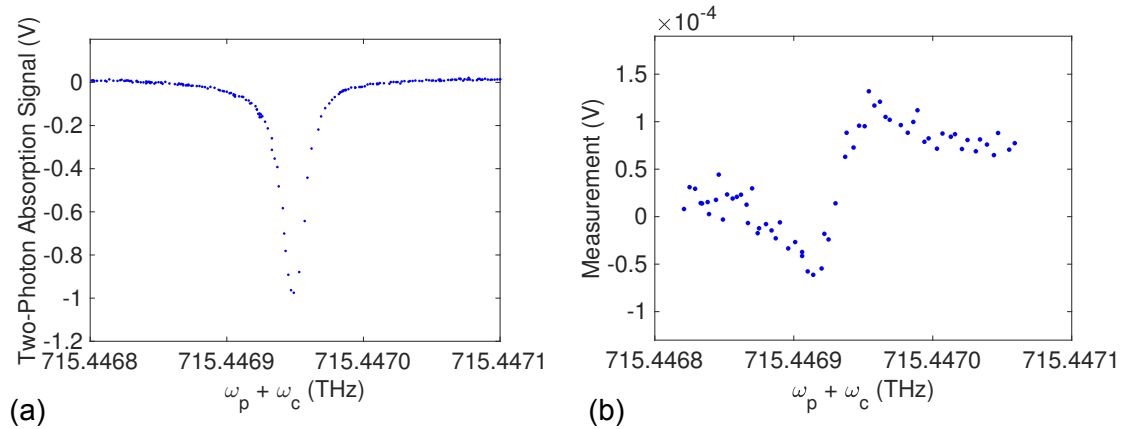


Figure 6.15: (a) A two-photon absorption measurement of the hyperfine component used for the phase shift measurement. (b) Phase shift measurement data. The amplitude of the measurement indicates that the maximum phase shift was roughly 5 mrad. Note that the two-photon absorption dip occurred at the same frequency as the phase shift. The data sets of (a) and (b) were taken about one day apart.

fields with metastable xenon atoms in the cavity. There was a slight frequency alignment mismatch of ~ 20 MHz between parts (a) and (b) of the figure. This was probably caused by slow drifts in the wavemeter calibration or by changing conditions in RF discharge within the vacuum chamber.

Not all of the measurement runs produced data as clean as that of Figure 6.15 (b). The same slowly-varying noise terms that produced the chaotic behavior evident in Figure 6.12 were still present, and in several runs the data was distorted significantly. Figure 6.16 shows data from another measurement run. The unusual features in this data were probably caused by spurious 823 nm control pulses back-reflected from the cavity. These pulses reached the detector at the same time as the measurement signals.

We added a pair of narrowband 853 nm optical filters in front of our balanced detector to remove the effects of back-reflected control pulses. Figure 6.17 shows the results of one measurement performed after the filters were installed. Attenuation loss at the filters reduced the amplitude of the measured signal by roughly a factor of 4, but the spurious noise had been eliminated.

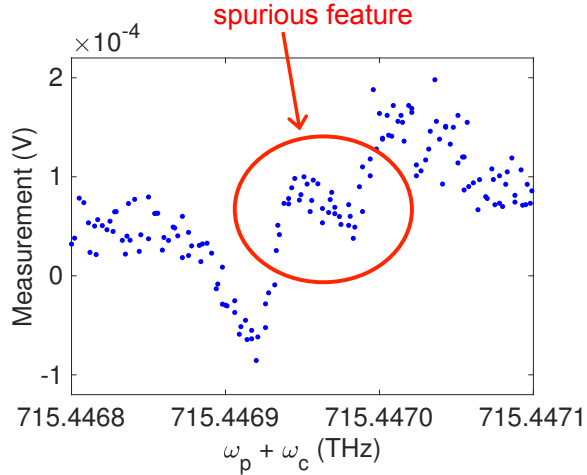


Figure 6.16: Data from another phase shift measurement run. The spurious feature that sets this data apart from the results of Figure 6.15 was probably caused by back-reflected 823 nm control pulses. Placing a pair of 853 nm narrowband optical filters in front of the balanced detector ports eliminated the noise, as shown in Figure 6.17.

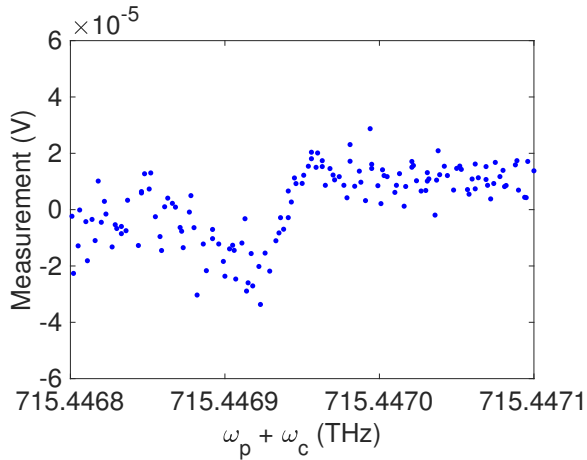


Figure 6.17: Phase shift data recorded after the inclusion of a pair of narrowband 853 nm optical filters to remove back-reflected control pulses from the detection events. The signal strength was reduced because of attenuation at the filters, but the noise had been removed as well.

6.10 Theoretical Description

In order to properly understand our experimental results, it was important to develop a theory capable of describing the nonlinear interaction between the intracavity control and probe fields in our system. This interaction can be described using a semiclassical method

based on the analysis of Section 2.4. We will begin here with the Hamiltonian describing the evolution of a 3-level atom interacting with two classical fields,

$$\hat{H} = \hbar \sum_{i=1}^3 \omega_i \hat{\sigma}_{ii} + \mu_{21} E_c (e^{i\omega_c t} \hat{\sigma}_{12} + e^{-i\omega_c t} \hat{\sigma}_{21}) + \mu_{32} E_p (e^{i\omega_p t} \hat{\sigma}_{23} + e^{-i\omega_p t} \hat{\sigma}_{32}). \quad (6.1)$$

This is a straightforward extension of Eq. 2.27 to the case of a 3-level atom. Here μ_{ij} indicates the dipole matrix element for the atomic $|j\rangle$ to $|i\rangle$ transition, and ω_i the energy of the atomic level $|i\rangle$. E_c and E_p represent the control and probe field amplitudes, respectively. The atomic operators are defined $\hat{\sigma}_{ij} \equiv |i\rangle \langle j|$, as in Section 2.3. To include the effects of atomic spontaneous decay we needed to use the master equation. Assuming that each atom is a closed 3-level system, the master equation can be written

$$\begin{aligned} \frac{d\hat{\rho}}{dt} = & -\frac{i}{\hbar} [\hat{H}, \hat{\rho}] - \frac{\Gamma_{21}}{2} (\hat{\sigma}_{21} \hat{\sigma}_{12} \hat{\rho} - 2\hat{\sigma}_{12} \hat{\rho} \hat{\sigma}_{21} + \hat{\rho} \hat{\sigma}_{21} \hat{\sigma}_{12}) - \dots \\ & - \frac{\Gamma_{32}}{2} (\hat{\sigma}_{32} \hat{\sigma}_{23} \hat{\rho} - 2\hat{\sigma}_{23} \hat{\rho} \hat{\sigma}_{32} + \hat{\rho} \hat{\sigma}_{32} \hat{\sigma}_{23}). \end{aligned} \quad (6.2)$$

We have used Γ_{21} and Γ_{32} for the atomic spontaneous transition rates of the $|2\rangle$ to $|1\rangle$ and $|3\rangle$ to $|2\rangle$ transitions, respectively. The equations of motion for the density matrix elements are

$$\begin{aligned} \dot{\rho}_{11} &= \Gamma_{21} \rho_{22} - i\Omega_{21} (e^{-i\omega_c t} \rho_{12} - e^{i\omega_c t} \rho_{21}) \\ \dot{\rho}_{22} &= -\Gamma_{21} \rho_{22} + \Gamma_{32} \rho_{33} + i\Omega_{21} (e^{-i\omega_c t} \rho_{12} - e^{i\omega_c t} \rho_{21}) - i\Omega_{32} (e^{-i\omega_p t} \rho_{23} - e^{i\omega_p t} \rho_{32}) \\ \dot{\rho}_{33} &= -\Gamma_{32} \rho_{33} + i\Omega_{32} (e^{-i\omega_p t} \rho_{23} - e^{i\omega_p t} \rho_{32}) \\ \dot{\rho}_{12} &= -\frac{\Gamma_{21}}{2} \rho_{12} + i\omega_{12} \rho_{12} - i\Omega_{21} e^{i\omega_c t} (\rho_{11} - \rho_{22}) - i\Omega_{32} e^{-i\omega_p t} \rho_{13} \\ \dot{\rho}_{23} &= -\frac{1}{2} (\Gamma_{32} + \Gamma_{21}) \rho_{23} + i\omega_{23} \rho_{23} + i\Omega_{21} e^{-i\omega_c t} \rho_{13} + i\Omega_{32} e^{i\omega_p t} (\rho_{33} - \rho_{22}) \\ \dot{\rho}_{13} &= -\frac{\Gamma_{32}}{2} \rho_{13} + i(\omega_{23} + \omega_{12}) \rho_{13} + i\Omega_{21} e^{i\omega_c t} \rho_{23} - i\Omega_{32} e^{i\omega_p t} \rho_{12}, \end{aligned} \quad (6.3)$$

where we have used $\Omega_{21} \equiv \frac{\mu_{21} E_c}{\hbar}$ and $\Omega_{32} \equiv \frac{\mu_{32} E_p}{\hbar}$. We have also assumed, without loss of generality, that Ω_{21} and Ω_{32} are both real and positive.

Real xenon atoms are open systems, i.e. it is possible for the levels $|2\rangle$ and $|3\rangle$ to decay to states outside of the 3-level structure considered here. These decays have the effect of gradually removing population from the system over time. The RF discharge in our vacuum chamber counteracted this effect by continually pumping atoms back into the metastable state. In the case of continuous-wave (CW) excitation it would have been important for a theoretical treatment to account for both of these effects. Our system though used pulsed excitation. As a result the theory needed only to describe the system dynamics over time intervals of $< 1 \mu\text{s}$. Simulations using the full theory showed that over such short timescales, any effects of the open system dynamics were negligible. For the sake of simplicity we neglect these effects for the remainder of our treatment.

Now we need to account for the effects of inhomogeneous broadening. This can be done using a Monte Carlo simulation by introducing a collection of N_d frequency offsets δ_k^c and δ_k^p for the first and second atomic transitions, respectively, where $k \in \{1, 2, 3, \dots, N_d\}$. Incorporating these into the analysis leads to a set of N_d master equations, one for each velocity class.

In the standing wave geometry of our cavity, each field can be expressed as a sum of two traveling waves propagating in opposite directions. In this configuration the Doppler shift of an atomic resonance as seen by one traveling wave is the opposite of that seen by the wave traveling in the other direction. As a result, each atomic velocity class is Doppler shifted upward from the perspective of one field and downward from the perspective of the other. Assuming that the two field components are equal in magnitude, this effect can be included by making the following substitutions in Eq. 6.3:

$$\begin{aligned}
e^{-i\omega_c t} &\rightarrow \left(e^{-i\omega_{c,k}^+ t} + e^{-i(\omega_{c,k}^- t + \theta_c)} \right) \\
e^{i\omega_c t} &\rightarrow \left(e^{i\omega_{c,k}^+ t} + e^{i(\omega_{c,k}^- t + \theta_c)} \right) \\
e^{-i\omega_p t} &\rightarrow \left(e^{-i\omega_{p,k}^+ t} + e^{-i(\omega_{p,k}^- t + \theta_p)} \right) \\
e^{i\omega_p t} &\rightarrow \left(e^{i\omega_{p,k}^+ t} + e^{i(\omega_{p,k}^- t + \theta_p)} \right).
\end{aligned} \tag{6.4}$$

We have used $\omega_{c,k}^+ = \omega_c + \delta_k^c$, $\omega_{c,k}^- = \omega_c - \delta_k^c$, $\omega_{p,k}^+ = \omega_p + \delta_k^p$ and $\omega_{p,k}^- = \omega_p - \delta_k^p$. The phases θ_c and θ_p account for the arbitrary relative phase between the counter-propagating field components. This leads to the rather cumbersome set of master equations

$$\begin{aligned}
\dot{\rho}_{11,k} &= \Gamma_{21,k} \rho_{22,k} - i\Omega_{21,k} \left[\left(e^{-i\omega_{c,k}^+ t} + e^{-i(\omega_{c,k}^- t + \theta_c)} \right) \rho_{12,k} - \left(e^{i\omega_{c,k}^+ t} + e^{i(\omega_{c,k}^- t + \theta_c)} \right) \rho_{21,k} \right] \\
\dot{\rho}_{22,k} &= -\Gamma_{21,k} \rho_{22,k} + \Gamma_{32,k} \rho_{33,k} + \dots \\
&\quad + i\Omega_{21,k} \left[\left(e^{-i\omega_{c,k}^+ t} + e^{-i(\omega_{c,k}^- t + \theta_c)} \right) \rho_{12,k} - \left(e^{i\omega_{c,k}^+ t} + e^{i(\omega_{c,k}^- t + \theta_c)} \right) \rho_{21,k} \right] + \dots \\
&\quad - i\Omega_{32,k} \left[\left(e^{-i\omega_{p,k}^+ t} + e^{-i(\omega_{p,k}^- t + \theta_p)} \right) \rho_{23,k} - \left(e^{i\omega_{p,k}^+ t} + e^{i(\omega_{p,k}^- t + \theta_p)} \right) \rho_{32,k} \right] \\
\dot{\rho}_{33,k} &= -\Gamma_{32,k} \rho_{33,k} + i\Omega_{32,k} \left[\left(e^{-i\omega_{p,k}^+ t} + e^{-i(\omega_{p,k}^- t + \theta_p)} \right) \rho_{23,k} - \dots \right. \\
&\quad \left. - \left(e^{i\omega_{p,k}^+ t} + e^{i(\omega_{p,k}^- t + \theta_p)} \right) \rho_{32,k} \right] \\
\dot{\rho}_{12,k} &= -\frac{\Gamma_{21,k}}{2} \rho_{12,k} + i\omega_{12,k} \rho_{12,k} - i\Omega_{21,k} \left(e^{i\omega_{c,k}^+ t} + e^{i(\omega_{c,k}^- t + \theta_c)} \right) (\rho_{11,k} - \rho_{22,k}) - \dots \\
&\quad - i\Omega_{32,k} \left(e^{-i\omega_{p,k}^+ t} + e^{-i(\omega_{p,k}^- t + \theta_p)} \right) \rho_{13,k} \\
\dot{\rho}_{23,k} &= -\frac{1}{2} (\Gamma_{32,k} + \Gamma_{21,k}) \rho_{23,k} + i\omega_{23,k} \rho_{23,k} + i\Omega_{21,k} \left(e^{-i\omega_{c,k}^+ t} + e^{-i(\omega_{c,k}^- t + \theta_c)} \right) \rho_{13,k} + \dots \\
&\quad + i\Omega_{32,k} \left(e^{i\omega_{p,k}^+ t} + e^{i(\omega_{p,k}^- t + \theta_p)} \right) (\rho_{33,k} - \rho_{22,k}) \\
\dot{\rho}_{13,k} &= -\frac{\Gamma_{32,k}}{2} \rho_{13,k} + i(\omega_{23,k} + \omega_{12,k}) \rho_{13,k} + i\Omega_{21,k} \left(e^{i\omega_{c,k}^+ t} + e^{i(\omega_{c,k}^- t + \theta_c)} \right) \rho_{23,k} - \dots \\
&\quad - i\Omega_{32,k} \left(e^{i\omega_{p,k}^+ t} + e^{i(\omega_{p,k}^- t + \theta_p)} \right) \rho_{12,k},
\end{aligned} \tag{6.5}$$

with one master equation for each velocity class k . The fact that each transition is driven by fields at two distinct frequencies makes this system quite difficult to solve. To simplify the problem we assume that the rightward- and leftward-traveling 823 nm control fields interact

with independent ensembles, allowing us to remove one of the two control field terms in Eq. 6.5. In doing this we neglect the coherent dynamics unique to atomic systems driven with bichromatic fields. These dynamics are quite interesting, but are beyond the scope of our treatment here [107–109].

The remaining system contains two sets of interaction terms, one describing a Doppler-free two-photon transition with counterpropagating control and probe fields, and the other describing a Doppler-broadened two-photon interaction with copropagating fields. For small detunings close to a two-photon resonance the Doppler-free part of the interaction dominates, so we neglect the much smaller Doppler-broadened part. After these approximations the master equations simplify to

$$\begin{aligned}
\dot{\rho}_{11,k} &= \Gamma_{21,k} \rho_{22,k} - i\Omega_{21,k} \left(e^{-i\omega_{c,k}^+ t} \rho_{12,k} - e^{i\omega_{c,k}^+ t} \rho_{21,k} \right) \\
\dot{\rho}_{22,k} &= -\Gamma_{21,k} \rho_{22,k} + \Gamma_{32,k} \rho_{33,k} + i\Omega_{21,k} \left(e^{-i\omega_{c,k}^+ t} \rho_{12,k} - e^{i\omega_{c,k}^+ t} \rho_{21,k} \right) - \dots \\
&\quad - i\Omega_{32,k} \left(e^{-i\omega_{p,k}^+ t} \rho_{23,k} - e^{i\omega_{p,k}^+ t} \rho_{32,k} \right) \\
\dot{\rho}_{33,k} &= -\Gamma_{32,k} \rho_{33,k} + i\Omega_{32,k} \left(e^{-i\omega_{p,k}^+ t} \rho_{23,k} - e^{i\omega_{p,k}^+ t} \rho_{32,k} \right) \\
\dot{\rho}_{12,k} &= -\frac{\Gamma_{21,k}}{2} \rho_{12,k} + i\omega_{12,k} \rho_{12,k} - i\Omega_{21,k} e^{i\omega_{c,k}^+ t} (\rho_{11,k} - \rho_{22,k}) - i\Omega_{32,k} e^{-i\omega_{p,k}^+ t} \rho_{13,k} \\
\dot{\rho}_{23,k} &= -\frac{1}{2} (\Gamma_{32,k} + \Gamma_{21,k}) \rho_{23,k} + i\omega_{23,k} \rho_{23,k} + i\Omega_{21,k} e^{-i\omega_{c,k}^+ t} \rho_{13,k} + \\
&\quad + i\Omega_{32,k} e^{i\omega_{p,k}^+ t} (\rho_{33,k} - \rho_{22,k}) \\
\dot{\rho}_{13,k} &= -\frac{\Gamma_{32,k}}{2} \rho_{13,k} + i(\omega_{23,k} + \omega_{12,k}) \rho_{13,k} + i\Omega_{21,k} e^{i\omega_{c,k}^+ t} \rho_{23,k} - i\Omega_{32,k} e^{i\omega_{p,k}^+ t} \rho_{12,k} .
\end{aligned} \tag{6.6}$$

From this point, the δ_k^c should be chosen at random from a Gaussian distribution with a width of 440 MHz, corresponding to the Doppler width of the 823 nm Xe transition. The probe field frequency offsets should be given by $\delta_k^p = 0.964 \times \delta_k^c$. Each value of δ_k^c represents a distinct velocity class of Xe atoms.

Next we move into a new basis that rotates along with the driving fields. Let $\sigma_{12,k} \equiv \rho_{12,k} e^{-i\omega_{c,k}^+ t}$, $\sigma_{23,k} \equiv \rho_{23,k} e^{-i\omega_{p,k}^+ t}$, and $\sigma_{13,k} \equiv \rho_{13,k} e^{-i(\omega_{c,k}^+ + \omega_{p,k}^+) t}$. For consistency

in notation we will use $\sigma_{ii,k} \equiv \rho_{ii,k}$, with $i \in \{1, 2, 3\}$. After the substitution the equations of motion become [65]

$$\begin{aligned}
\dot{\sigma}_{11,k} &= \Gamma_{21}\sigma_{22,k} - i\Omega_{21}(\sigma_{12,k} - \sigma_{21,k}) \\
\dot{\sigma}_{22,k} &= -\Gamma_{21}\sigma_{22,k} + \Gamma_{32}\sigma_{33,k} + i\Omega_{21}(\sigma_{12,k} - \sigma_{21,k}) - i\Omega_{32}(\sigma_{23,k} - \sigma_{32,k}) \\
\dot{\sigma}_{33,k} &= -\Gamma_{32}\sigma_{33,k} + i\Omega_{32}(\sigma_{23,k} - \sigma_{32,k}) \\
\dot{\sigma}_{12,k} &= -\frac{\Gamma_{21}}{2}\sigma_{12,k} - i\Delta_k\sigma_{12,k} + i\Omega_{21}(\sigma_{22,k} - \sigma_{11,k}) - i\Omega_{32}\sigma_{13,k} \\
\dot{\sigma}_{23,k} &= -\frac{1}{2}(\Gamma_{21} + \Gamma_{32})\sigma_{23,k} - i(\delta_k - \Delta_k)\sigma_{23,k} + i\Omega_{21}\sigma_{13,k} + i\Omega_{32}(\sigma_{33,k} - \sigma_{22,k}) \\
\dot{\sigma}_{13,k} &= -\frac{\Gamma_{32}}{2}\sigma_{13,k} - i\delta_k\sigma_{13,k} + i\Omega_{21}\sigma_{23,k} - i\Omega_{32}\sigma_{12,k} .
\end{aligned} \tag{6.7}$$

We have used $\Delta_k \equiv \omega_{c,k}^+ - \omega_{21}$ and $\delta_k \equiv \omega_{c,k}^+ + \omega_{p,k}^+ - \omega_{21} - \omega_{32}$, as illustrated in Figure 6.1.

Eq. 6.7 describes the evolution of an ensemble of Doppler-broadened metastable Xe atoms interacting with the classical control and probe fields in the cavity. Next we must account for the evolution of the intracavity fields. Figure 6.18 illustrates the model used to describe the time evolution of the control and probe fields within the cavity. We first assume a field amplitude $E_i(t)$ just inside the left cavity mirror propagating towards the right, using the index $i \in \{c, p\}$ to indicate the control and probe fields, respectively. Say we wait just long enough to allow the wavefront of this field to propagate back-and-forth across the cavity exactly once. After this the field amplitude will be

$$E_i(t + \tau_i) = tE_i^0(t) + r^2e^{-\beta_i + i\phi_i}E_i(t). \tag{6.8}$$

We have used r and t for the amplitude reflection and transmission coefficients of the mirrors, $E_i^0(t)$ for the input field amplitude, and τ_i for the time required by the field to make one round trip within the cavity. The parameters β_i and ϕ_i indicate the attenuation and

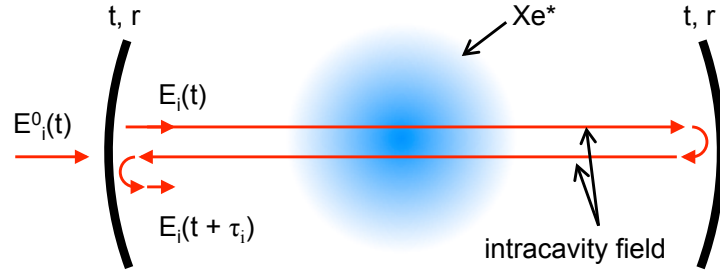


Figure 6.18: Illustration of the time evolution of a wavefront of the intracavity field. Starting at time t the field makes one round trip within the cavity, and receives modifications to its amplitude and phase from interactions with metastable Xe atoms and from reflections off of the mirror surfaces. These modifications combine with the contribution of the field at the cavity input $E_i^0(t)$ to give the new value of the field at time $t + \tau_i$, where τ_i is the time required for a single round-trip.

phase shift imparted by interaction with the Xe atoms, and are given by

$$\begin{aligned}\beta_i &= \frac{\omega_i \tau_i}{2} \text{Im}\{\chi_i\} \\ \phi_i &= \frac{\omega_i \tau_i}{2} \text{Re}\{\chi_i\},\end{aligned}\tag{6.9}$$

where ω_i is the angular frequency of the field. For an ensemble of atoms the susceptibilities are given by

$$\begin{aligned}\chi_c &= N_v \frac{\mu_{21}^* \sigma_{21}(t)}{E_c(t)} \\ \chi_p &= N_v \frac{\mu_{32}^* \sigma_{32}(t)}{E_p(t)},\end{aligned}\tag{6.10}$$

where N_v is the volume number density of metastable xenon atoms [65]. Assuming that τ_i is small, we can approximate the time derivative of $E_i(t)$ by the finite difference $\dot{E}_i(t) \approx [E_i(t + \tau_i) - E_i(t)] / \tau_i$. We find

$$\dot{E}_i(t) \approx [tE_i^0(t) + (r^2 e^{-\beta_i + i\phi_i} - 1) E_i(t)] / \tau_i.\tag{6.11}$$

The susceptibilities couple the field evolution of Eq. 6.11 with the evolution of the xenon atoms given in Eq. 6.7. This system of coupled differential equations describes the interaction of the cavity fields with an ensemble of inhomogeneously broadened Xe atoms.

Equations 6.7 and 6.9 - 6.11 were solved numerically to simulate the expected measurement outcome. The calculation from this point forward proceeded in finite time steps. For each step the evolution of the density matrices for each atomic velocity group was calculated separately, along with the evolution of the fields. The values of χ_c and χ_p were then calculated by averaging over the density matrices of all velocity groups, and were stored in memory for the next step. This process was repeated until the full system evolution had been calculated to the desired evolution time, typically on the order of 500 ns.

Figure 6.19 shows a sample result of a single run of the numerical simulation. Part (a) on the left shows the calculated control and probe field intensities transmitted through the cavity. The occupation probabilities of atomic states $|2\rangle$ and $|3\rangle$ are shown as well. The evolution of the transmitted intensity for the control and probe fields possess two separate segments. The first segment represents the buildup period as the field amplitude accumulates due to constructive interference between the input light and the field in the cavity. During this segment the intensity increases quadratically with time. This lasts for the duration of the input pulses (30 ns for the control and 60 ns for the probe, in the current example). Once the input pulses reach their end the intensity begins to fall off exponentially, with the rate of decay given by the cavity lifetime $\frac{1}{\kappa} \approx 80$ ns. Because the simulation was run using a large value of Δ , the population of state $|2\rangle$ closely follows the control field intensity. The behavior of the state $|3\rangle$ population is similar, but with the addition of Rabi oscillations with a period of roughly 200 ns. These relatively slow Rabi oscillations are the result of the small two-photon detuning of $\delta \approx 5$ MHz used in the simulation.

Part (b) of Figure 6.19 shows the intensity of the transmitted probe pulse along with its phase. While the phase shift accumulates within the cavity over time, the intensity of the transmitted probe field falls rapidly after the onset of the exponential cavity decay. As a result the SNR for measurements taken after $t = 100$ ns tend to be small. In light of this fact, our measurements in the laboratory were taken with $t < 100$ ns.

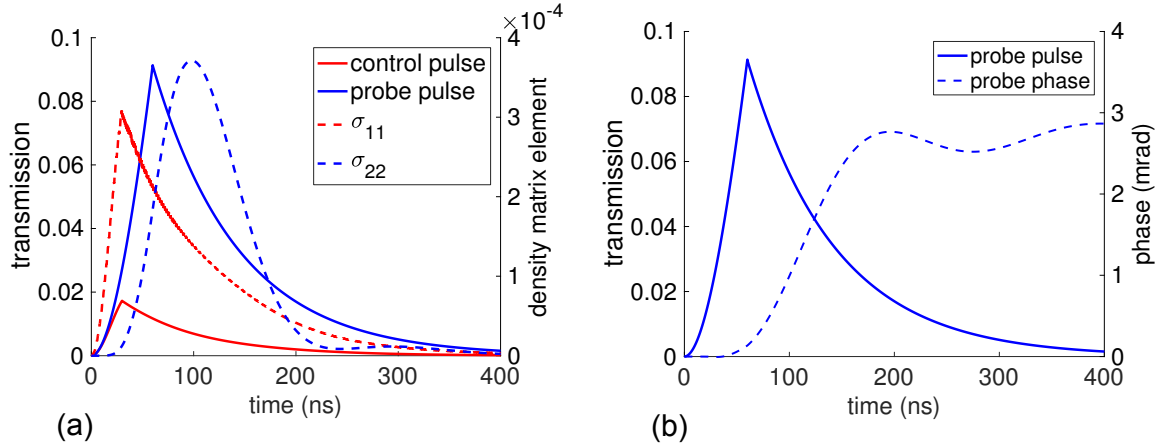


Figure 6.19: Results from a sample run of the numerical simulation used to predict phase shift measurements. (a) Control and probe field transmitted intensities calculated at the cavity output mirror, along with the occupation probabilities of the first and second atomic excited states as a function of time. (b) Intensity and phase of the transmitted probe field. The dashed red curve in (b) shows the size of the signal that would be seen by a homodyne detector measuring these results. For all curve the point $t = 0$ marks the time at which the 60 ns probe pulse first strikes the cavity.

6.11 Results and Conclusions

Figure 6.20 plots a set of phase shift measurement data alongside the results of a theory simulation. The theory results used a typical set of experimental parameters. The durations of the probe and control pulses were chosen to be 60 and 30 ns, respectively, to match the values used in the experiment. The atomic decay and transition rates, dipole moments, and measurement acquisition time used in the calculations were also the same as those in the experiment. The effective density of metastable Xe atoms and the delay time between the control and probe pulses were varied within the experimental uncertainties to give the best fit between the simulation and the measured data. Agreement between the two was quite good.

The maximum cross-phase shift of 5 mrad in Figure 6.20 was achieved using 5 fJ control field pulses. This corresponded to the presence of roughly 18,000 control field photons within the cavity. Thus for this measurement the cross-phase shift per control field

Chapter 7

New Cavity System

7.1 Overview

In the previous chapters we demonstrated that the use of metastable xenon vapor inside a high-finesse cavity leads to very large optical nonlinearities, with the presence of a few thousand photons producing measurable changes in the optical properties of the system. The nonlinearities we have seen in this work so far, however, were too weak to be useful for experiments in quantum nonlinear optics. Reaching this regime required an improved cavity. The new cavity needed to have higher finesse and shorter length. We wanted also to achieve faster frequency tuning control by using piezoelectric elements rather than temperature control. In this chapter we describe the new cavity system that was built to meet these needs.

7.2 Design Considerations

Increasing the finesse of a cavity has the effect of reducing κ , the rate of photon loss from absorption, scattering, and transmission at the mirrors (see Figure 2.7 for reference). How-

ever, it leaves g and γ unchanged. Reducing the cavity length d leads to the confinement of intracavity photons within a smaller volume, effectively increasing in the magnitude of the electric field produced by a single photon. This results in an increase in the coherent coupling rate g . At the same time though, decreasing d reduces the amount of time required for wavefronts of the intracavity field to traverse the cavity. This leads to an increase in κ . Thus, in order to increase the coherent coupling rate g of a Fabry-Perot cavity system without also increasing dissipation, one must simultaneously increase the cavity's finesse and reduce its length proportionately.

In order to reach the strengths of nonlinearities required for single-photon nonlinear optics, our new cavity system needed to have a cooperativity of $\eta \approx 1$. The finesse required for this was on the order of 100,000 to 300,000. We purchased a new set of mirrors from OptoSigma Corporation, with reflectivities designed for $R = 99.9985\%$. Mirrors of this quality should produce a cavity with a finesse greater than 200,000.

The smallest achievable cavity length for our system was limited by the need for double-resonance with a two-photon transition, like the transition diagram illustrated in Figure 6.1. We generated a spreadsheet file enumerating all values of the cavity length d that supported a normal mode resonant with the 823 nm transition in Xe, from $d \approx 20 \mu\text{m}$ to $d > 3 \text{ mm}$. We then searched the list for any values of d that simultaneously supported a second resonant mode within $\pm 2 \text{ GHz}$ of one of the Xe transitions available from state $6p[3/2]_2$. After scouring the Xe transitions catalogued in the NIST database of atomic spectra (reference [78]) we found one which would allow our cavity to satisfy the criterion of double resonance with a length of only $d \approx 300 \mu\text{m}$. The resulting 3-level diagram is illustrated in Figure 7.1.

A cavity with such high finesse and short length is extremely sensitive to slight changes in d . For the cavity to function properly, the amplitude of mechanical vibrations must be kept below 0.01 \AA . This is less than $1/10$ the diameter of a hydrogen atom! Vibra-

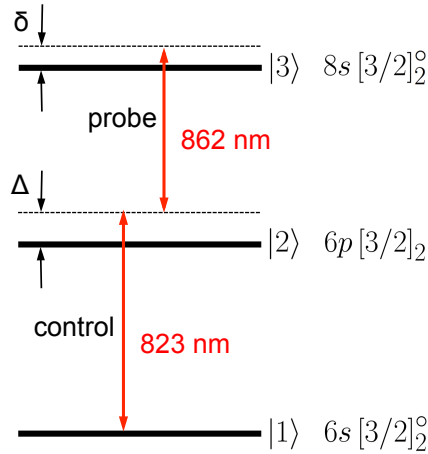


Figure 7.1: Energy level diagram to be used for producing cross-phase shifts in the new cavity. The 862 nm $6p[3/2]_2$ to $8s[3/2]_2^o$ transition has a more favorable branching ratio than the 853 nm transition of Figure 6.1.

tions caused by ambient sounds and air currents largely disappear once the cavity is placed under vacuum. Vibrations within the floor of the room can be more problematic. These can be mitigated though by mounting the vacuum system on a floating optical table, and by designing the cavity mount to damp the remaining vibrations as far as possible.

In designing the new cavity our group benefited greatly from the excellent work done in the research group of Jeff Kimble at CalTech [110, 111]. The designs of our new high-finesse cavity and its mounting system were based largely on successful cavity systems developed by that group.

7.3 The New Cavity

Figure 7.2 illustrates the construction of the new cavity mount. The cavity was supported by two solid copper blocks, each seated on a Viton o-ring to help dampen vibrations. These were mounted on a 4.5" ConFlat vacuum flange. On top of the copper supports, a stainless steel block served as a baseplate for the cavity mirrors. Two steel mounting plates were then mounted on the base. The mounting plates were free to slide along the surface of the

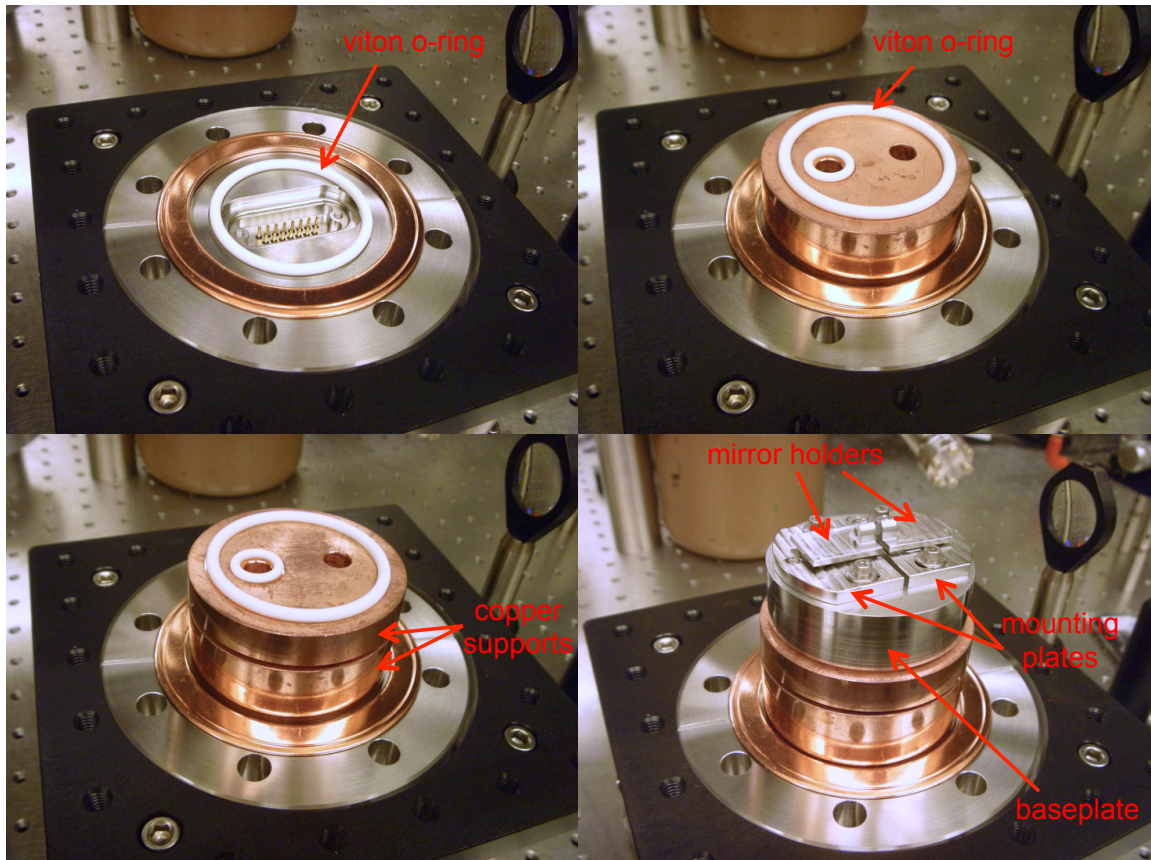


Figure 7.2: Series of 4 photographs illustrating the design of the new cavity mount.

baseplate to facilitate easier alignment of the mirrors. Once aligned the plates could be tightened down with screws, as in the photo.

Figure 7.3 shows a closeup of the cavity itself. A piezoelectric shear stack was glued into the top of each of the movable mounting plates (not visible in the figures) to tune the cavity frequency. A steel mirror holder was glued onto each of these piezos, and a mirror was mounted in each holder and held in place with a viton-tipped set screw. This allowed for easy changing of the cavity mirrors without the need to disassemble the mount. The mirror substrates were 3 mm in diameter at the center, and tapered down to a diameter of 1.5 mm at the mirror faces. The taper allowed the mirrors to be placed closer together than would otherwise have been possible.

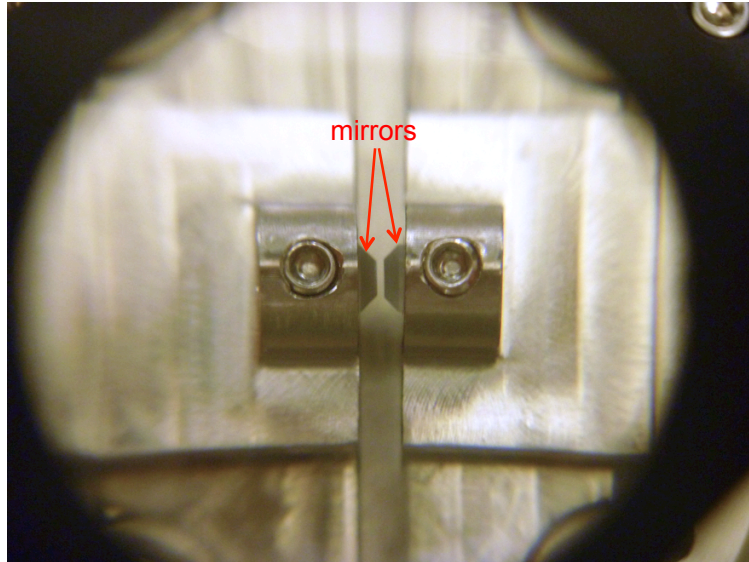


Figure 7.3: Closeup view of the cavity mirrors.

With this cavity we were able to align an input laser to the fundamental transverse mode, and to begin making some stability measurements. In the process though several of our mirrors were damaged. Images of the cracked mirrors are provided in Figure 7.4. The steel mirror holders and set screws were simply too rough on the delicate glass substrates. We attempted to make the mounting process gentler, by handling and tightening the mirrors more carefully, but this did not help. In addition, it proved difficult to align the mirrors with this mounting system. Transverse alignment could be accomplished by adjusting the positions of the movable mounting plates. To adjust the vertical alignment though we were forced to insert thin strips of metal shim stock underneath one or the other of the mounting plates. As this was our only means of adjusting both the heights and the vertical orientations of the mirrors, the process of achieving a good alignment was extremely tedious and time consuming. After several weeks spent on this and similar tasks, we decided to design a new mount that would be easier to align and gentler with the mirrors.

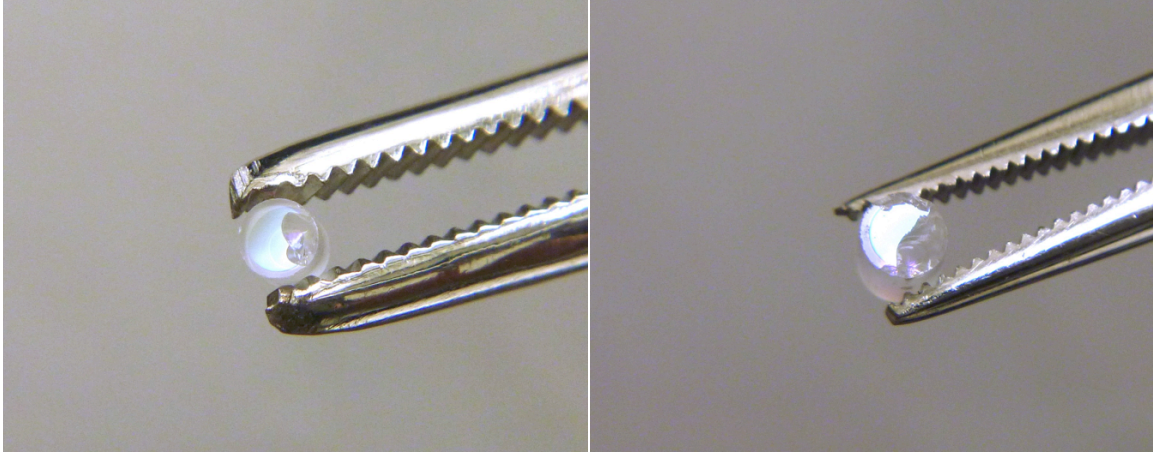


Figure 7.4: Mirrors damaged after mounting in the steel mirror holders.

7.4 Redesign of the New Cavity

Our primary purposes in redesigning the cavity mount were to achieve greater ease of alignment and less frequent damage of the mirrors. Both of these goals could be accomplished simultaneously by mounting the mirrors with glue, rather than using metal holders and set screws. Though the use of glue makes it more difficult to remove and replace the mirrors, it is very common in state-of-the-art cavity QED systems used by other groups [111, 112].

In the new design, each cavity mirror was mounted on a pair of ceramic v-grooves. A shear piezo plate was sandwiched between each pair of v-grooves for cavity tuning. Holes were drilled through the v-grooves to allow wire leads to connect to the top and bottom electrodes of each piezo plate. Tiny steel springs were inserted into these holes. The insulation of each piezo wire lead was then glued within the “v” of the associated v-groove, and a length of bare wire was coiled into the v-groove hole. The tiny spring was pressed by the coiled wire lead on one side and by the piezo electrode on the other, maintaining electrical contact between them. A pair of custom stainless steel caps were then designed to fit over the v-groove assemblies, to protect them from the RF discharge. Holes were drilled through the cap walls to allow optical fields to couple into the cavity.

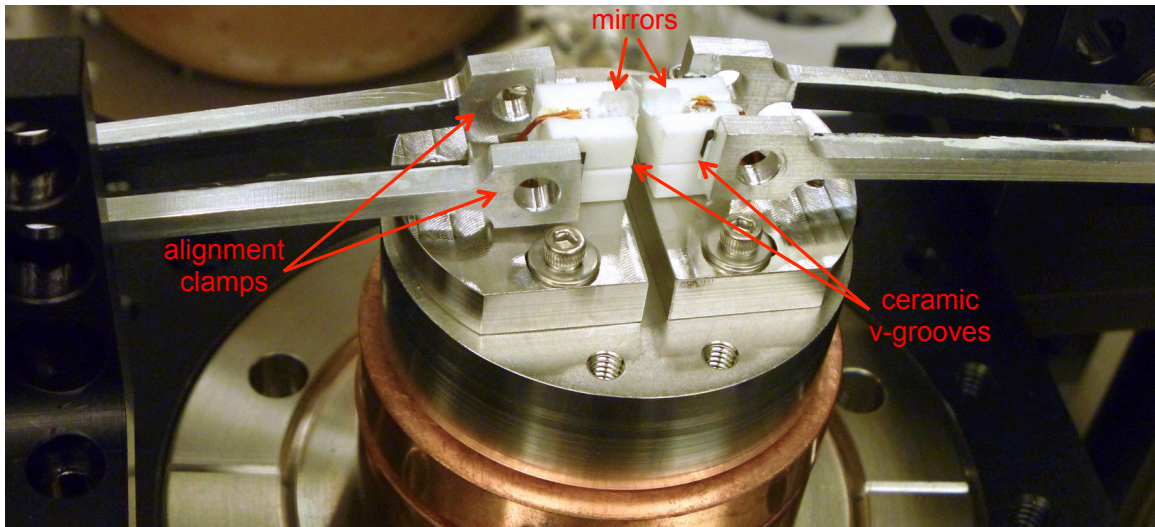


Figure 7.5: Photo of the redesigned cavity mount, during the process of aligning the mirrors.

Figure 7.5 illustrates the procedure for the initial alignment of the cavity mirrors. First the v-grooves and piezo plates were glued together with Torr Seal epoxy and left to set overnight. The v-groove assemblies were then fastened with clamps to a pair of 3-axis translation stages. The two mirrors were carefully set within the v-grooves, and a small drop of Torr Seal was added to fasten each mirror in place. While the glue on the mirrors was still drying, small adjustments to the mirror positions were made using the translation stages. The small drops of epoxy attaching the mirrors to their v-grooves allowed the mirror orientations to be adjusted slightly by carefully prodding the mirror substrates. Iterative adjustments to the orientations were made, and the relative orientation was checked by moving the mirrors very close together and viewing them underneath a strong magnifying lens. The risk of damaging the mirrors with this procedure was relatively low, since the curvature of the mirror surfaces prevented them from coming into direct contact [111]. See Figure 7.6 for an illustration.

When a good alignment was achieved Torr Seal was used again to fasten the v-groove assemblies in place on top of the cavity mounting plates, as shown in Figure 7.7. The setup was then left for the glue to set overnight. Once the Torr Seal had set the clamps were removed and the cavity was ready for use.

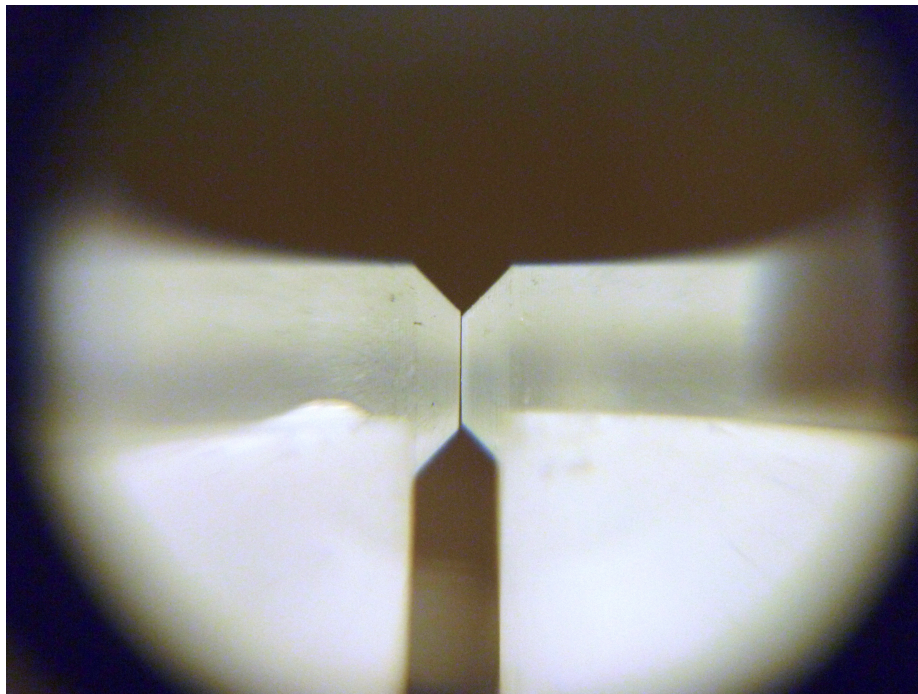


Figure 7.6: Closeup photo illustrating the relative orientations of the mirrors after initial alignment.

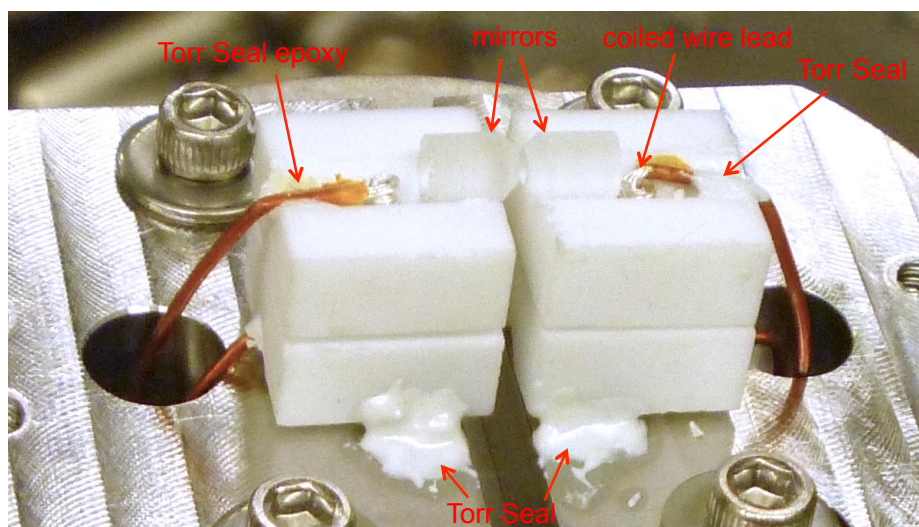


Figure 7.7: Photo of the cavity mirrors and their supporting structure. The stainless steel caps protecting the piezos from the discharge had been removed to allow the v-groove assemblies to be seen.

After aligning the cavity we measured its finesse and found it to be roughly 80,000. This is a factor of $3 \sim 4$ lower than what we would like. We expect though that with a few weeks of testing, and perhaps with some extra attention taken to careful handling of the mirrors, we should be able to bring the number up to at least 200,000. This will allow our cavity system to produce single-photon optical nonlinearities with sizes large enough to be useful for applications in quantum information processing with weak nonlinearities.

Chapter 8

Conclusion and Summary

In this work we have introduced a new apparatus for producing weak single-photon nonlinearities, based on the use of metastable xenon vapor as a nonlinear medium within a high-finesse optical cavity. It has been the purpose of this document to describe this new system, explain its importance, and relate several proof-of-principle experiments that demonstrated its effectiveness. We also included some details regarding a new cavity system which should produce even stronger nonlinearities. We close here by reviewing the highlights of the previous chapters.

In Chapter 1 we introduced the basic principles of quantum communication, and discussed the challenges associated with its performance over a lossy channel. We briefly discussed recent work in the field of quantum nonlinear optics, as it relates to this and similar problems. We then introduced our new system for producing weak single-photon nonlinearities using metastable xenon in a cavity.

Chapter 2 reviewed some technical details associated with the use of optical cavities, and reviewed the basic theory of cavity quantum electrodynamics (cavity QED). We introduced the well-known Jaynes-Cummings Hamiltonian and investigated some of the particularly interesting dynamics that occur in single-atom cavity systems. Then we de-

scribed the important concepts of dissipation and dephasing in cavity QED, leading to the master equation formalism for the density matrix of an open quantum system.

In Chapter 3 we examined the important question of the spectroscopic properties of Xe atoms. We reviewed the basic theory behind the coupling schemes most commonly used in the description of atomic spectra, and we used the jl coupling scheme to describe the energy level structure of atomic Xe. After this we discussed the shapes of atomic absorption lines resulting from homogeneous and inhomogeneous broadening mechanisms and from hyperfine splittings. A comparison of our theoretical results with an experimentally-measured absorption spectrum of the 823 nm $6s[3/2]_2^{\circ}$ to $6p[3/2]_2$ transition in Xe demonstrated good agreement.

In Chapter 4 we described the technical details of our first proof-of-principle cavity system. After an overview of the vacuum system we discussed our methods of exciting Xe atoms into the metastable state, including DC and RF discharges and optical pumping techniques. We also detailed the design and construction of the cavity itself, calling attention to a few of the most prominent technical challenges we encountered while using it.

Chapter 5 recounted an experimental demonstration of ultralow-power absorption saturation using this cavity system. In this experiment we demonstrated the advantages of using a high-finesse cavity to dramatically enhance the strength of the optical nonlinearities inherent in Xe atoms. We began with a note on the relationship between critical coupling of a cavity QED system and the intracavity absorption. We then described our laboratory system and experimental methods for this measurement. The results shown in Section 5.7 demonstrate that absorption saturation effects began to take place with input probe field power levels of nW. A similar experiment in free space would have observed the same effects occurring with power levels of μ W, indicating that the use of our cavity resulted in an enhancement of the nonlinearity of Xe atoms by a factor of roughly 1,000.

Chapter 6 described our measurement of cross-phase modulation using the cavity. After explaining the physical mechanism for producing the cross-phase shift, we reviewed some of the details of the experimental apparatus used and the steps taken to achieve a good signal-to-noise ratio in the final measurement. We then developed a theoretical model to predict the outcomes of experiment runs, with inhomogeneous broadening accounted for using numerical Monte-Carlo simulations. Our measurement results showed that our system produced cross-phase shifts of 5 mrad using 5 fJ control field pulses.

In Chapter 7 we reviewed our recent progress in building a new cavity system, with higher finesse and faster frequency control. We described two designs for the mounting system to support the cavity mirrors. The first one found some success, but was difficult to align and unkind to the delicate high-finesse mirror substrates. The second system was a marked improvement, being relatively straightforward to assemble and align. We have measured the cavity finesse to be about 80,000, and hope with a few weeks of work to improve it by another factor of $3 \sim 4$.

Low-power optical nonlinearities are extremely useful in optical science, and single-photon nonlinearities are an important tool in many applications of optical quantum information processing [8, 11, 20–22]. Experimental systems commonly used to produce such strong nonlinearities often rely on optically cooling and trapping individual atoms or clouds of atoms [12, 17–19, 24, 25, 27]. In this work we have shown that metastable xenon vapor in a high-finesse cavity can serve as a relatively simple and robust setup for producing very strong optical nonlinearities. Further work with our newest cavity should result in a system capable of producing weak single-photon nonlinearities useful for quantum information applications [9, 16, 30].

Chapter 9

Bibliography

- [1] J. S. Bell, “On the einstein podolsky rosen paradox,” *Physics* **1**, 195 (1964).
- [2] Alain Aspect, Jean Dalibard, and Gérard Roger, “Experimental test of bell’s inequalities using time- varying analyzers,” *Phys. Rev. Lett.* **49**, 1804–1807 (1982).
- [3] W. Tittel, J. Brendel, H. Zbinden, and N. Gisin, “Violation of bell inequalities by photons more than 10 km apart,” *Phys. Rev. Lett.* **81**, 3563–3566 (1998).
- [4] C. H. Bennett and G. Brassard, “Quantum cryptography: Public key distribution and coin tossing,” in *Proceedings of IEEE International Conference on Computers, Systems and Signal Processing* (Bangalore, India, 1984).
- [5] Charles H. Bennett, “Quantum cryptography using any two nonorthogonal states,” *Phys. Rev. Lett.* **68**, 3121–3124 (1992).
- [6] Peter W. Shor and John Preskill, “Simple proof of security of the bb84 quantum key distribution protocol,” *Phys. Rev. Lett.* **85**, 441–444 (2000).
- [7] Hoi-Kwong Lo and H. F. Chau, “Unconditional security of quantum key distribution over arbitrarily long distances,” *Science* **283**, 2050–2056 (1999).
- [8] Isaac L. Chuang and Yoshihisa Yamamoto, “Simple quantum computer,” *Phys. Rev. A* **52**, 3489–3496 (1995).
- [9] W J Munro, K Nemoto, and T P Spiller, “Weak nonlinearities: a new route to optical quantum computation,” *New J. Phys.* **7**, 137 (2005).
- [10] J. I. Cirac, P. Zoller, H. J. Kimble, and H. Mabuchi, “Quantum state transfer and entanglement distribution among distant nodes in a quantum network,” *Phys. Rev. Lett.* **78**, 3221–3224 (1997).
- [11] Stephan Ritter, Christian Nolleke, Carolin Hahn, Andreas Reiserer, Andreas Neuzner, Manuel Uphoff, Martin Mucke, Eden Figueroa, Joerg Bochmann, and Gerhard Rempe, “An elementary quantum network of single atoms in optical cavities,” *Nature* **484**, 195–200 (2012).

- [12] Andreas Reiserer and Gerhard Rempe, “Cavity-based quantum networks with single atoms and optical photons,” *Rev. Mod. Phys.* **87**, 1379–1418 (2015).
- [13] Gilles Brassard, Norbert Lütkenhaus, Tal Mor, and Barry C. Sanders, “Limitations on practical quantum cryptography,” *Phys. Rev. Lett.* **85**, 1330–1333 (2000).
- [14] P A Hiskett, D Rosenberg, C G Peterson, R J Hughes, S Nam, A E Lita, A J Miller, and J E Nordholt, “Long-distance quantum key distribution in optical fibre,” *New J. Phys.* **8**, 193 (2006).
- [15] Masahiro Takeoka, Saikat Guha, and Mark M. Wilde, “Fundamental rate-loss trade-off for optical quantum key distribution,” *Nat. Commun.* **5** (2014).
- [16] B. T. Kirby and J. D. Franson, “Nonlocal interferometry using macroscopic coherent states and weak nonlinearities,” *Phys. Rev. A* **87**, 053822 (2013).
- [17] Jürgen Volz, Michael Scheucher, Christian Junge, and Arno Rauschenbeutel, “Nonlinear π phase shift for single fibre-guided photons interacting with a single resonator-enhanced atom,” *Nat. Photon.* **8**, 965–970 (2014).
- [18] Kristin M. Beck, Mahdi Hosseini, Yiheng Duan, and Vladan Vuletić, “Large conditional single-photon cross-phase modulation,” *Proc. Natl. Acad. Sci. U.S.A.* **113**, 9740–9744 (2016).
- [19] Daniel Tiarks, Steffen Schmidt, Gerhard Rempe, and Stephan Dürr, “Optical π phase shift created with a single-photon pulse,” *Sci. Adv.* **2** (2016).
- [20] N. Imoto, H. A. Haus, and Y. Yamamoto, “Quantum nondemolition measurement of the photon number via the optical Kerr effect,” *Phys. Rev. A* **32**, 2287–2292 (1985).
- [21] Vittorio Giovannetti, Seth Lloyd, and Lorenzo Maccone, “Quantum-enhanced measurements: Beating the standard quantum limit,” *Science* **306**, 1330–1336 (2004).
- [22] H. J. Kimble, “The quantum internet,” *Nature* **453**, 1023–1030 (2008).
- [23] Ilya Fushman, Dirk Englund, Andrei Faraon, Nick Stoltz, Pierre Petroff, and Jelena Vučković, “Controlled phase shifts with a single quantum dot,” *Science* **320**, 769–772 (2008).
- [24] T. G. Tiecke, J. D. Thompson, N. P. de Leon, L. R. Liu, V. Vuletić, and M. D. Lukin, “Nanophotonic quantum phase switch with a single atom,” *Nature* **508**, 241–244 (2014).
- [25] Andreas Reiserer, Norbert Kalb, Gerhard Rempe, and Stephan Ritter, “A quantum gate between a flying optical photon and a single trapped atom,” *Nature* **508**, 237–240 (2014).
- [26] Bastian Hacker, Stephan Welte, Gerhard Rempe, and Stephan Ritter, “A photon-photon quantum gate based on a single atom in an optical resonator,” *Nature* **536**, 193–196 (2016).

- [27] Zi-Yu Liu, Yi-Hsin Chen, Yen-Chun Chen, Hsiang-Yu Lo, Pin-Ju Tsai, Ite A. Yu, Ying-Cheng Chen, and Yong-Fan Chen, “Large cross-phase modulations at the few-photon level,” *Phys. Rev. Lett.* **117**, 203601 (2016).
- [28] Io-Chun Hoi, Anton F. Kockum, Tauno Palomaki, Thomas M. Stace, Bixuan Fan, Lars Tornberg, Sankar R. Sathyamoorthy, Göran Johansson, Per Delsing, and C. M. Wilson, “Giant cross-Kerr effect for propagating microwaves induced by an artificial atom,” *Phys. Rev. Lett.* **111**, 053601 (2013).
- [29] Vivek Venkataraman, Kasturi Saha, and Alexander L Gaeta, “Phase modulation at the few-photon level for weak-nonlinearity-based quantum computing,” *Nat. Photon.* **7**, 138–141 (2013).
- [30] Philippe Grangier, Juan Ariel Levenson, and Jean-Philippe Poizat, “Quantum non-demolition measurements in optics,” *Nature* **396**, 537–542 (1998).
- [31] H. M. Gibbs, S. L. McCall, and T. N. C. Venkatesan, “Differential gain and bistability using a sodium-filled fabry-perot interferometer,” *Phys. Rev. Lett.* **36**, 1135–1138 (1976).
- [32] Hai Wang, David Goorskey, and Min Xiao, “Controlling the cavity field with enhanced Kerr nonlinearity in three-level atoms,” *Phys. Rev. A* **65**, 051802 (2002).
- [33] Haibin Wu, J. Gea-Banacloche, and Min Xiao, “Splitting of atom-cavity polariton peaks for three-level atoms in an optical cavity,” *Phys. Rev. A* **80**, 033806 (2009).
- [34] G. T. Hickman, T. B. Pittman, and J. D. Franson, “Saturated absorption at nanowatt power levels using metastable xenon in a high-finesse optical cavity,” *Opt. Express* **22**, 22882–22887 (2014).
- [35] G. T. Hickman, T. B. Pittman, and J. D. Franson, “Low-power cross-phase modulation in a metastable xenon-filled cavity for quantum-information applications,” *Phys. Rev. A* **92**, 053808 (2015).
- [36] D. I. Schuster, A. P. Sears, E. Ginossar, L. DiCarlo, L. Frunzio, J. J. L. Morton, H. Wu, G. A. D. Briggs, B. B. Buckley, D. D. Awschalom, and R. J. Schoelkopf, “High-cooperativity coupling of electron-spin ensembles to superconducting cavities,” *Phys. Rev. Lett.* **105**, 140501 (2010).
- [37] Ming Cai, Oskar Painter, and Kerry J. Vahala, “Observation of critical coupling in a fiber taper to a silica-microsphere whispering-gallery mode system,” *Phys. Rev. Lett.* **85**, 74–77 (2000).
- [38] Q. A. Turchette, C. J. Hood, W. Lange, H. Mabuchi, and H. J. Kimble, “Measurement of conditional phase shifts for quantum logic,” *Phys. Rev. Lett.* **75**, 4710–4713 (1995).
- [39] Bahaa E. A. Saleh and Malvin Carl Teich, “Fundamentals of photonics,” (John Wiley and Sons, Inc., New York, 1991) Chap. Resonator Optics, pp. 378–387, 1st ed.

- [40] Karel Patek, “Lasers,” (CRC Press, Ohio, 1964) Chap. Resonant Cavities for the Optical Region, pp. 89–96.
- [41] Yanhua Shih, *An Introduction to Quantum Optics: Photon and Biphoton Physics* (CRC Press, 2011).
- [42] E. T. Jaynes and F. W. Cummings, “Comparison of quantum and semiclassical radiation theories with application to the beam maser,” *Proc. IEEE* **51**, 89–109 (1963).
- [43] Michael Tavis and Frederick W. Cummings, “Exact solution for an n -molecule–radiation-field hamiltonian,” *Phys. Rev.* **170**, 379–384 (1968).
- [44] J. H. Eberly, N. B. Narozhny, and J. J. Sanchez-Mondragon, “Periodic spontaneous collapse and revival in a simple quantum model,” *Phys. Rev. Lett.* **44**, 1323–1326 (1980).
- [45] Bruce W. Shore and Peter L. Knight, “The Jaynes-Cummings model,” *J. Mod. Opt.* **40**, 1195–1238 (1993).
- [46] D. Meschede, H. Walther, and G. Müller, “One-atom maser,” *Phys. Rev. Lett.* **54**, 551–554 (1985).
- [47] R. J. Thompson, G. Rempe, and H. J. Kimble, “Observation of normal-mode splitting for an atom in an optical cavity,” *Phys. Rev. Lett.* **68**, 1132–1135 (1992).
- [48] J. M. Raimond, M. Brune, and S. Haroche, “Manipulating quantum entanglement with atoms and photons in a cavity,” *Rev. Mod. Phys.* **73**, 565–582 (2001).
- [49] N. B. Narozhny, J. J. Sanchez-Mondragon, and J. H. Eberly, “Coherence versus incoherence: Collapse and revival in a simple quantum model,” *Phys. Rev. A* **23**, 236–247 (1981).
- [50] Gerhard Rempe, Herbert Walther, and Norbert Klein, “Observation of quantum collapse and revival in a one-atom maser,” *Phys. Rev. Lett.* **58**, 353–356 (1987).
- [51] Kazuki Koshino, “Single-photon filtering by a cavity quantum electrodynamics system,” *Phys. Rev. A* **77**, 023805 (2008).
- [52] Serge Rosenblum, Scott Parkins, and Barak Dayan, “Photon routing in cavity QED: Beyond the fundamental limit of photon blockade,” *Phys. Rev. A* **84**, 033854 (2011).
- [53] Ranojoy Bose, Deepak Sridharan, Hyochul Kim, Glenn S. Solomon, and Edo Waks, “Low-photon-number optical switching with a single quantum dot coupled to a photonic crystal cavity,” *Phys. Rev. Lett.* **108**, 227402 (2012).
- [54] E. Knill, R. Laflamme, and G. J. Milburn, “A scheme for efficient quantum computation with linear optics,” *Nature* **409**, 46–52 (2001).

- [55] T. B. Pittman, B. C. Jacobs, and J. D. Franson, “Demonstration of nondeterministic quantum logic operations using linear optical elements,” *Phys. Rev. Lett.* **88**, 257902 (2002).
- [56] Nicolas Sangouard, Christoph Simon, Hugues de Riedmatten, and Nicolas Gisin, “Quantum repeaters based on atomic ensembles and linear optics,” *Rev. Mod. Phys.* **83**, 33–80 (2011).
- [57] G. Y. Xiang, T. C. Ralph, A. P. Lund, N. Walk, and G. J. Pryde, “Heralded noiseless linear amplification and distillation of entanglement,” *Nat. Photon.* **4**, 316–319 (2010).
- [58] Axel Kuhn, Markus Hennrich, and Gerhard Rempe, “Deterministic single-photon source for distributed quantum networking,” *Phys. Rev. Lett.* **89**, 067901 (2002).
- [59] Zhiliang Yuan, Beata E. Kardynal, R. Mark Stevenson, Andrew J. Shields, Charlene J. Lobo, Ken Cooper, Neil S. Beattie, David A. Ritchie, and Michael Pepper, “Electrically driven single-photon source,” *Science* **295**, 102–105 (2002).
- [60] E. Moreau, I. Robert, J. M. Gérard, I. Abram, L. Manin, and V. Thierry-Mieg, “Single-mode solid-state single photon source based on isolated quantum dots in pillar microcavities,” *Appl. Phys. Lett.* **79**, 2865–2867 (2001).
- [61] Satoshi Kako, Charles Santori, Katsuyuki Hoshino, Stephan Gotzinger, Yoshihisa Yamamoto, and Yasuhiko Arakawa, “A gallium nitride single-photon source operating at 200 k,” *Nat Mater* **5**, 887–892 (2006).
- [62] Thomas M. Babinec, Hausmann Birgit J. M., Mughees Khan, Yinan Zhang, Jeronimo R. Maze, Philip R. Hemmer, and Marko Loncar, “A diamond nanowire single-photon source,” *Nat Nano* **5**, 195–199 (2010).
- [63] Maximilian Schlosshauer, “Decoherence, the measurement problem, and interpretations of quantum mechanics,” *Rev. Mod. Phys.* **76**, 1267–1305 (2005).
- [64] Girish S. Agarwal, *Quantum Optics* (Cambridge University Press, 2013).
- [65] Robert W. Boyd, “Nonlinear optics,” (Academic Press, Inc., New York, NY, 1992) pp. 192–206.
- [66] S. M. Hendrickson, T. B. Pittman, and J. D. Franson, “Nonlinear transmission through a tapered fiber in rubidium vapor,” *J. Opt. Soc. Am. B* **26**, 267–271 (2009).
- [67] S. M. Hendrickson, M. M. Lai, T. B. Pittman, and J. D. Franson, “Observation of two-photon absorption at low power levels using tapered optical fibers in rubidium vapor,” *Phys. Rev. Lett.* **105**, 173602 (2010).
- [68] D. E. Jones, J. D. Franson, and T. B. Pittman, “Saturation of atomic transitions using subwavelength diameter tapered optical fibers in rubidium vapor,” *J. Opt. Soc. Am. B* **31**, 1997–2001 (2014).

- [69] D. E. Jones, G. T. Hickman, J. D. Franson, and T. B. Pittman, “Nanofiber-segment ring resonator,” *Opt. Lett.* **41**, 3683–3685 (2016).
- [70] Meimei Lai, James D. Franson, and Todd B. Pittman, “Transmission degradation and preservation for tapered optical fibers in rubidium vapor,” *Appl. Opt.* **52**, 2595–2601 (2013).
- [71] Daniel Jones, *Interaction of Nanofiber-Guided Light with a Warm Atomic Vapor*, Ph.D. thesis, University of Maryland, Baltimore County, 1000 Hilltop Circle, Baltimore, MD 21227 (2016).
- [72] E. U. Condon and G. H. Shortley, “The theory of atomic spectra,” (Cambridge University Press, New York, NY, 1964) pp. 187–195, 257–262, 301–304.
- [73] I. I. Sobel’man, “Introduction to the theory of atomic spectra,” (Pergamon Press, Elmsford, NY, 1972) pp. 13–54, 119–120, 163–165, 185–186, 204–209.
- [74] Giulio Racah, “On a new type of vector coupling in complex spectra,” *Phys. Rev.* **61**, 537–537 (1942).
- [75] K. Watanabe, Edward C. Y. Inn, and Murray Zelikoff, “Absorption coefficients of oxygen in the vacuum ultraviolet,” *J. Chem. Phys.* **21**, 1026–1030 (1953).
- [76] M. Walhout, A. Witte, and S. L. Rolston, “Precision measurement of the metastable $6s[3/2]_2$ lifetime in xenon,” *Phys. Rev. Lett.* **72**, 2843–2846 (1994).
- [77] L. Allen, D. G. C. Jones, and D. G. Schofield, “Radiative lifetimes and collisional cross sections for xe i and ii,” *J. Opt. Soc. Am.* **59**, 842–847 (1969).
- [78] A. Kramida, Yu. Ralchenko, J. Reader, and NIST ASD Team, NIST Atomic Spectra Database (ver. 5.4), [Online]. Available: <http://physics.nist.gov/asd> [2016, November 16]. National Institute of Standards and Technology, Gaithersburg, MD. (2016).
- [79] M. R. Bruce, W. B. Layne, C. A. Whitehead, and J. W. Keto, “Radiative lifetimes and collisional deactivation of two-photon excited xenon in argon and xenon,” *J. Chem. Phys.* **92**, 2917–2926 (1990).
- [80] M. B. Das and S. Karmakar, “Radiative lifetimes of some excited states of neutral xenon,” *EPJ D* **32**, 285–288 (2005).
- [81] D. E. Jones, J. D. Franson, and T. B. Pittman, “Ladder-type electromagnetically induced transparency using nanofiber-guided light in a warm atomic vapor,” *Phys. Rev. A* **92**, 043806 (2015).
- [82] I.V. Hertel and C.P. Schulz, *Atoms, Molecules and Optical Physics 1: Atoms and Spectroscopy*, Graduate Texts in Physics (Springer, Berlin, 2014).
- [83] Renato James Cedolin, *Laser-Induced Fluorescence Diagnostics of Xenon Plasmas*, Ph.D. thesis, Stanford University (1997).

- [84] R. J. Cedolin, R. K. Hanson, and M. A. Cappelli, “Laser-induced fluorescence measurements of resonance broadening in xenon,” *Phys. Rev. A* **54**, 335–342 (1996).
- [85] A. Pine, C. Glassbrenner, and J. Kafalas, “Pressure-tuned gas diode-laser absorption spectroscopy of xenon hyperfine structure,” *IEEE J. Quantum Electron.* **9**, 800–807 (1973).
- [86] T. Xia, S. W. Morgan, Y. Y. Jau, and W. Happer, “Polarization and hyperfine transitions of metastable ^{129}Xe in discharge cells,” *Phys. Rev. A* **81**, 033419 (2010).
- [87] T. B. Pittman, D. E. Jones, and J. D. Franson, “Ultralow-power nonlinear optics using tapered optical fibers in metastable xenon,” *Phys. Rev. A* **88**, 053804 (2013).
- [88] L. Young, D. Yang, and R. W. Dunford, “Optical production of metastable krypton,” *J. of Phys. B* **35**, 2985 (2002).
- [89] Y. Ding, S.-M. Hu, K. Bailey, A. M. Davis, R. W. Dunford, Z.-T. Lu, T. P. O’Connor, and L. Young, “Thermal beam of metastable krypton atoms produced by optical excitation,” *Rev. Sci. Instrum.* **78**, 023103 (2007).
- [90] G. T. Hickman, J. D. Franson, and T. B. Pittman, “Optically enhanced production of metastable xenon,” *Opt. Lett.* **41**, 4372–4374 (2016).
- [91] John M. Choi, Reginald K. Lee, and Amnon Yariv, “Control of critical coupling in a ring resonator–fiber configuration: application to wavelength-selective switching, modulation, amplification, and oscillation,” *Opt. Lett.* **26**, 1236–1238 (2001).
- [92] A. Yariv, “Critical coupling and its control in optical waveguide-ring resonator systems,” *IEEE Photon. Technol. Lett.* **14**, 483–485 (2002).
- [93] C. Sames, H. Chibani, C. Hamsen, P. A. Altin, T. Wilk, and G. Rempe, “Antiresonance phase shift in strongly coupled cavity QED,” *Phys. Rev. Lett.* **112**, 043601 (2014).
- [94] Brian Vlastakis, Andrei Petrenko, Nissim Ofek, Luyan Sun, Zaki Leghtas, Katrina Sliwa, Yehan Liu, Michael Hatridge, Jacob Blumoff, Luigi Frunzio, Mazyar Mirrahimi, Liang Jiang, M. H. Devoret, and R. J. Schoelkopf, “Characterizing entanglement of an artificial atom and a cavity cat state with Bell’s inequality,” *Nature Communications* **6**, 8970 (2015).
- [95] Willis E. Lamb, “Theory of an optical maser,” *Phys. Rev.* **134**, A1429–A1450 (1964).
- [96] R. A. McFarlane, W. R. Bennett Jr., and W. E. Lamb Jr., “Single mode tuning dip in the power output of an He-Ne optical maser,” *Appl. Phys. Lett.* **2**, 189–190 (1963).
- [97] S. Bartalini, S. Borri, and P. De Natale, “Doppler-free polarization spectroscopy with a quantum cascade laser at $4.3\ \mu\text{m}$,” *Opt. Express* **17**, 7440–7449 (2009).
- [98] Ben E. Sherlock and Ifan G. Hughes, “How weak is a weak probe in laser spectroscopy?” *Am. J. Phys.* **77**, 111–115 (2009).

- [99] Ofer Firstenberg, Thibault Peyronel, Qi-Yu Liang, Alexey V Gorshkov, Mikhail D Lukin, and Vladan Vuletić, “Attractive photons in a quantum nonlinear medium,” *Nature* **502**, 71–75 (2013).
- [100] Hoonsoo Kang and Yifu Zhu, “Observation of large Kerr nonlinearity at low light intensities,” *Phys. Rev. Lett.* **91**, 093601 (2003).
- [101] Hsiang-Yu Lo, Po-Ching Su, and Yong-Fan Chen, “Low-light-level cross-phase modulation by quantum interference,” *Phys. Rev. A* **81**, 053829 (2010).
- [102] Bor-Wen Shiau, Meng-Chang Wu, Chi-Ching Lin, and Ying-Cheng Chen, “Low-light-level cross-phase modulation with double slow light pulses,” *Phys. Rev. Lett.* **106**, 193006 (2011).
- [103] Hsiang-Yu Lo, Yen-Chun Chen, Po-Ching Su, Hao-Chung Chen, Jun-Xian Chen, Ying-Cheng Chen, Ite A. Yu, and Yong-Fan Chen, “Electromagnetically-induced-transparency-based cross-phase-modulation at attojoule levels,” *Phys. Rev. A* **83**, 041804 (2011).
- [104] G. J. Milburn, “Quantum optical Fredkin gate,” *Phys. Rev. Lett.* **62**, 2124–2127 (1989).
- [105] Christopher C. Gerry and R. A. Campos, “Generation of maximally entangled photonic states with a quantum-optical Fredkin gate,” *Phys. Rev. A* **64**, 063814 (2001).
- [106] Robert C. Hilborn, “Einstein coefficients, cross sections, f values, dipole moments, and all that,” *Am. J. Phys.* **50**, 982–986 (1982).
- [107] Noriaki Tsukada, “Saturation effects of a two-level system in two RF fields,” *J. Phys. Soc. Jpn.* **46**, 1280–1287 (1979).
- [108] Z. Ficek and H. S. Freedhoff, “Resonance-fluorescence and absorption spectra of a two-level atom driven by a strong bichromatic field,” *Phys. Rev. A* **48**, 3092–3104 (1993).
- [109] Neil B. Manson, Changjiang Wei, and John P. D. Martin, “Response of a two-level system driven by two strong fields,” *Phys. Rev. Lett.* **76**, 3943–3946 (1996).
- [110] Quentin A. Turchette, *Quantum Optics with Single Atoms and Single Photons*, Ph.D. thesis, California Institute of Technology (1997).
- [111] Christina J. Hood, *Real-Time Measurement and Trapping of Single Atoms by Single Photons*, Ph.D. thesis, California Institute of Technology (2000).
- [112] D. G. Norris, E. J. Cahoon, and L. A. Orozco, “Atom detection in a two-mode optical cavity with intermediate coupling: Autocorrelation studies,” *Phys. Rev. A* **80**, 043830 (2009).

